

AD-A079 862

AIR FORCE INST OF TECH WRIGHT-PATTERSON AFB OH SCH00--ETC F/6 13/13
COLUMN BUCKLING OF ISOTROPIC AND COMPOSITE BEAMS USING A TRUNCA--ETC(U)
DEC 79 J L INSPRUCKER
AFIT/6A/AA/804-2

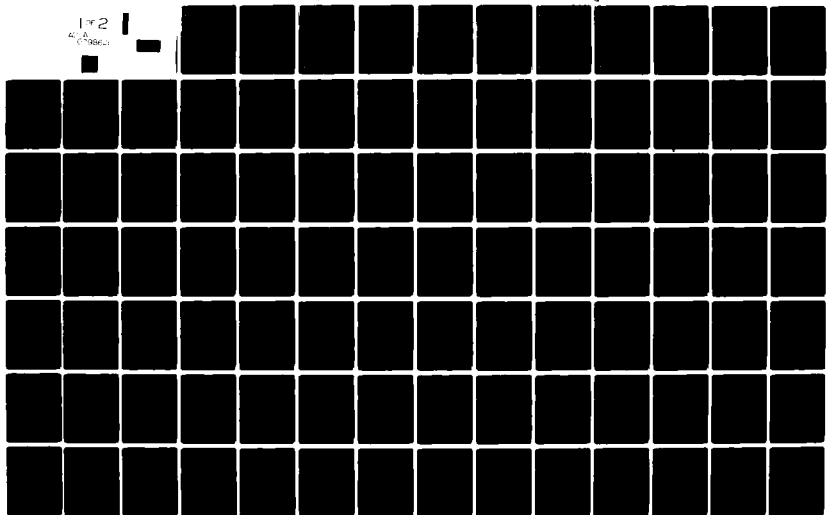
UNCLASSIFIED

NL

172

400

(1986)



AFIT/GA/AA/80M-2

①

COLUMN BUCKLING OF ISOTROPIC
AND COMPOSITE BEAMS USING A
TRUNCATED FOURIER SERIES

THESIS

AFIT/GA/AA/80M-2

John L. Insprucker III
2nd Lt USAF

D D C
RECEIVED
JAN 28 1980
A

Approved for public release; distribution unlimited

14

AFIT/GA/AA/80M-2

12 139

6 COLUMN BUCKLING OF ISOTROPIC AND COMPOSITE BEAMS USING A TRUNCATED FOURIER SERIES .

9 Master's Thesis

Presented to the Faculty of the School of Engineering of the Air Force Institute of Technology Air University in Partial Fulfillment of the Requirements for the Degree of Master of Science

Table with columns and rows, some handwritten marks.

Louis

10 by John [redacted] / Insprucker, III 2nd Lt USAF

Graduate Astronautical Engineering

11 Dec [redacted] 79

Approved for public release, distribution unlimited

012225 Ym

Preface

This thesis applies the trigonometric approach to finite difference calculus in order to calculate column buckling loads. The loads are found using a virtual work energy approach. It is hoped that my results will encourage the further expansion of the trigonometric method to different structural geometries as an alternative to finite elements.

I wish to thank Dr. Anthony Palazotto for allowing me to pursue this line of research and for his guidance. In a year when he had several thesis students, he always had time to help me. His ability to provide information was amazing.

I also thank Captain Steven Hannah, my predecessor in this field, who provided guidance through his own thesis.

John L. Insprucker III

Contents

| | Page |
|--|------|
| Preface | ii |
| List of Figures | v |
| List of Tables | viii |
| List of Symbols | ix |
| Abstract | xi |
| I. Introduction | 1 |
| Background | 1 |
| Purpose | 4 |
| General Approach | 4 |
| II. Theory | 6 |
| Assumptions | 6 |
| Virtual Work Equation | 7 |
| Boundary Conditions | 8 |
| III. Numerical Technique | 9 |
| Finite Difference Calculus | 9 |
| Conventional Approach | 9 |
| Trigonometric Approach | 14 |
| Application to the Virtual Work Equation | 18 |
| Summary | 27 |
| IV. Uniform Beam Results | 29 |
| Uniform Beam Solutions | 32 |
| Pinned-Pinned | 34 |
| Guided-Guided | 36 |
| General Results | 37 |
| Summary | 42 |
| V. Beams with Variable Inertia | 52 |
| Introduction | 52 |
| Optimization of λ | 53 |
| Continuous Inertia | 55 |
| Sinusoidal Variation | 55 |
| Exponential Variation | 58 |
| Discontinuous Inertia | 61 |
| Specific Examples | 64 |
| Summary | 68 |

| | |
|---|-----|
| VI. Variable Mesh | 78 |
| Introduction | 78 |
| Technique | 80 |
| Test Results | 85 |
| Summary | 91 |
| VII. Extension to Composite Materials | 98 |
| Introduction | 98 |
| Theory | 99 |
| Laminated Plate Approach | 99 |
| Results | 102 |
| Summary | 104 |
| VIII. Conclusions | 106 |
| Bibliography | 111 |
| Appendix A: Derivation of the Virtual Work Equation | 114 |
| Appendix B: Trigonometric Finite Difference Expression for the Second Derivative of the Deflection with a Variable Mesh | 117 |
| Appendix C: Effective Inertia at a Sudden Change In Cross-Section | 119 |
| Appendix D: Flexural Rigidity of a Composite Beam | 122 |
| Vita | 124 |

List of Figures

| Figure | Page |
|--|------|
| 1 Typical Beam Under Axial Load | 8 |
| 2 Deflection Shape Versus Nodal Arrangement | 10 |
| 3 Beam Deflection Using a Half-Station Node Pattern | 12 |
| 4 Node Pattern for N Internal Nodes | 19 |
| 5 Numerical Integration of fdx Using a Full-Station Approach | 20 |
| 6 Numerical Integration of gdx Using a Half-Station Approach | 21 |
| 7 Pinned-Pinned Beam with Nine Nodes | 35 |
| 8 Buckling Load Versus Wavelength Parameter | 40 |
| 9 Buckling Load Curve Comparing Error for Trigonometric and Conventional Solutions for a Pinned-Pinned Beam | 43 |
| 10 Buckling Load Curve Comparing Error for Trigonometric and Conventional Solutions for a Pinned-Clamped Beam | 44 |
| 11 Buckling Load Curve Comparing Error for Trigonometric and Conventional Solutions for a Clamped-Clamped Beam | 45 |
| 12 Buckling Load Curve Comparing Error for Trigonometric and Conventional Solutions for a Clamped-Free Beam | 46 |
| 13 Comparison of the Eigenvector and the Exact Mode Shape for a Pinned-Pinned Beam | 47 |
| 14 Comparison of the Eigenvector and the Exact Mode Shape for A Pinned-Guided Beam | 48 |
| 15 Comparison of the Eigenvector and the Exact Mode Shape for a Clamped-Clamped Beam | 49 |
| 16 Comparison of the Eigenvector and the Exact Mode Shape for a Pinned-Clamped Beam | 50 |
| 17 Comparison of the Eigenvector and the Exact Mode Shape for a Clamped-Guided Beam | 51 |

| | | |
|----|--|----|
| 18 | Optimization Curves for Buckling | 54 |
| 19 | Sinusoidal Variation in Inertia | 56 |
| 20 | Typical Discontinuous Beam | 62 |
| 21 | Discontinuous Beam of the First Example | 65 |
| 22 | Third Example of a Discontinuous Beam | 68 |
| 23 | Buckling Load Curves for a Beam with Sinusoidal Inertia. $N = 9,11$ | 70 |
| 24 | Buckling Load Curves for a Beam with Exponential Inertia. $N = 9,11$ | 71 |
| 25 | Buckling Load Curves for a Beam with Exponential Inertia. $N = 9,10$ | 72 |
| 26 | Buckling Load Curves for a Beam with Exponential Inertia. $N = 9,12$ | 73 |
| 27 | Buckling Load Curves for a Discontinuous Beam, $I_1/I_2 = .4$, $a/L = .4$. $N = 9,19$ | 74 |
| 28 | Buckling Load Curve for a Discontinuous Beam, $I_1/I_2 = .4$, $a/L = .4$. $N = 10$ | 75 |
| 29 | Buckling Load Curves for a Discontinuous Beam, $I_1/I_2 = .4$, $a/L = .4$. $N = 8,9$ | 76 |
| 30 | Buckling Load Curves for a Discontinuous Beam, $I_1 = I_3 = .4$, $I_2 = 1.0$, $a_1 = .2L$, $a_2 = .6L$. $N = 9,19$ | 77 |
| 31 | Comparison of Uniform and Variable Meshes | 79 |
| 32 | Numerical Integration of fdx for a Variable Mesh | 81 |
| 33 | First Variable Mesh Example | 85 |
| 34 | Discontinuous Beam with Variable Mesh A | 86 |
| 35 | Discontinuous Beam with Variable Mesh B | 87 |
| 36 | Discontinuous Beam $I_1/I_2 = .5$, $a/L = .5$ | 90 |
| 37 | Uniform and Variable Mesh Curves for a Discontinuous Beam, $I_1/I_2 = .1$, $a/L = .2$, $N = 9$, $h_2 = .05L$ | 93 |

| | | |
|----|---|-----|
| 38 | Uniform and Variable Mesh Curves for a Discontinuous Beam, $I_1/I_2 = .1$, $a/L = .2$, $N = 9$, $h_2 = .05L$ | 94 |
| 39 | Uniform and Variable Mesh Curves for a Discontinuous Beam, $I_1/I_2 = .5$, $a/L = .5$, $N = 9$, $h_2 = .05L$ | 95 |
| 40 | Uniform and Variable Mesh Curves for a Beam with Sinusoidal Inertia, $N = 9$, $h_2 = .05L$ | 96 |
| 41 | Uniform and Variable Mesh Curves for a Beam with Exponential Inertia, $N = 9$, $h_2 = .05L$ | 97 |
| 42 | Composite Beam Cross-Section and Lay-Up | 100 |
| A1 | Beam Element Under Axial Loading | 114 |
| A2 | Deflected Beam Segment Shape | 116 |
| B1 | Variable Mesh Size Arrangement | 117 |
| C1 | Step Change in Inertia | 119 |
| C2 | Fictitious and Actual Node Displacements | 120 |

List of Tables

| Table | Page |
|--|------|
| I Optimal Wavelengths for Uniform Beams with 10 Boundary Combinations | 39 |
| II Nine Internal Node Variable Mesh Results | 91 |

List of Symbols

| | |
|------------------------|---|
| A_{11} | In plane stiffness constant for a composite beam |
| A, B, C | Matrices of displacement coefficients |
| \tilde{A}, \tilde{B} | A, B matrices with h factored out |
| a_i | Coefficients of virtual displacements at node i |
| B_{11} | Stiffness coupling coefficient for a composite beam |
| D_{11} | Flexural stiffness coefficient for a composite beam |
| E | Young's modulus of elasticity |
| $E_{1,2}$ | Modulus of elasticity parallel and normal to principal composite fiber directions |
| f_i, g_i | Functions defined at node i for the virtual work equation |
| G | Shear modulus |
| h | Uniform mesh size |
| h_1, h_2, h_3 | Variable mesh sizes |
| \tilde{h} | Equivalent mesh sizes |
| i | Index attached to a variable to denote node number or the composite lamina number |
| I | Moment of inertia |
| I_L | Inertia to the left of a discontinuity |
| I_R | Inertia to the right of a discontinuity |
| I_{eff} | Value of inertia applied at a discontinuity node |
| J_0, J_1 | Bessel functions |
| k_{cr} | Critical axial buckling parameter |
| L | Beam length |
| M | Moment in the x direction for simple beam theory |

| | |
|-----------------|--|
| $M_{x,y}$ | Moments in the x, y directions |
| n | Bessel function argument |
| N | Number of internal node points |
| P | Axial load |
| P_{cr} | Critical buckling load |
| T_i | Coefficients of Fourier series |
| δU | Internal virtual strain energy |
| w | Transverse (vertical) beam displacement |
| δW_i | Internal virtual work |
| δW_e | External virtual work |
| x | Axial coordinate system |
| ϵ_x | Strain in axial direction |
| λ | Variable wavelength parameter |
| λ_{opt} | Wavelength corresponding to P_{cr} |
| ν_{12} | Poisson's ratio for a composite material |
| π | Total potential energy |
| σ_x | Axial stress in the x direction |
| σ_y | Stress in the y direction |
| θ | Fiber orientation angle |

Abstract

A trigonometric approach to finite difference calculus was applied to solve for beam buckling loads using a virtual work method. The trigonometric equation, a truncated Fourier series, permitted varying the buckling load by adjusting a wavelength parameter. Values for the buckling load of a variety of beams - uniform, homogeneous, variable and discontinuous inertias, composite - were found under a wide range of boundary conditions. Choosing the optimal wavelength produced the result from literature. An optimization scheme was used which determines the critical load by locating the intersection of two buckling load curves. The method is accurate as long as points of interest - maximum inertia, discontinuities - are modeled by the nodal arrangement. The trigonometric approach provided improved accuracy over the conventional approach for a wide range of wavelengths. For an infinite value of the wavelength, the trigonometric approach converges to the conventional one. A variable mesh designed to concentrate nodes about points of interest was found to be relatively ineffective when compared to a uniform mesh. Composite materials were modeled using an equivalent flexural rigidity.

COLUMN BUCKLING OF ISOTROPIC
AND COMPOSITE BEAMS USING A
TRUNCATED FOURIER SERIES

I. Introduction

Background

In the past, structural problems were solved using simplifying assumptions and rule of thumb. This still holds true today to a great extent. But today's problems are demanding more than the "linearized solution" often seen in problem analysis. Today's structures are becoming more complex, more daring, more costly than ever before. From new architecturally advanced domed stadiums to large space structures, these designs push our knowledge and its use to the limit. With this advance has come the need for more effective tools to provide the necessary accuracy required by these designs. And this need is being met through the use of modern computers and associated software. This software takes form as programs - STAGS, SAP, NASTRAN - available to an engineer for structural analysis and design. With these new tools, solutions to the problems of the real, "non-linear" world can be more accurately approached. The only limit is the precision of the engineer's model and the numerical technique he applies. Because of the increasing accuracy available, the engineer can concentrate on attaining the most accuracy for the least time and cost - symbolized by

choosing the best technique as judged in these terms.

Finite difference calculus is the technique applied in this thesis. It models the beams analyzed within by dividing them up into a finite number of degrees of freedom (nodes) (5-8). A trigonometric finite difference is used as opposed to a conventional finite difference. The conventional finite difference approximates a function's derivatives by combinations of a Taylor series expansion (8-10). This technique is good when the function in question is polynomial in nature. The functions in this thesis are directly dependent upon the beam's buckling shape, which is sinusoidal. To model the necessary derivatives, a technique developed by Stein and Housner (1,2) and expanded upon by Hannah (3,4) is incorporated. A truncated Fourier series is used to develop trigonometric finite difference expressions for the needed derivatives. By using a Fourier, rather than a Taylor series, a closer approximation of the derivatives of the sinusoidal shape results. In his thesis, Hannah showed the improved accuracy of this trigonometric approach over the conventional method.

Beam buckling, also known as Euler column buckling, is an important problem in structural design. Beam buckling is referred to as column buckling because the load configuration on a beam that causes axial buckling is most often seen when the beam is used as a column, as in a landing gear strut. The prediction of the critical, or buckling, load on the column is of primary concern in the beam design. For example, possible solar power satellites, as described by Nansen (11),

would be constructed of composite struts. With a known loading, the problem in strut design becomes one of finding the optimum dimensions to prevent column buckling while conserving mass and space. The minimum force which can cause buckling is the critical buckling load. Below this load, a perfect beam will remain flat in equilibrium. At the critical load, the beam will deflect suddenly to a position of higher equilibrium. This defines the buckling load as that load which causes the beam to deflect from its lowest equilibrium position (12-13). While there are higher critical loads, they are not of interest in this thesis.

In Hannah's work, the uniform beam was observed under a variety of boundary conditions to validate the use of trigonometric finite difference expressions. However, most beams are not so simple. Struts for use in the solar satellite can be both composite and tapered - not constant in either material properties or inertia. The non-uniform beam is of great interest. While some solutions have been published, these tend to be expressed as bounds on the exact buckling load found by a numerical method or by approximations to the governing differential equations (14-18). The ability to achieve an accurate solution may be possible with the trigonometric technique. In fact, the exact solution may be attainable. The solution is only as exact as the model of beam buckling makes it.

There are many effects which are not included in the beam buckling equations. The trigonometric technique can provide the solutions for beams with variable cross-section,

material properties, node arrangements and combinations of various boundary conditions.

Purpose

The purpose of this thesis is to use the trigonometric finite difference approach to calculate the critical axial load in a beam under a wide variety of conditions. These conditions include continuous and discontinuous changes in inertia, isotropic and composite materials, uniform and variable nodal arrangements and multiple boundary combinations. Solutions are obtained using the virtual work equation and are a function of a variable wavelength parameter in the truncated Fourier series. Success in applying this technique depends upon accuracy of the generated solution and the time it takes.

General Approach

In his thesis, Hannah showed the superiority of the virtual work equation (3,19-21) versus the equilibrium approach in generating the correct answer to the buckling load problem. Likewise, the advantage of the truncated Fourier series over the Taylor series in developing the finite difference derivatives for a simple beam was demonstrated. Therefore, I started my analysis of more complex beams using the virtual work equation and the truncated Fourier series.

The first and second derivatives of the beam's deflection at an arbitrary point are developed from the Fourier series. To integrate the virtual work equation, the beam's domain is divided into a series of nodes, each a constant distance apart.

The trapezoidal rule is made use of in integrating the virtual work equation over the length of the beam. The solution depends upon the location of the nodes and the derivatives previously developed. The end result is an eigenvalue equation, with the lowest eigenvalue related to the critical buckling load. By separating virtual and actual displacements at each node, the eigenvalue equation is transformed into an eigenvalue related to the buckling load.

Imbedded within the algebraic equations which form the eigenvalue matrix are the effects of variable inertia and material properties. Also, combinations of four end restraints are used in reducing the equations to their final matrix form. Restraints considered are pinned, clamped, guided and free.

A similar procedure is carried out to examine the effect of a mesh with non-constant intervals between node points. This variable mesh requires the development of finite difference derivatives which have dissimilar mesh spacings on either side of the reference point. The procedure for developing the matrix equation is similar to that used in the uniform mesh solution except these new derivatives are inserted at nodes where the mesh interval changes.

Results pertaining to the eigenvalue for a simple uniform beam were obtained by Hannah using a method similar to this one. The solutions for his simple beam are widely available in literature (18,19,22-23). A broader range of beams can be analyzed by applying this thesis. When possible, a comparison with known solutions is made (8,14-18,24).

II. Theory

Assumptions

The virtual work equation for beam buckling (19-21) was derived with the following assumptions:

1. Sections of the beam normal to the longitudinal axis that are planar before buckling remain plane during buckling.
2. The length of the beam is much greater compared to the width or the height.
3. Displacements are small along the beam.
4. The beam is flat before buckling.
5. The beam is composed of a homogeneous, isotropic material.
 - A. For composite beams, interlaminar effects are ignored and the flexural rigidity is averaged through the cross-section.
6. The inertia used at a discontinuity is a weighted average of inertias around the step which preserves continuity and equilibrium.
7. Axial loading is along the neutral axis with the neutral axes of beam segments being co-linear.
8. Only bending strain energy is considered.

The accuracy of the buckling load solution is only as good as these assumptions allow.

Virtual Work Equation

The principle of virtual work is used to provide the basic equation of this thesis. Its ultimate solution is the critical buckling load P_{cr} . The principle of virtual work states that for the variation of potential energy to be zero (an equilibrium state), the variation in external work done by the forces acting on the beam through a small displacement must be equal and opposite to the variation of internal work done by internal forces (8). Mathematically, virtual work states that

$$\delta W_e = -\delta W_i \quad (2-1)$$

where δW_e and δW_i are the virtual external and internal work due to small displacements. The internal work can be related to a beam's strain energy by

$$\delta W_i = -\delta U \quad (2-2)$$

The virtual work equation can now be stated in terms of the external virtual work done by the load P and the internal strain energy. For a one dimensional axially loaded beam, the virtual work equation is

$$\int_0^L EI \frac{d^2 w}{dx^2} \frac{d^2 \delta w}{dx^2} dx = P \int_0^L \frac{dw}{dx} \frac{d\delta w}{dx} dx \quad (2-3)$$

The derivation of the virtual work equation is shown in Appendix A

Figure 1 shows the coordinate system and axial loading of the beam. The beam's lateral deflection is w , measured from the neutral axis (generally the midplane for a symmetric beam). E is the modulus of elasticity, and I is the beam's inertia.

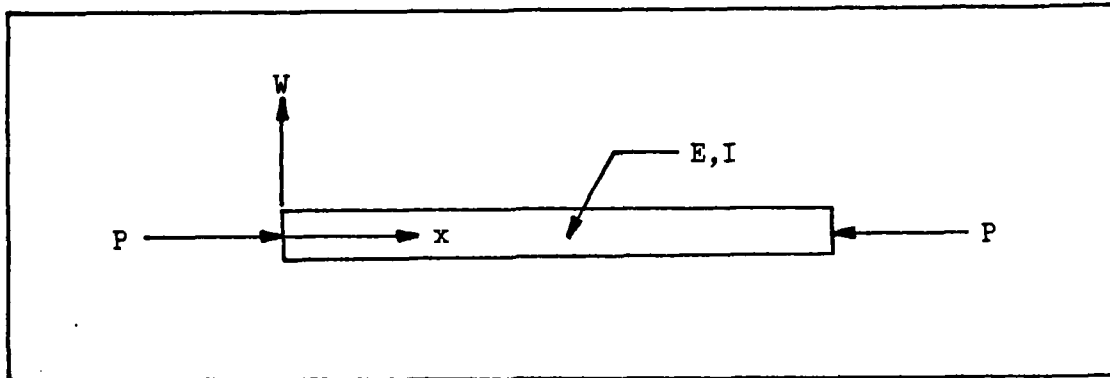


Fig 1. Typical Beam Under Axial Load

Boundary Conditions

Four boundary conditions are considered for beams in this thesis: pinned, clamped, guided, free. These are the most commonly seen conditions and they can be applied in any possible combination. For the virtual work approach incorporated in this thesis, the boundary conditions used are

- | | | | |
|------------|--------------|---------------------|-------|
| 1. Pinned | $W(A) = 0$ | $\delta W(A) = 0$ | |
| | $W''(A) = 0$ | $\delta W''(A) = 0$ | |
| 2. Clamped | $W(A) = 0$ | $\delta W(A) = 0$ | |
| | $W'(A) = 0$ | $\delta W'(A) = 0$ | (2-4) |
| 3. Guided | $W'(A) = 0$ | $\delta W'(A) = 0$ | |
| 4. Free | $W''(A) = 0$ | $\delta W''(A) = 0$ | |

where A is either the boundary $x = 0$ or $x = L$.

While pinned and clamped boundaries supply two conditions for $W(A)$ or its derivatives, guided and free do not. A third order boundary condition on shear is available, but because it is a third order differential it is not possible for use in this work. Instead, an additional degree of freedom exists whenever a guided or free boundary is encountered in order to satisfy the equilibrium characteristics at the boundary. This replaces the shear condition.

III. Numerical Technique

Finite Difference Calculus

The evaluation of the buckling load of a beam can be a difficult task, especially when the variation of moment of inertia or stiffness does not follow a simple law. For these reasons, approximate methods of computation have been devised which provide bounds on the buckling load (6,14-18). Since 1910, a finite difference procedure for determining the characteristic values of differential equations has been widely investigated. This procedure presents a wide range of applications as well as simplicity. With finite differences, the solution to beam buckling can be carried out easily, requiring only the needed computing power.

Conventional Approach

Although a truncated Fourier series will be used to derive trigonometric finite difference derivatives, a study of the conventional finite difference derivatives is useful. The conventional approach highlights many important ideas and also adds insight in applying the trigonometric approach.

The concept of finite differences is similar for both the conventional and trigonometric approaches. A function under investigation, the beam deflection W in this thesis, is modeled as a collection of node points. These nodes can be considered as superimposed upon the beam. Figure 2

represents $W(x)$ divided into a finite difference mesh.

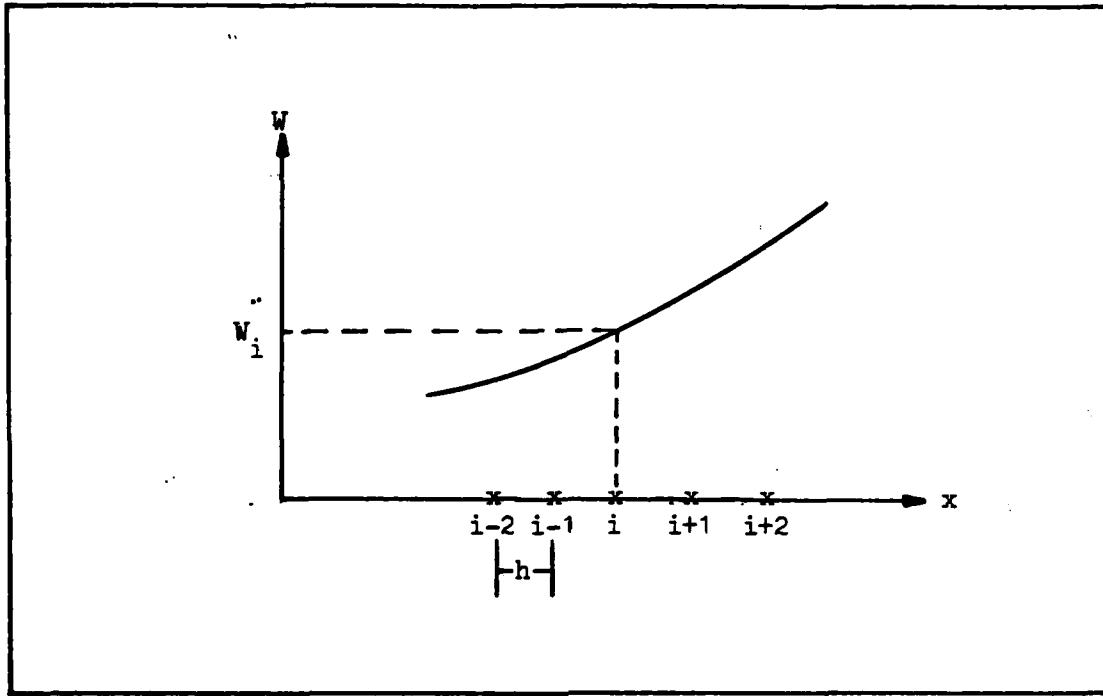


Fig 2. Deflection Shape Versus Nodal Arrangement

The nodes are numbered, with the deflection W_i corresponding to node i as indicated. The mesh spacing h is the distance between nodes and is shown as a constant. Node points, marked by the X's in Fig 2, are positions at which the deflection is defined.

The conventional derivatives, those derived using a conventional finite difference approach, are found as combinations of a Taylor series. The value of the displacement function at location $X + h$ can be described by the Taylor series

$$\begin{aligned}
 W(X + h) = & W(X) + hW'(X) + \frac{1}{2}h^2W''(X) + \frac{1}{6}h^3W'''(X) \\
 & + \frac{1}{24}h^4W^{(4)}(X) + \dots \quad (3-1)
 \end{aligned}$$

This can be written as

$$W_{i+1} = W_i + hW'_i + \frac{1}{2}h^2W''_i + \frac{1}{6}h^3W'''_i + \frac{1}{24}h^4W^{iv}_i + \dots \quad (3-2)$$

where i corresponds to the position of node i and $+1$ is a distance h from i . Likewise, -1 is a node a distance $-h$ from i . This notation provides

$$W(X - h) = W_{i-1} = W_i - hW'_i + \frac{1}{2}h^2W''_i - \frac{1}{6}h^3W'''_i + \frac{1}{24}h^4W^{iv}_i + \dots \quad (3-3)$$

By subtracting Eq (3-2) from Eq (3-3) and rearranging terms, an expression for the first derivative is obtained.

$$W'_i = \frac{1}{2h}(W_{i+1} - W_{i-1}) - \frac{h^2}{6}W''_i + \dots \quad (3-4)$$

Typically all but the first term is ignored, with the second term $(h^2/6)W''_i$ a measure of the error by truncating. Adding Eq (3-2) to Eq (3-3) provides the second derivative at node i in terms of the adjacent node points.

$$W''_i = \frac{1}{h^2}(W_{i+1} - 2W_i + W_{i-1}) - \frac{h^2}{12}W^{iv}_i + \dots \quad (3-5)$$

Once again, the first term is the finite difference expression with $(h^2/12)W^{iv}_i$ representing the relative error due to truncation.

Because the virtual work equation depends only on first and second derivatives of the deflection W , no further derivatives need to be found. However, an increase in accuracy is possible. The two conventional equations were derived at a node in terms of deflection values at adjacent nodes. However the reference point i can be located between two adjacent nodes. This is diagrammed in Figure 3 and is referred to as a half-station approximation.

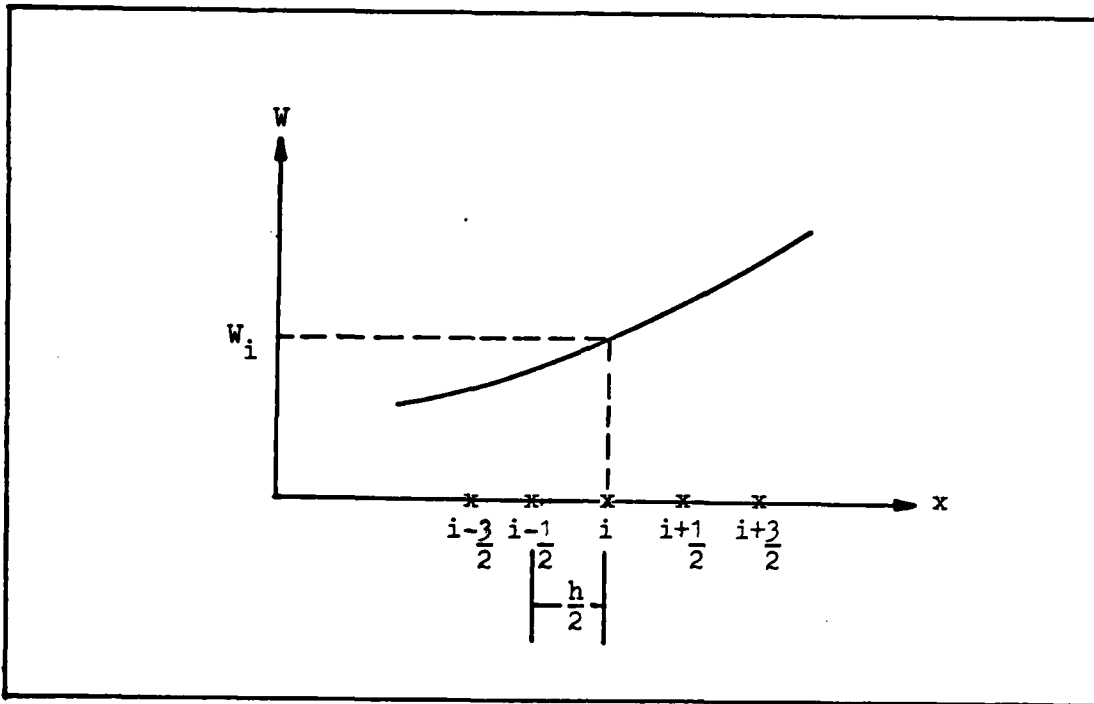


Fig 3. Beam Deflection Using a Half-Station Node Pattern

The development of half-station finite difference expressions follows the same procedure as the full-station approximations by replacing $\pm h$ by $\pm h/2$ and ± 1 by $\pm 1/2$. The Taylor series expressions become

$$\begin{aligned}
 W(x + h/2) = W_{i+\frac{1}{2}} &= W_i + \frac{h}{2}W_i' + \frac{1}{2}\left(\frac{h}{2}\right)^2 W_i'' + \frac{1}{6}\left(\frac{h}{2}\right)^3 W_i''' \\
 &+ \frac{1}{24}\left(\frac{h}{2}\right)^4 W_i^{iv} + \dots \quad (3-6)
 \end{aligned}$$

$$\begin{aligned}
 W(x - h/2) = W_{i-\frac{1}{2}} &= W_i - \frac{h}{2}W_i' + \frac{1}{2}\left(\frac{h}{2}\right)^2 W_i'' - \frac{1}{6}\left(\frac{h}{2}\right)^3 W_i''' \\
 &+ \frac{1}{24}\left(\frac{h}{2}\right)^4 W_i^{iv} + \dots \quad (3-7)
 \end{aligned}$$

Subtracting Eq (3-6) from Eq (3-7) provides

$$W_i' = \frac{1}{h}(W_{i+\frac{1}{2}} - W_{i-\frac{1}{2}}) - \frac{h^2}{24}W_i''' + \dots \quad (3-8)$$

The error term is represented by $(h^2/24)W_i'''$. Comparing with the error term from Eq (3-4), $(h^2/6)W_i''$, shows that a first derivative of W is better represented by a half-station approximation. To produce an expression for W_i' , the expansions of $W(X + 3/2h)$ and $W(X - 3/2h)$ are needed. These prevent bringing W_i into the solution. W_i is a reference point, not a node as was defined

$$W\left(i + \frac{3}{2}\right) = W_i + \left(\frac{3h}{2}\right)W_i' + \frac{1}{2}\left(\frac{3h}{2}\right)^2 W_i'' + \frac{1}{6}\left(\frac{3h}{2}\right)^3 W_i''' + \frac{1}{24}\left(\frac{3h}{2}\right)^4 W_i^{iv} + \dots \quad (3-9)$$

$$W\left(i - \frac{3}{2}\right) = W_i - \left(\frac{3h}{2}\right)W_i' + \frac{1}{2}\left(\frac{3h}{2}\right)^2 W_i'' - \frac{1}{6}\left(\frac{3h}{2}\right)^3 W_i''' + \frac{1}{24}\left(\frac{3h}{2}\right)^4 W_i^{iv} + \dots \quad (3-10)$$

Adding Eq (3-9) to Eq (3-10) gives

$$W_{i+\frac{3}{2}} + W_{i-\frac{3}{2}} = 2W_i + \frac{9h^2}{4} W_i'' + \frac{27}{64} W_i^{iv} + \dots \quad (3-11)$$

Adding Eq (3-6) and Eq (3-7) provides an expression for $2W_i$.

Substituting into (3-11) gives

$$W_i'' = \frac{1}{2h^2} (W_{i+\frac{3}{2}} - W_{i+\frac{1}{2}} - W_{i-\frac{1}{2}} + W_{i-\frac{3}{2}}) - \frac{5h^2}{24} W_i^{iv} + \dots \quad (3-12)$$

Comparing the error term from this half-station derivation $(5h^2/24 W_i^{iv})$ to the error term from the full-station derivation $(h^2/12 W_i^{iv})$ indicated that the full-station expression for W_i' (Eq (3-5)) is the more accurate.

The method of producing derivative expressions by half- or full-station approximations can be extended to trigonometric

finite difference expressions where the comparison between error terms is difficult.

Trigonometric Approach

The conventional approach provides good approximations, provided the function being approximated is polynomial in nature. However, beam buckling has a sinusoidal mode shape. By using a Fourier series, rather than the conventional Taylor series, one should obtain better approximations due to its trigonometric terms. Stein and Housner (1,2) recommended just this approach. The recommended Fourier series, a truncated one, was given by

$$W(X) = T_1 + T_2 \sin \frac{\pi(X-X_0)}{\lambda} + T_3 \cos \frac{\pi(X-X_0)}{\lambda} \quad (3-13)$$

where λ is a variable wavelength parameter and X_0 is the reference point, usually the node i . The wavelength parameter λ may take on any value from zero to infinity. Derivation of the first and second derivatives follows closely from the conventional approaches, with much the same terminology.

Using the results from the conventional approach, a half-station approximation will be used for the first derivative of the deflection W . The derivative of Eq (3-13) with respect to X is

$$W'(X) = T_2 \frac{\pi}{\lambda} \cos \frac{\pi(X-X_0)}{\lambda} - T_3 \frac{\pi}{\lambda} \sin \frac{\pi(X-X_0)}{\lambda} \quad (3-14)$$

Evaluating this at the reference point $X = X_0$ gives

$$W'(X_0) = T_2 \frac{\pi}{\lambda} \quad (3-15)$$

and

$$T_2 = \frac{\lambda}{\pi} W'(X_0) \quad (3-16)$$

The second derivative of Eq(3-13) provides a similar expression for T_3 when evaluated at $X = X_0$.

$$T_3 = -\left(\frac{\lambda}{\pi}\right)^2 W''(X_0) \quad (3-17)$$

Finally, evaluating Eq (3-13) at $X = X_0$ provides a meaning for T_1

$$T_1 = W(X_0) + \left(\frac{\lambda}{\pi}\right)^2 W''(X_0) \quad (3-18)$$

The truncated Fourier series can now be expressed in terms of sine, cosine and the function with its derivatives at a chosen reference point.

$$W(X) = W(X_0) + \frac{\lambda}{\pi} W'(X_0) \sin \frac{\pi(X-X_0)}{\lambda} + \left(\frac{\lambda}{\pi}\right)^2 W''(X_0) \left[1 - \cos \frac{\pi(X-X_0)}{\lambda}\right] \quad (3-19)$$

With this expression, the necessary derivatives are obtained. As previously stated, the first derivative of W will be evaluated with a half-station approximation. Using the same notation as for the conventional approach ($X_0 = \text{node } i$ and $\pm h/2 = \pm 1/2$)

$$W\left(X_0 + \frac{h}{2}\right) = W_{i+\frac{1}{2}} = W_i + \frac{\lambda}{\pi} W'_i \sin \frac{\pi h/2}{\lambda} + \left(\frac{\lambda}{\pi}\right)^2 W''_i \left[1 - \cos \frac{\pi h/2}{\lambda}\right] \quad (3-20)$$

$$W\left(X_0 - \frac{h}{2}\right) = W_{i-\frac{1}{2}} = W_i - \frac{\lambda}{\pi} W'_i \sin \frac{\pi h/2}{\lambda} + \left(\frac{\lambda}{\pi}\right)^2 W''_i \left[1 - \cos \frac{\pi h/2}{\lambda}\right] \quad (3-21)$$

Subtracting Eq (3-21) from Eq (3-22) gives the expression

for W_i'

$$W_i' = \frac{1}{\frac{2\lambda}{\pi} \sin \frac{\pi h}{2\lambda}} (W_{i+\frac{1}{2}} - W_{i-\frac{1}{2}}) \quad (3-22)$$

If $\tilde{h} \equiv \frac{2\lambda}{\pi} \sin \frac{\pi h}{2\lambda}$, the finite difference expression looks very similar to that derived by the conventional approach. This \tilde{h} is the equivalent mesh size, as opposed to the mesh size h from the conventional approach.

The second derivative of the beam deflection W will be a full-station approximation. Therefore, the function is evaluated at $X = X_0 \pm h$. It was shown earlier that the full-station approach has a smaller truncation error. Evaluating $W(X)$ at these points gives

$$W(X_0 + h) = W_{i+1} = W_i + \frac{\lambda}{\pi} W_i' \sin \frac{\pi h}{\lambda} + \left(\frac{\lambda}{\pi}\right)^2 W_i'' \left[1 - \cos \frac{\pi h}{\lambda}\right] \quad (3-23)$$

$$W(X_0 - h) = W_{i-1} = W_i - \frac{\lambda}{\pi} W_i' \sin \frac{\pi h}{\lambda} + \left(\frac{\lambda}{\pi}\right)^2 W_i'' \left[1 - \cos \frac{\pi h}{\lambda}\right] \quad (3-24)$$

Adding Eq (3-23) to Eq (3-24) provides W_i'' .

$$W_i'' = \frac{1}{2\left(\frac{\lambda}{\pi}\right)^2 \left[1 - \cos \frac{\pi h}{\lambda}\right]} (W_{i+1} - 2W_i + W_{i-1}) \quad (3-25)$$

By using the formula $\cos 2\theta = \cos^2 \theta - \sin^2 \theta$ where $\theta = \pi h/2\lambda$, the quantity

$$2\left(\frac{\lambda}{\pi}\right)^2 \left[1 - \cos \frac{\pi h}{\lambda}\right] = \left(\frac{2\lambda}{\pi}\right)^2 \sin^2 \frac{\pi h}{2\lambda} \quad (3-26)$$

This revised expression is merely the equivalent mesh size

squared \tilde{h}^2 . The second derivative can be expressed in the familiar form

$$W_i'' = \frac{1}{\tilde{h}^2} (W_{i+1} - 2W_i + W_{i-1}) \quad (3-27)$$

This equation is similar to the conventional solution with the mesh size h replaced by the equivalent mesh size \tilde{h} . The subscript i is merely the reference point along the beam at which the second derivative is required. For the second derivative, the reference point is a node. As will be shown shortly, the first derivative uses a reference point midway between two nodes.

Not only do the trigonometric finite differences greatly resemble the conventional derivatives, they approach them as λ , the variable wavelength parameter, goes to infinity. Stein and Housner included λ as a parameter independent from the process of solving for the buckling load. It can be chosen as whatever the operator wishes. The parameter does have some physical significance, as will be shown in Section IV. By choosing different λ 's, multiple buckling loads result, creating hope that the "exact" solution may be attained and not merely bounded. Choosing an optimal λ will be given further attention later. The bound established by the conventional finite differences can easily be established. Using the fact that $\sin\theta = \theta$ for small values of θ , then from

$$\lim_{\lambda \rightarrow \infty} \tilde{h} = \lim_{\lambda \rightarrow \infty} \frac{2\lambda}{\pi} \sin \frac{h}{2\lambda} \quad (3-28)$$

one obtains

$$\lim_{\lambda \rightarrow \infty} \tilde{h} = \lim_{\lambda \rightarrow \infty} \frac{2\lambda}{\pi} \frac{\pi h}{2\lambda} = h \quad (3-29)$$

Therefore, for large λ , the equivalent mesh \tilde{h} reduces to the conventional mesh h . With this, the trigonometric approximations reduce to the conventional approximations and the lower bound produced by conventional finite differences is achieved. By knowing the conventional solution, one may obtain a range of λ where the accuracy is better. Of added importance is the use of conventional procedures to determine the trigonometric equations, i.e. use of half-station or full-station approximations. Because the conventional error is known and the two methods behave the same in the limit, the same type of error can be expected in the trigonometric approach. This validates the usage of half- and full-station approximations in the first and second derivatives.

Application to the Virtual

Work Equation

The trigonometric finite difference derivatives just developed will be applied to the virtual work equation derived in Appendix A:

$$\int_0^L EI \frac{d^2W}{dx^2} \frac{d^2\delta W}{dx^2} dx = P \int_0^L \frac{dW}{dx} \frac{d\delta W}{dx} dx \quad (3-30)$$

where E is the Young's modulus, I is its inertia and P is the axial load which will cause buckling. The equation is to be solved for the buckling load $P = P_{cr}$. The virtual work equation cannot be integrated in closed form, so numerical integration is used. First, though, the beam is divided into a nodal mesh, with the nodes numbered as shown in Figure 4.

The nodes are represented by X's along the beam axis.

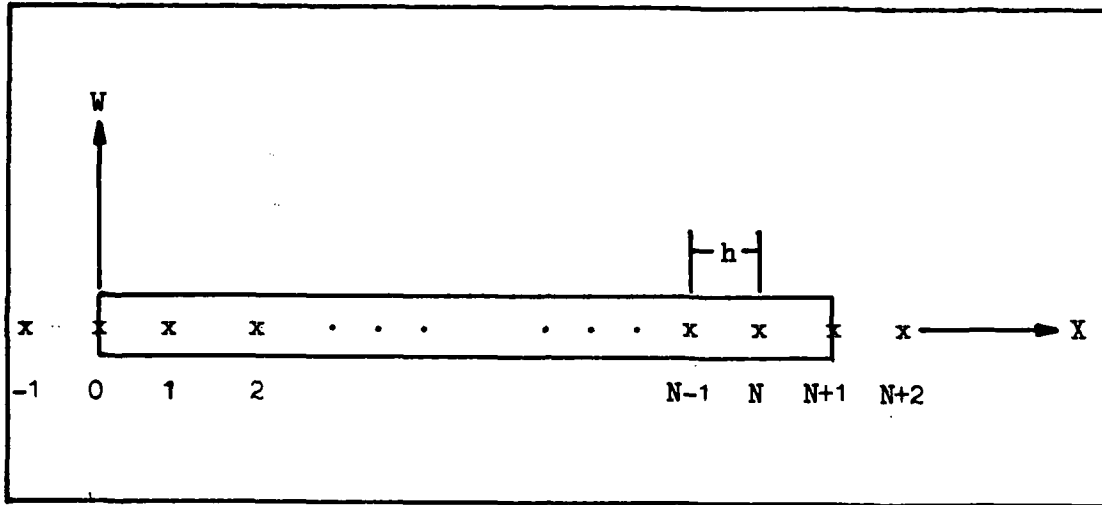


Fig 4. Node Pattern for N Internal Nodes

The distance between nodes is the mesh size h which equals the beam length divided by $N + 1$. N is the number of internal nodes. Nodes 0 and $N + 1$ are at the beam boundaries. Nodes -1 and $N + 2$ are fictitious external nodes which are required when applying the second derivative at a boundary.

The numerical integration used on the virtual work equation is the trapezoid rule. For ease in presenting the solution, the following definitions are made

$$f_i = E_i I_i W_i'' \delta W_i'' \quad (3-31)$$

$$g_i = W_i' \delta W_i' \quad (3-32)$$

where the subscript i is the same as used in developing the trigonometric derivatives. The virtual work equation can be thought of as:

$$\int_0^L f dx = P \int_0^L g dx \quad (3-33)$$

To integrate along the beam length L , assume the function f

is represented by the curve in Figure 5.

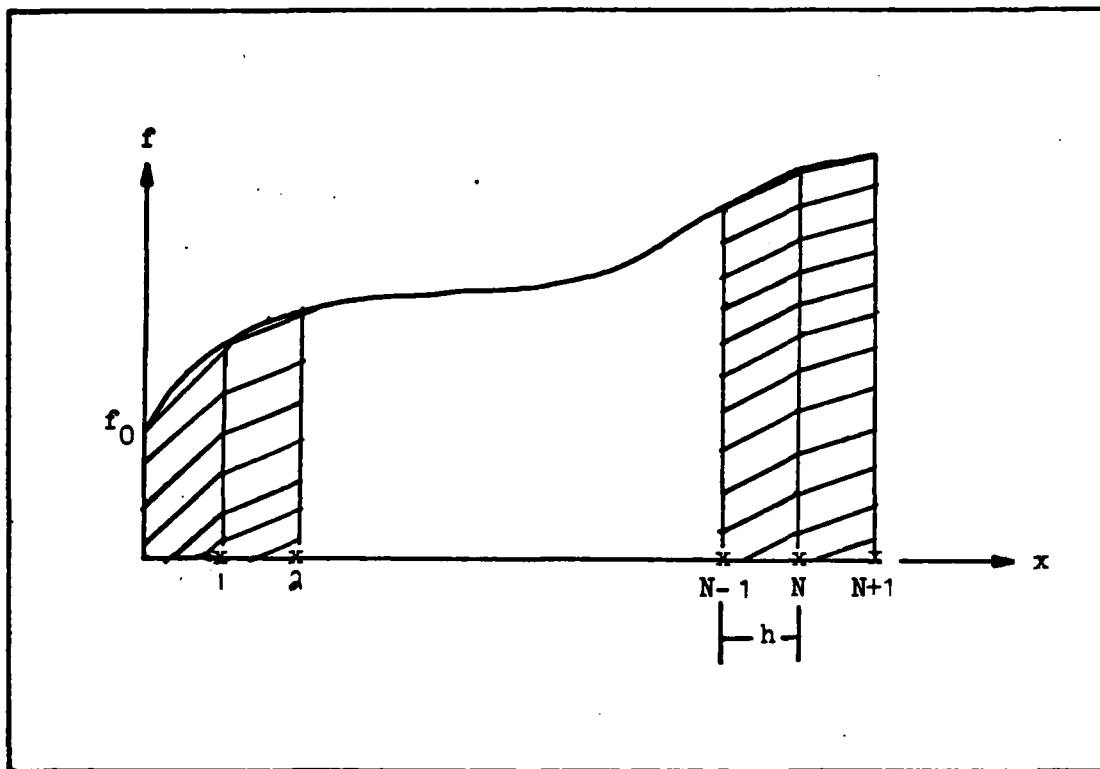


Fig 5. Numerical Integration of $f dx$
Using Full-Station Approach

By using the trapezoidal rule on Figure 5, the integral of $f dx$ can be represented as a summation over the beam's nodes:

$$h \left(\frac{1}{2} f_0 + \sum_{i=1}^N f_i + \frac{1}{2} f_{N+1} \right)$$

Likewise, numerical integration can be applied to the integral of $g dx$. This integration depends upon the values of g at points half-way between the node points because g is a function of half-station approximations. Figure 6 demonstrates this integration.

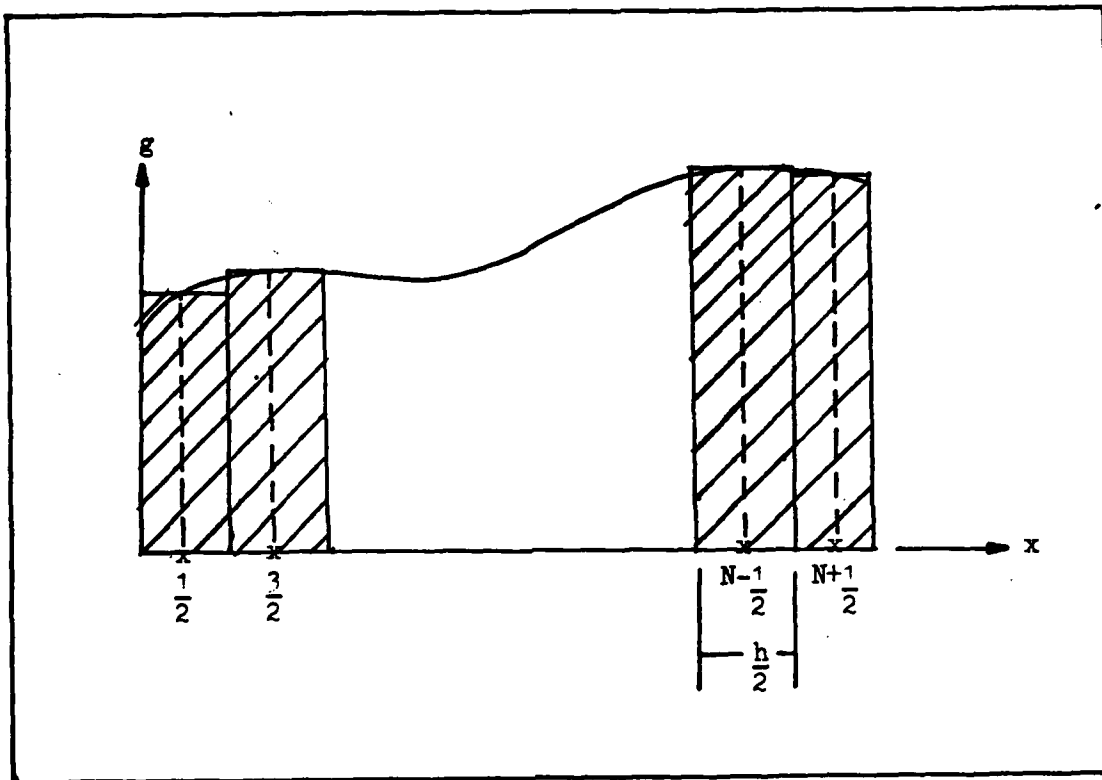


Fig 6. Numerical Integration of gdx
Using Half-Station Approach

The integral can be represented by

$$h \sum_{i=0}^N g_{i+\frac{1}{2}}$$

Replacing the virtual work integrals by these new expressions gives the equation

$$h \left(\frac{1}{2} f_0 + \sum_{i=1}^N f_i + \frac{1}{2} f_{N+1} \right) = Ph \sum_{i=0}^N g_{i+\frac{1}{2}} \quad (3-34)$$

The mesh size h is factored out of both sides of Eq (3-34). Using Eq (3-31) and Eq (3-32) and substituting the trigonometric derivatives, a definition for f_k , g_k is produced

$$f_k = \frac{E_k I_k}{h^4} (W_{k+1} - 2W_k + W_{k-1}) (\delta W_{k+1} - 2\delta W_k + \delta W_{k-1}) \quad (3-35)$$

$$g_k = \frac{1}{h^2} (W_{k+\frac{1}{2}} - W_{k-\frac{1}{2}}) (\delta W_{k+\frac{1}{2}} - \delta W_{k-\frac{1}{2}}) \quad (3-36)$$

for $k = 0$ to $N + 1$. The expressions in Eq (3-34) may now be defined in terms of the beam displacement W , stiffness E , and inertia I at each node in the beam. The solution of this equation will be the critical buckling load.

The summations in Eq (3-34) can be expressed using Eq (3-35) and Eq (3-36). By regrouping the coefficients of specific virtual displacements δW_i , the equation

$$\begin{aligned} & a_{-1} (P, E, I, W_{-1}, W_0, W_1) \delta W_{-1} + a_0 (P, E, I, W_{-1}, W_0, W_1, W_2) \delta W_0 + \dots \\ & \dots + a_{N+1} (P, E, I, W_{N-1}, W_N, W_{N+1}, W_{N+2}) \delta W_{N+1} \\ & + a_{N+2} (P, W_N, W_{N+1}, W_{N+2}) \delta W_{N+2} = 0 \end{aligned} \quad (3-37)$$

is produced. The a_i are functions of the axial load P and the actual displacements W in the neighborhood of node i . Also, the a_i are functions of E and I in the vicinity of i . Eq (3-37) can be written in the form

$$\sum_{i=-1}^{N+2} a_i \delta W_i = 0 \quad (3-38)$$

The trivial solution $\delta W_i = 0$ is ignored. The internal virtual displacements are arbitrary and are taken as non-zero. At the beam ends, the virtual work idea makes actual and virtual displacements compatible. For example, a beam pinned at the left boundary has the real boundary conditions $W(0) = 0$ and

$W''(0) = 0$. Because virtual boundary displacements must be compatible, $\delta W(0) = 0$ and $\delta W''(0) = 0$. Applying the finite difference derivatives gives

$$\delta W_0 = 0 \quad (3-39)$$

$$\delta W_{-1} = -\delta W \quad (3-40)$$

By applying the boundary conditions, external virtual displacements can be related to internal and boundary virtual displacements. Virtual displacements at the boundary are zero if pinned or clamped and undefined if free or guided. In this latter case, the virtual boundary displacement δW_0 or δW_{N+1} , depending on which boundary, produces an additional unknown and an additional equation. Applying the boundary equations reduces Eq (3-38) to an equation with N coefficients ($N + 1$ with a free or guided boundary, $N + 2$ with both boundaries free or guided)

$$\sum_{i=1}^N b_i \delta W_i = 0 \quad (3-41)$$

The b_i are functions of W , P , E , I as were the a_i in Eq (3-38). However, the actual boundary conditions are applied to the actual displacements in the a_i in the same manner as the virtual displacements. For a pinned left boundary, the conditions are

$$W_0 = 0 \quad (3-42)$$

$$W_{-1} = -W_1 \quad (3-43)$$

Applying the boundary equations, the expressions a_i are reduced to b_i . Once again, a free or guided boundary displacement is left as an unknown.

In Eq (3-41), all the virtual displacement may now be

treated as arbitrary. Because of this, the coefficients b_i must be zero. This reduces the virtual work equation to a set of N equations ($N + q$ where q is the number of free/guided boundaries) of the form

$$b_i = 0 \quad i = 1, 2, \dots, N \quad (3-44)$$

The b_i are functions of P , E , I and the actual node displacements W_i along the beam. By factoring out the actual displacements, Eq (3-44) can be represented in its matrix form.

$$\begin{bmatrix} C \end{bmatrix} \begin{bmatrix} W_1 \\ W_2 \\ \vdots \\ W_{N-1} \\ W_N \end{bmatrix} = 0 \quad (3-45)$$

The elements of C depend only upon E , I and P . Matrix C is of size $N \times N$ and is populated along and near to the diagonal. Once the values of E and I are known for each node in the beam, the eigenvalues of the matrix C can be solved for. Because Eq (3-45) is a set of homogeneous equations, setting the determinant of C equal to zero will produce N eigenvalues. Although the solution for buckling load yields an infinite number of values, only N are obtained from the determinant. This is due to the approximation of the beam continuum by N internal node points. By ordering the eigenvalues, the critical buckling load is found. It is P_{cr} , the lowest non-zero eigenvalue. A zero eigenvalue corresponds to rigid body motion, a non-buckling phenomenon.

Now that the C matrix is determined, it merely awaits some type of reduction to yield the buckling load. One simple technique involves checking the sign of the determinant of C. A guess is made at the value of the axial load P. It is inserted into the determinant and the sign of the determinant of C is checked. A larger P is assumed and the process is repeated. When the sign of the determinant of C changes, two bounds, one high and one low, are established for P. This process repeats until the determinant of C equals zero. The value of P for this condition is an eigenvalue of Eq (3-45). If it is the lowest eigenvalue, then P is the critical buckling load P_{cr} . However, as Franklin (26) shows, there are better ways to solve for the eigenvalues of the C matrix. This simple algorithm, though, helps to illustrate how it could be done. More sophisticated techniques for solving the eigenvalue problem include the method of elimination by triangularization, the method of Householder and Bauer, and the LR and QR methods (25,26).

The method used in determining both the critical buckling load (eigenvalue) and the corresponding mode shape (eigenvector) is from a prepared routine available in the International Mathematical and Statistical Libraries (IMSL). To use this routine, Eq (3-41) must be rewritten. The C matrix in Eq (3-41) contained E, I and the critical force P. This force P was evident in the right hand side of the virtual work equation

provides a method for looking at the effect a change in the beam has on its mode shape.

In the guided-free, guided-guided and free-free beams, rigid body motion can show up in both eigenvalue and eigenvector analysis. In the eigenvalue problem, a critical buckling load of zero is returned as a result of the rigid body translation. The computer is merely programmed to avoid this zero and return the next lowest eigenvalue. In eigenvector plots, rigid body motion affects the displacement curve by introducing a scaling factor. To avoid this in the guided-free beam, all displacements are re-scaled by subtracting the minimum nodal displacement (usually at the guided boundary) from a nodal displacement value and dividing this difference by $(1 - W_{\min})$. This rescales the nodal displacements and produces the expected curve. A similar technique is used for the free-free and guided-guided beam. An additional change is needed because the center of the beam, at $x = L/2$, does not have zero transverse displacement. This arbitrary translation is removed from the nodal displacements, producing the expected curve.

Summary

The eigenvalue matrix problem is now set up. It was derived from the use of a truncated Fourier series, featuring the variable wavelength parameter λ , in developing finite difference expressions. These expressions were applied to a beam at several nodes, permitting the numerical integration of the virtual work equation. The equations (3-41) and (3-42)

are the end result of this integration. By solving for the determinant of the C matrix in Eq (3-45), the eigenvalue P_{cr} and eigenvector W are obtained.

The forth section of the thesis will apply this technique to simple, uniform beams to verify the method before looking at more difficult problems. Besides verifying the approach, an attempt to determine a best wavelength parameter λ will begin.

IV. Uniform Beam Results

The first beams that were examined were the simple, uniform beams. These are beams which have a constant stiffness E and a constant moment of inertia I . Equation (3-46) was programmed for a computer. It allows for N internal nodes with constant or varying E and I . To test the program, it was run for the uniform beam as described above. Because E and I are constant, only the boundary conditions are different from beam to beam. The 10 boundary conditions considered are:

1. Pinned-pinned
2. Pinned-clamped
3. Pinned-guided
4. Pinned-free
5. Clamped-clamped
6. Clamped-guided
7. Clamped-free
8. Guided-guided
9. Guided-free
10. Free-free

For these 10 cases, the exact critical buckling load and mode shape are available through solving a governing differential equation which was not applied in this thesis. These results are well catalogued in literature (18-20,23,24).

Accuracy of the computer program has been checked by comparing the calculated buckling load and mode shape with the exact solutions. As discussed in Section III, the mode shape is actually a curve fitted through the deflection at each node of the beam. This mode shape is produced independent of the wavelength parameter λ . To show this, a discussion

of the accuracy of the critical buckling load must first be made.

Eq (3-46) consists of two matrices A and B. They were formed by numerically integrating the virtual work equation. Imbedded within both matrices is a dependence upon W_1, W_2, \dots, W_N and the corresponding virtual displacements. These were factored out, leaving Eq (3-46). The A matrix, consisting of f_k (Eq (3-35)) applications, now depends upon $E_k I_k$ and $1/h^4$. Likewise, the B matrix depends upon multiples of $1/h^2$, obtained by applying Eq (3-36). The equivalent mesh size $\tilde{h} = \frac{2\lambda}{\pi} \sin \frac{\pi h}{2\lambda}$. For the uniform beam, solutions are obtained with a "uniform" mesh. By choosing the desired number of nodes N within the beam, the beam is divided into a mesh with the distance between each node equal to h, where $h = (\text{beam length}) / (N + 1)$. Therefore, for a uniform mesh, h is constant throughout the beam. This was used earlier when h was divided out of Eq (3-34). As will be shown in Section VI, this simplification is not permitted when the mesh varies in size throughout the beam. Using the fact that h is a constant, fixed in size when N is chosen, \tilde{h} is dependent only upon the mesh size and is constant for a fixed wavelength. The equivalent mesh is only a function of h and λ , which are determined by the operator. The wavelength parameter is independent of E, I.

With the simplification of the uniform mesh beam, $1/h^4$ and $1/h^2$ will be factored out of the A and B matrices of Eq (3-46). This produces two matrices \tilde{A} and \tilde{B} .

$$\frac{1}{\tilde{h}^4} \begin{bmatrix} \tilde{A} \end{bmatrix} \begin{Bmatrix} W_1 \\ \cdot \\ \cdot \\ \cdot \\ W_N \end{Bmatrix} = \frac{P}{\tilde{h}^2} \begin{bmatrix} \tilde{B} \end{bmatrix} \begin{Bmatrix} W_1 \\ \cdot \\ \cdot \\ \cdot \\ W_N \end{Bmatrix} \quad (4-1)$$

Multiplying both sides of Eq (4-1) by \tilde{h}^4 , ... (defining $k = P\tilde{h}^2$) results in an equation similar in form to Eq (3-46).

$$\begin{bmatrix} \tilde{A} \end{bmatrix} \begin{Bmatrix} W_1 \\ \cdot \\ \cdot \\ \cdot \\ W_N \end{Bmatrix} = k \begin{bmatrix} \tilde{B} \end{bmatrix} \begin{Bmatrix} W_1 \\ \cdot \\ \cdot \\ \cdot \\ W_N \end{Bmatrix} \quad (4-2)$$

The eigenvalue of the problem is no longer P_{cr} , the axial buckling load, but k . This equation is solved for the lowest non-zero value of k , the critical axial buckling parameter. From the definition of k and \tilde{h} , the buckling load P_{cr} can be written in the form

$$P_{cr} = \frac{k_{cr}}{\left(\frac{2\lambda}{\pi} \sin \frac{\pi h}{2\lambda}\right)^2} \quad (4-3)$$

This equation highlights one of the main advantages of Stein and Housner's truncated Fourier series. The eigenvalue equation does not return a single critical buckling load for N nodes as does the conventional finite difference equation. Instead, the eigenvalue equation returns a value for k_{cr} which permits P_{cr} to become a function of λ . By choosing a λ , a critical load is returned. This is the basic advantage of the Fourier series coupled with λ . By choosing a good λ it may be possible to obtain a P_{cr} better (more accurate) than the conventional finite difference method generates. And if λ is just

right, the "exact" solution may be obtained. The question of what is a good wavelength parameter will be discussed further in this Section.

In addition to determining the buckling load, it is sometimes desirable to determine the corresponding mode shape. By using the IMSL routine described in Section III, the eigenvector can be determined for either Eq (3-46) or Eq (4-1). For the uniform mesh beam, Eq (4-1) is used. The eigenvector corresponding to each of the N eigenvalues is stored and is available upon request. Because this thesis is mainly concerned with eigenvalue determination, the methods of eigenvector determination will not be discussed. For my purpose, if an eigenvector is needed, it will be that one returned by the IMSL package. The eigenvector is of interest though, because it is independent of the wavelength parameter. As was just shown, the \tilde{A} and \tilde{B} matrices have no direct λ dependence. Instead, they depend on the buckling parameter k_{cr} which was a constant in the eigenvalue solution. Therefore, the eigenvector delivered depends upon \tilde{A} , \tilde{B} and k_{cr} . The eigenvector is independent of λ . In the computer program, the buckling mode shape is determined before the operator decides on what λ or range thereof he is interested in. Because of this, even though a poor λ may be chosen, resulting in a poor P_{cr} , the mode shape is independent of the λ .

Uniform Beam Solutions

As stated in the introduction to this section, 10 cases of a uniform beam were studied to verify the designed computer

program. These 10 cases differed only in the boundary conditions, the wavelength parameter λ was usually varied between 0.2 and 2.0. This produces a range of P_{cr} , according to Eq (4-3). Also, the conventional finite difference solution was calculated to provide a comparison with the trigonometric solution. The conventional solution can be found by letting $\lambda \rightarrow \infty$, or in the uniform beam case, replacing \tilde{h} by h . Because \tilde{h} was factored from the matrix equation (4-1), this substitution is easily accomplished.

Figures 9 through 12 at the end of this Section compare the buckling load curve, produced by varying λ , with the conventional solution. Because the correct solution is known, the percent error of the buckling load is plotted versus the wavelength parameter. Because the conventional finite difference solution is independent of λ , it is represented as a dashed line of constant error. Also, a zero error line is included which allows for ease in comparison and in determining the best wavelength parameter. Although 10 cases were examined, several combinations of boundary conditions produced the same curve. As an example, pinned-pinned and free-free boundaries produce the same buckling load curve. Therefore, only the four independent curves are included. The boundary combinations they represent are included in the figure title.

In addition to buckling load curves, the calculated eigenvector is plotted for five boundary combinations. Once again, one eigenvector can represent several different boundary combinations. As a check on the accuracy of the eigenvector,

the exact buckling shapes are plotted on the same figure. Results are shown in Figures 13 through 18.

For ease in calculation, several parameters were normalized. For simplicity, E and I , variables within the A matrix, were defined as 1.0. Because the beam is uniform, E and I do not change. They are represented as the ratios of E/E_{\max} and I/I_{\max} which accounts for the normalization.

The beam length L is also normalized as $L/L_{\text{beam}} = 1.0$. In Section V, discontinuities are introduced which make this practice of normalization quite useful. Also, the user is not forced to choose specific numerical values for E , I and L . The critical buckling load is represented by $P_{\text{cr}} = m EI/L^2$ with the value of m returned by Eq (4-3). Once the solution is in this form, the user can choose any values of E , I and L desired, without having to solve Eq (4-2) for each specific case.

Using these techniques, the 10 uniform cases were solved for P_{cr} and the buckling mode shape. A few of the results are discussed here.

Pinned-Pinned

The most common column buckling problem is the uniform pinned-pinned column. This problem is usually the first buckling problem a student sees. For analysis, two cases were run. Nine internal node points were used in one case, Figure 9, and 19 in another. Choosing these numbers of internal nodes results in a mesh size of 0.1 and 0.05, for a beam of length equal to one. It can be seen that 19 nodes provides a mesh

twice as fine as for $N = 9$ nodes. The nine node beam is shown in Figure 7 with its buckled mode shape superimposed.

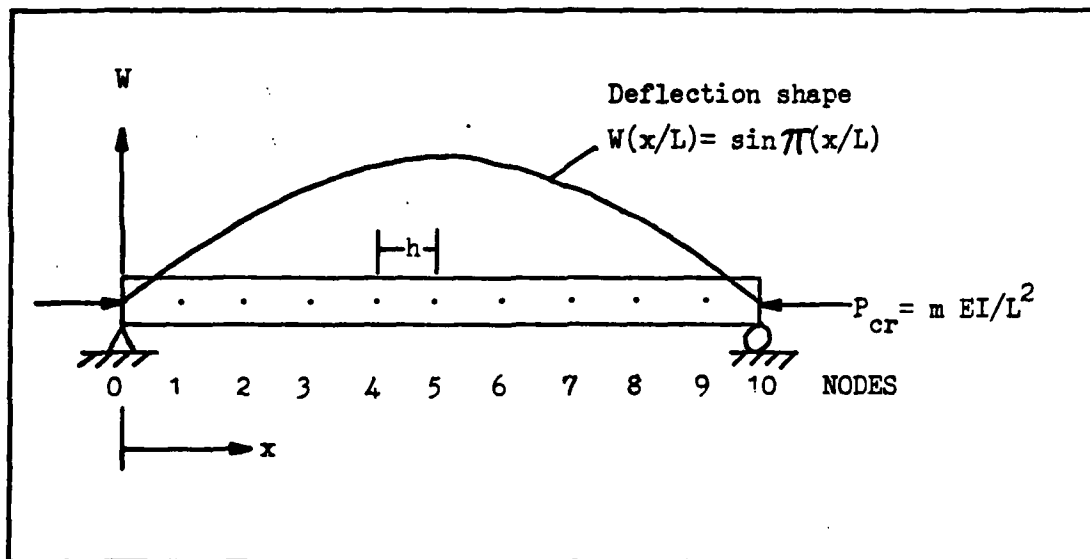


Fig 7. Pinned-Pinned Beam with Nine Nodes

The critical buckling load is given in literature by the formula

$$P_{cr} = (n\pi)^2 \frac{EI}{L^2} \quad n = 1, 2, 3, \dots \quad (4-4)$$

The lowest P_{cr} is given for $n = 1$ which produces $P_{cr} = \pi^2 EI/L^2 = 9.8696044 EI/L^2$. The nine node solution results in values of P_{cr} more accurate than the conventional finite difference for the range of $.71 < \lambda < \infty$, approximately. Also, the exact buckling load is calculated when $\lambda = 1.0$. At this value of the wavelength parameter, Eq (4-3) returns $m = 9.8696044$ which matches the known solution for $n = 1$.

In addition to matching the buckling load, the eigenvector that is produced exactly matches the known mode shape $W(X/L) = \sin \pi(X/L)$. Actually, the nodal displacements lie on this curve, with the computer producing a curve through them.

For 19 internal nodes the same results are obtained, but

with greater accuracy. Once more, at $\lambda = 1.0$ the exact solution is returned. For the range $.71 < \lambda < \infty$, P_{cr} is more accurate than the conventional solution. For this same range, the 19 node buckling curve is more accurate than the nine node curve. Finally, the eigenvector matches the known mode shape again.

In both cases, $\lambda = 1.0$ resulted in the exact solution. This value of λ can be related to the known buckled shape. If the beam problem were solved explicitly with L non-dimensionalized, the exact solution would occur at $\lambda = 1.0L$. The fact that λ is a wavelength parameter gives a clue to its nature. If the sine curve of the buckling mode shape were extended beyond $X = L$, it would have a wavelength of $2L$. Its half-buckled wavelength would be L , which corresponds to the optimum value of λ . The idea of λ_{opt} corresponding to the half-buckled wavelength will be checked further.

Guided-Guided

A second type of beam that was checked is one in which both boundaries are guided, that is, the boundary is free to translate vertically, but must retain zero slope (dw/dx) at each end. Although the beam is not common, it does provide a check on solutions produced for more exotic configurations.

The exact solution for the guided-guided beam is given as $\pi^2 EI/L^2$ for the lowest eigenvalue P_{cr} . For nine internal nodes, the value of $\lambda = 1.0$ produced a solution accurate to π^2 within 10 significant figures. For engineering purposes, this is the exact solution. When compared with the conventional solution, the trigonometric finite differences were more

accurate for the range $.71 < \lambda < \infty$. Figure 9 demonstrates this behavior. The same result occurs for 19 internal nodes, with an improved accuracy range of $.71 < \lambda < \infty$. Once again, the optimal value of λ is 1.0. How well does this compare to the mode shape?

The exact mode shape is $W(X/L) = \cos\pi(X/L)$. Once the problem of rigid body translation was accounted for, the eigenvectors for the two mesh sizes matched the expected mode shape. This is particularly encouraging because no nodal displacement was known ahead of time. In pinned and clamped beams, the displacement at the boundary is known (equal to zero). This provides less unknowns for the program to handle. With guided and free boundaries, the displacement is left as an unknown. In all guided and free cases though, the computer returned the correct displacement.

From the exact and generated mode shapes, a half-buckled wavelength of L is evident. Therefore, choosing λ equal to half of the buckled wavelength produces an exact solution.

General Results

Ten combinations of boundary conditions were tested on the simple uniform beam. In each case, the exact buckling load could be found by "proper" choice of the wavelength parameter (the optimal λ , λ_{opt}). Also, the eigenvector exactly matched the equivalent points on the known mode shape.

The number of nodes used to model the beam depends upon the user and how much time and money are available. For this thesis, time and money had no real effect on the number of

nodes chosen because of the simplicity of the beam. Although using more nodes takes longer, the increase is not noticeable. The key features to remember in choosing N nodes are the increase in accuracy and the increase in the size of the generated matrices. Also, it is convenient to have a node at the point of maximum deflection. This produces a smoother eigenvector shape. Otherwise, the maximum deflection will not be correctly displayed.

The computer handles Eq (4-2) which involves reducing matrices of order $N \times N$. Increasing the number of nodes will increase the range of λ for a good solution (compared to the conventional solution), improve the buckled mode shape by returning more nodal displacements, but will raise the number of elements in the A and B matrices. For $N = 9$ nodes, in a pinned-pinned beam there are 81 elements. With 19 nodes, there are 381 elements. As I stated before, the change from $N = 9$ to $N = 19$ has no significant change on the cost to the user for these simple beams. But the point must be kept in mind when working with more complicated beams and with complex structural elements (plates, shells) to which this technique can be applied.

Nine nodes were chosen to produce the results in Figures 9 through 18. Using nine nodes gave a convenient mesh size (.1L) and produced fairly accurate buckling load plots and eigenvectors. As Hannah demonstrated, even a lower number of nodes, such as five, will produce an exact answer. However, the choice of λ must be good because the optimal range of λ

shrank by choosing fewer nodes. So although the exact answer is available, the choice of λ can greatly affect your error.

For the 10 beams analyzed, the range of λ for which P_{cr} was more accurate than the conventional solution was checked. These results are listed in Table I under the heading λ range. In all cases, the choice of λ which gave the exact buckling load corresponded to half of the buckled wavelength. This is the same feature as seen in literature under the effective buckling length idea (18).

TABLE I

| BOUNDARIES | λ_{opt} | λ range |
|-----------------|-----------------|-----------------------------|
| Pinned-pinned | 1.0 | .71 < λ < ∞ |
| Pinned-clamped | .632 | .45 < λ < ∞ |
| Pinned-guided | 2.0 | 1.42 < λ < ∞ |
| Pinned-free | 1.0 | .71 < λ < ∞ |
| Clamped-clamped | 0.5 | .36 < λ < ∞ |
| Clamped-guided | 1.0 | .71 < λ < ∞ |
| Clamped-free | 2.0 | 1.42 < λ < ∞ |
| Guided-guided | 1.0 | .71 < λ < ∞ |
| Guided-free | 2.0 | 1.42 < λ < ∞ |
| Free-free | 1.0 | .71 < λ < ∞ |

If the buckling wavelength of the mode shape is not known, a choice of $\lambda \approx 1.4$ gives results better than the conventional approach. This result is seen by comparing the ranges of λ in Table I. In addition, merely choosing a large λ will result in better accuracy. For a large λ , the solution is most likely a lower bound on P_{cr} and therefore a conservative answer.

The general behavior of the P_{cr} vs λ plots in Figures 9 to 12 explains the previous statement. It also explains why an exact solution is always obtainable for the beam analyzed within the bounds of the model used. Figure 8 typifies the behavior of P_{cr} vs λ for the uniform beams.

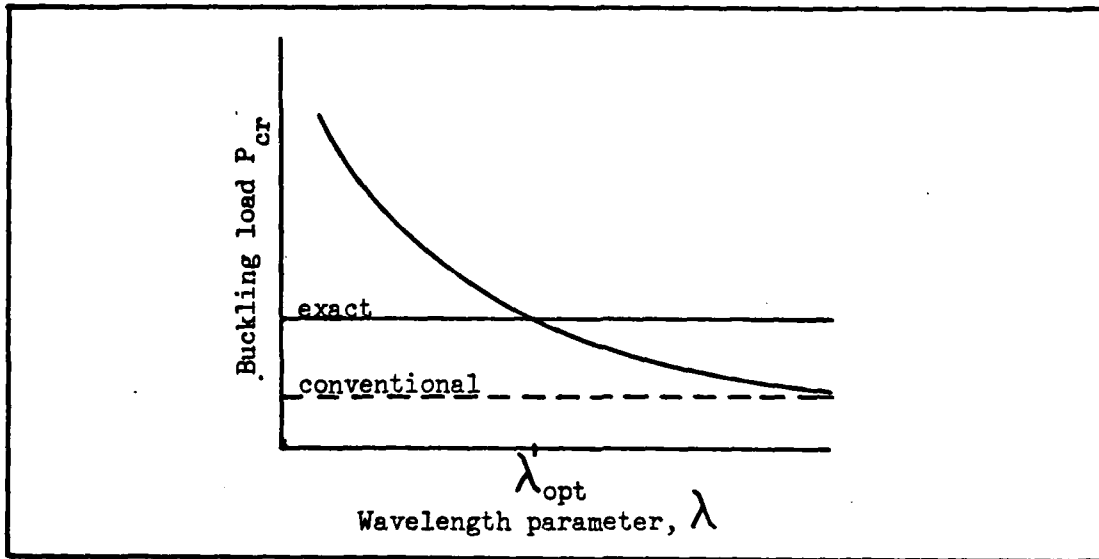


Fig 8. Buckling Load Versus Wavelength Parameter

Each curve plotted showed a very large buckling load for $\lambda = 0.1, 0.2$. This can be explained using Eq (4-3), rewritten here for reference.

$$P_{cr} = \frac{k_{cr}}{\left(\frac{2\lambda}{\pi} \sin \frac{\pi h}{2\lambda}\right)^2} \quad (4-3)$$

The computer returns k_{cr} , independent of λ . Although the buckling load curve is smooth in all the figures, there are singularities for small λ . These singularities occur when

$$\frac{2\lambda}{\pi} \sin \frac{\pi h}{2\lambda} = 0 \quad (4-5)$$

Solutions to Eq (4-5) occur for

$$\lambda = 0 \quad \text{or} \quad \frac{\pi h}{2\lambda} = n\pi \quad n = 0, 1, 2, \dots \quad (4-6)$$

The first singularity, at $\lambda = 0$ is generally not a problem. Setting the wavelength equal to zero would be of no use. This leaves the second part of Eq (4-6). The singularities generated by it are

$$\lambda = \frac{h}{2n} \quad (n = 1, 2, \dots) \quad (4-7)$$

This forms a sequence of singularities from near zero out to $\lambda = h/2$. For $\lambda > h/2$, no singularities exist. This value of $\lambda(h/2)$ provides a good start for a P_{cr} vs λ plot. Below $\lambda = h/2$, singularities occur. At $\lambda = h/2$, $P_{cr} = \infty$. For the uniform beam plot, the curves started at $\lambda = .2$ because the nearest singularity was at $\lambda = 0.05$ ($h = .1$). This helped avoid the extremely large values of the buckling load in this region.

On the other end of the curve is the conventional finite difference solution. The conventional solution is always a lower bound. Modeling the beam by nodes breaks the beam continuum into a finite number of degrees of freedom, making the beam more flexible than the continuum. This increased flexibility helps the beam to buckle at a lower value of P_{cr} than the continuum beam would. Therefore, the conventional solution is always lower than the true solution.

Eq (4-6) at $n = 0$ implies $\lambda = \infty$ is a singularity. However, Eq (3-29) showed that as $\lambda \rightarrow \infty$, $\tilde{h} \rightarrow h$. Therefore, a very large λ reduces the trigonometric solution to the conventional solution and not to a singularity.

The fact that the exact solution is attainable is easily explained now. At $\lambda = h/2$, the value of P_{cr} is positive infinite. As $\lambda \rightarrow \infty$, the critical load reduces to that determined by the conventional solution, which is lower than P_{cr} exact. Therefore, the buckling load curve starts higher than the exact solution and ends up lower than the exact solution. By

the mean value theorem, the curve must pass through the exact solution for some λ , $h/2 < \lambda < \infty$.

Physically, increasing λ results in a buckled mode shape of longer wavelength. A smaller force is required to buckle a beam with this longer wavelength. Therefore, the buckling load decreases with increasing λ .

Summary

By analyzing the simple uniform beam, several results have been achieved.

- 1) The equation that generates the solution successfully predicted the buckling load and mode shape for 10 known cases, for an optimal λ .
- 2) The optimal λ was half of the buckled wave shape. If the shape is unknown, a $\lambda \approx 1.4$ will give a better solution than the conventional finite difference.
- 3) The exact buckling load always lies somewhere on P_{cr} vs λ curve.
- 4) The exact solution was obtained at the same λ for $N = 9$ or 19 . However, $N = 19$ provides a larger range of good λ and more points for the eigenvector mode shape.

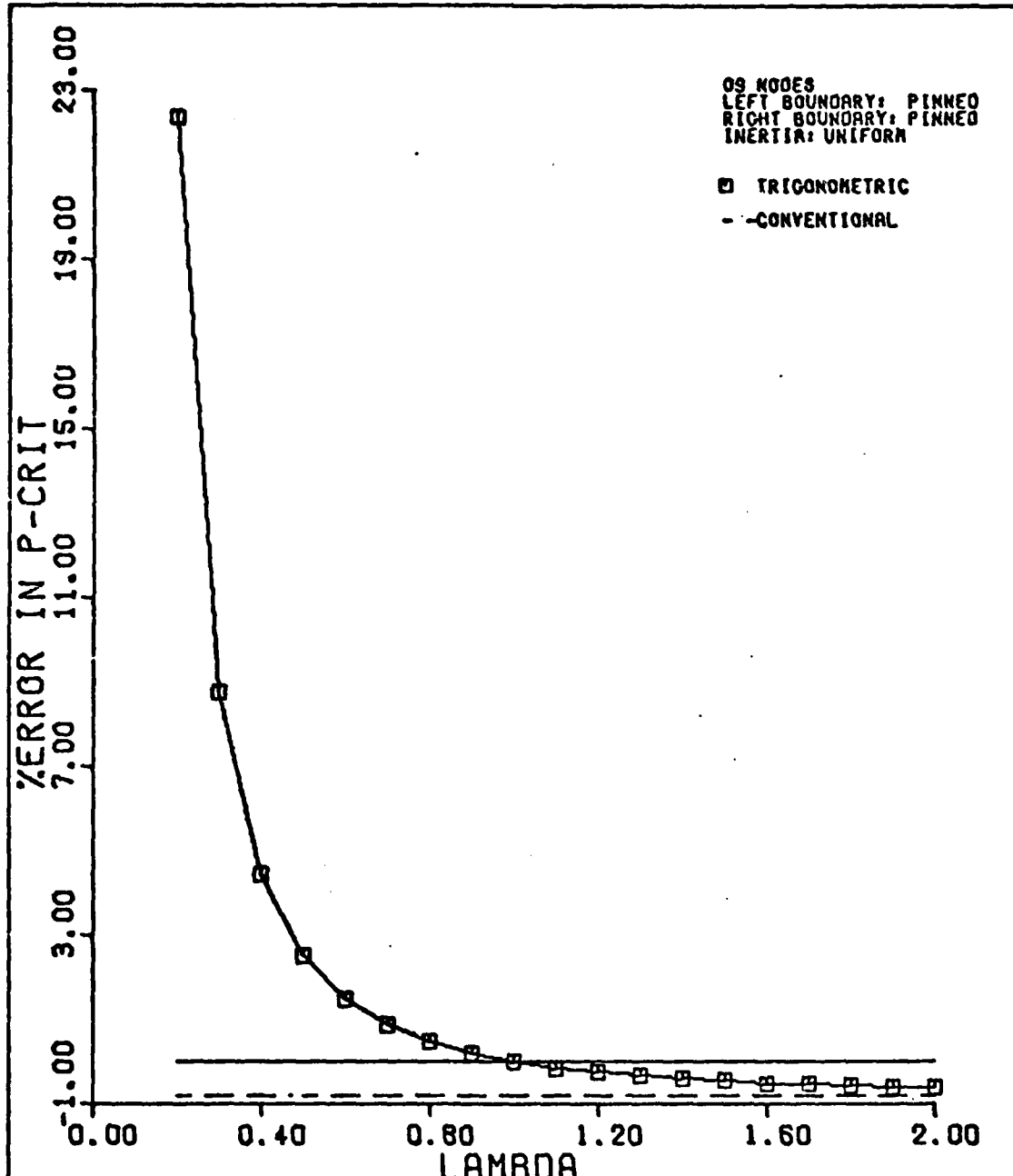


Fig 9. Buckling load curve comparing error for trigonometric and conventional solutions with the known solution (represented by the solid line). This plot is representative of the pinned-pinned, pinned-free, clamped-guided, guided-guided, and free-free beam solutions. $\lambda_{opt} = 1.0$

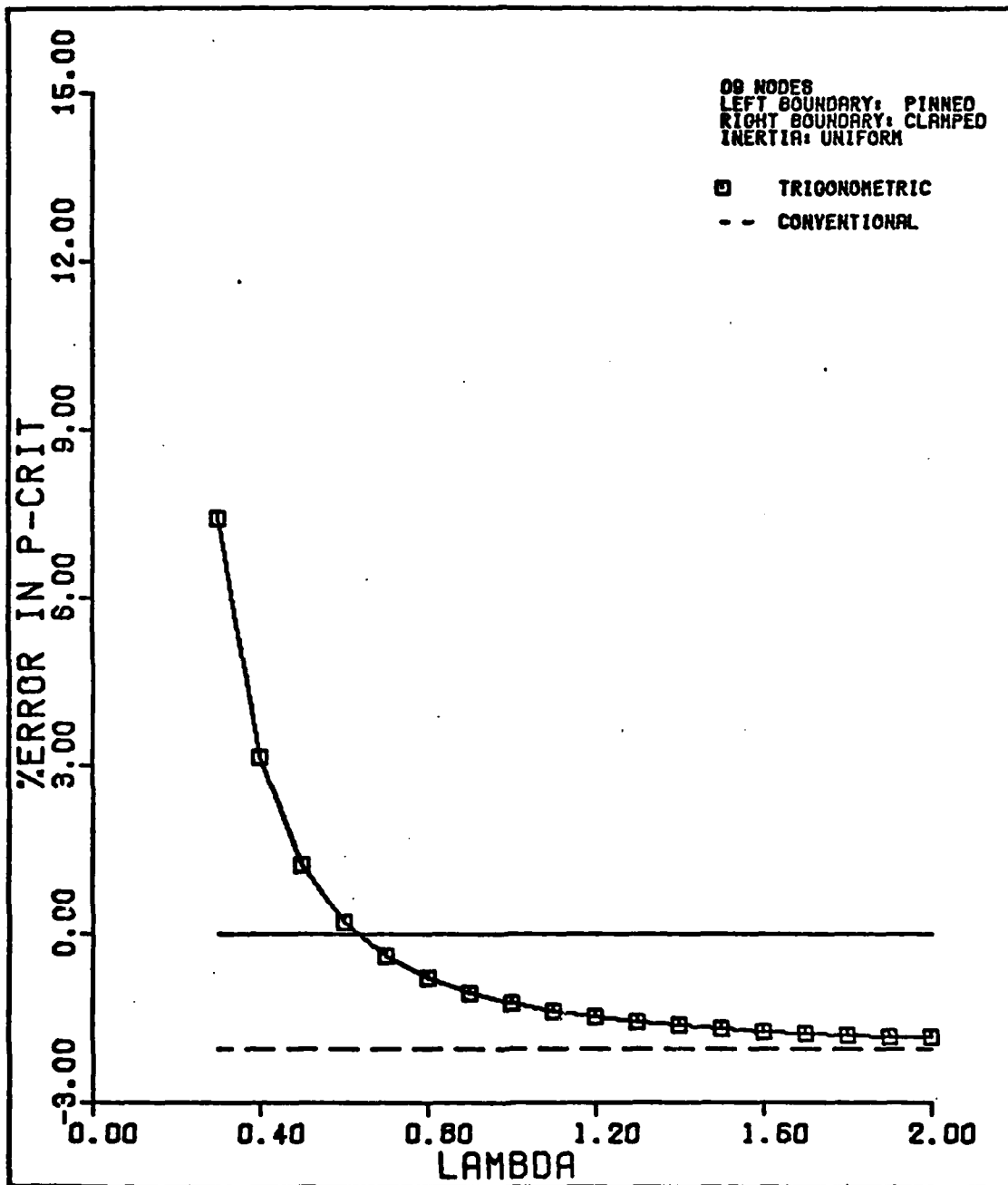


Fig 10. Buckling load curve comparing error for trigonometric and conventional solutions with the known solution (represented by the solid line). This plot is representative of the pinned-clamped beam, $\lambda_{opt} = .63$.

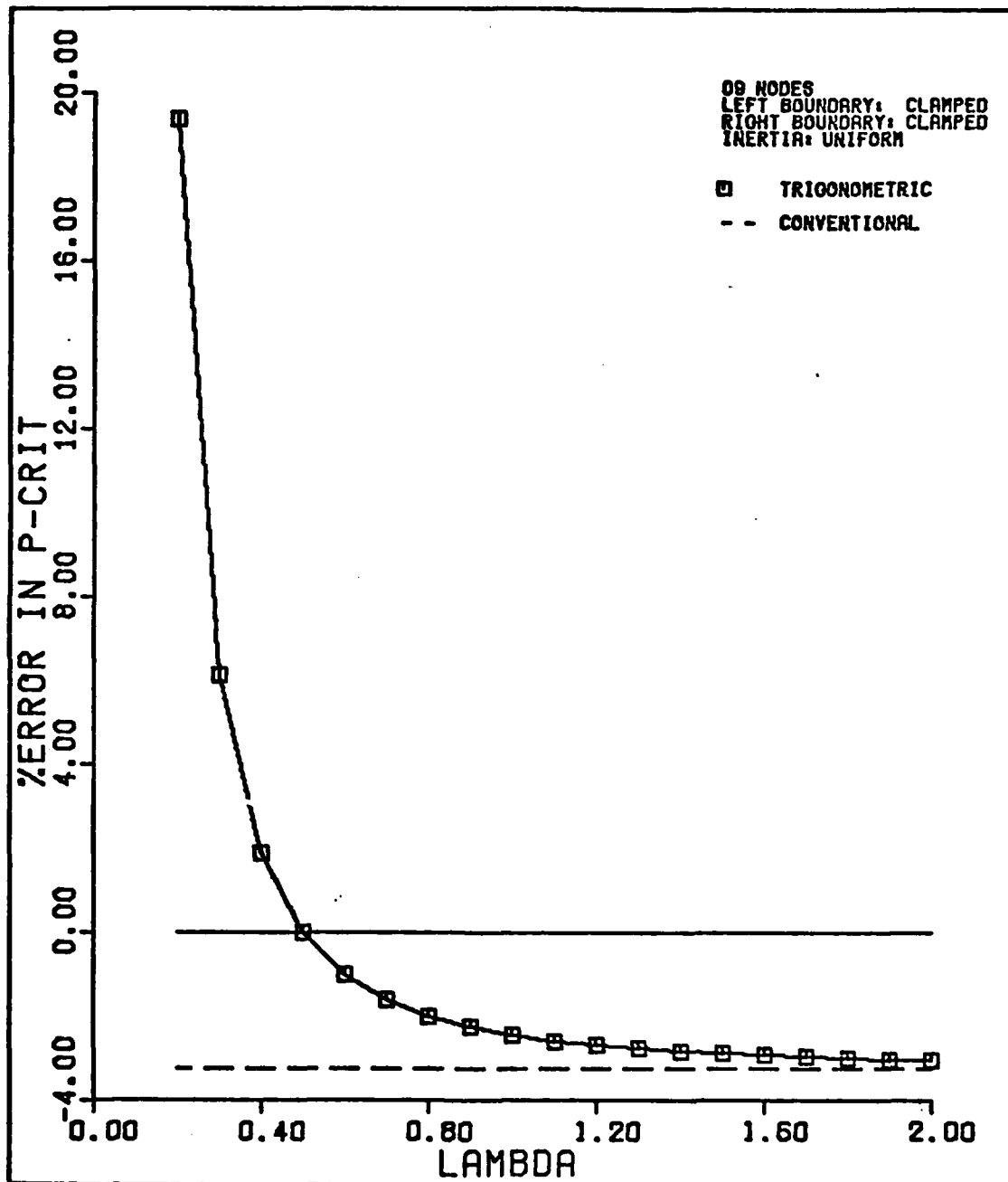


Fig 11. Buckling load curve comparing error for trigonometric and conventional solutions with the known solution (represented by the solid line). This plot is representative of the clamped-clamped beam, $\lambda_{opt} = .5$.

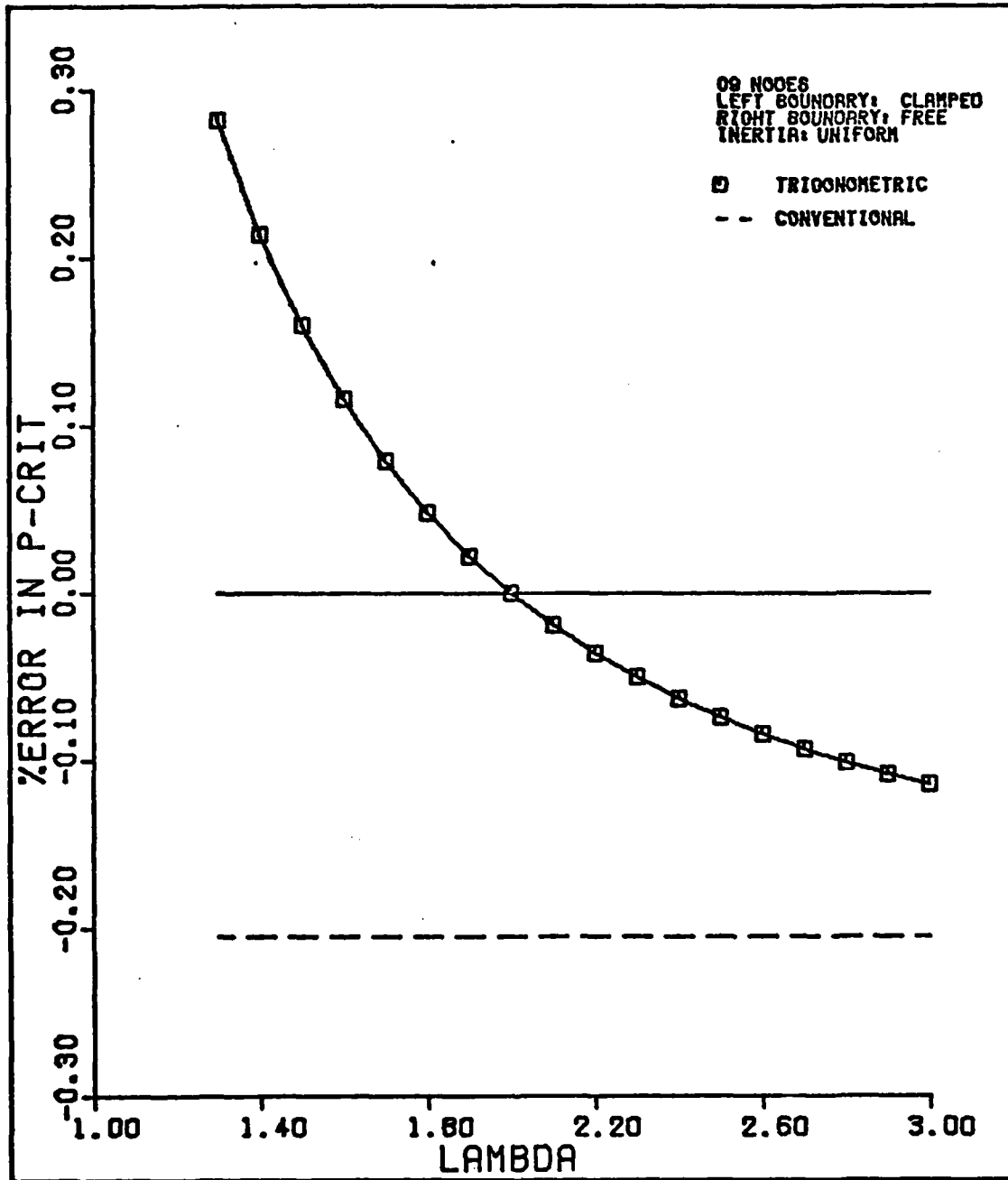


Fig 12. Buckling load curve comparing error for trigonometric and conventional solutions with the known solution (represented by the solid line). This plot is representative of the clamped-free pinned-guided, and guided-free beams, $\lambda_{opt} = 2.0$.

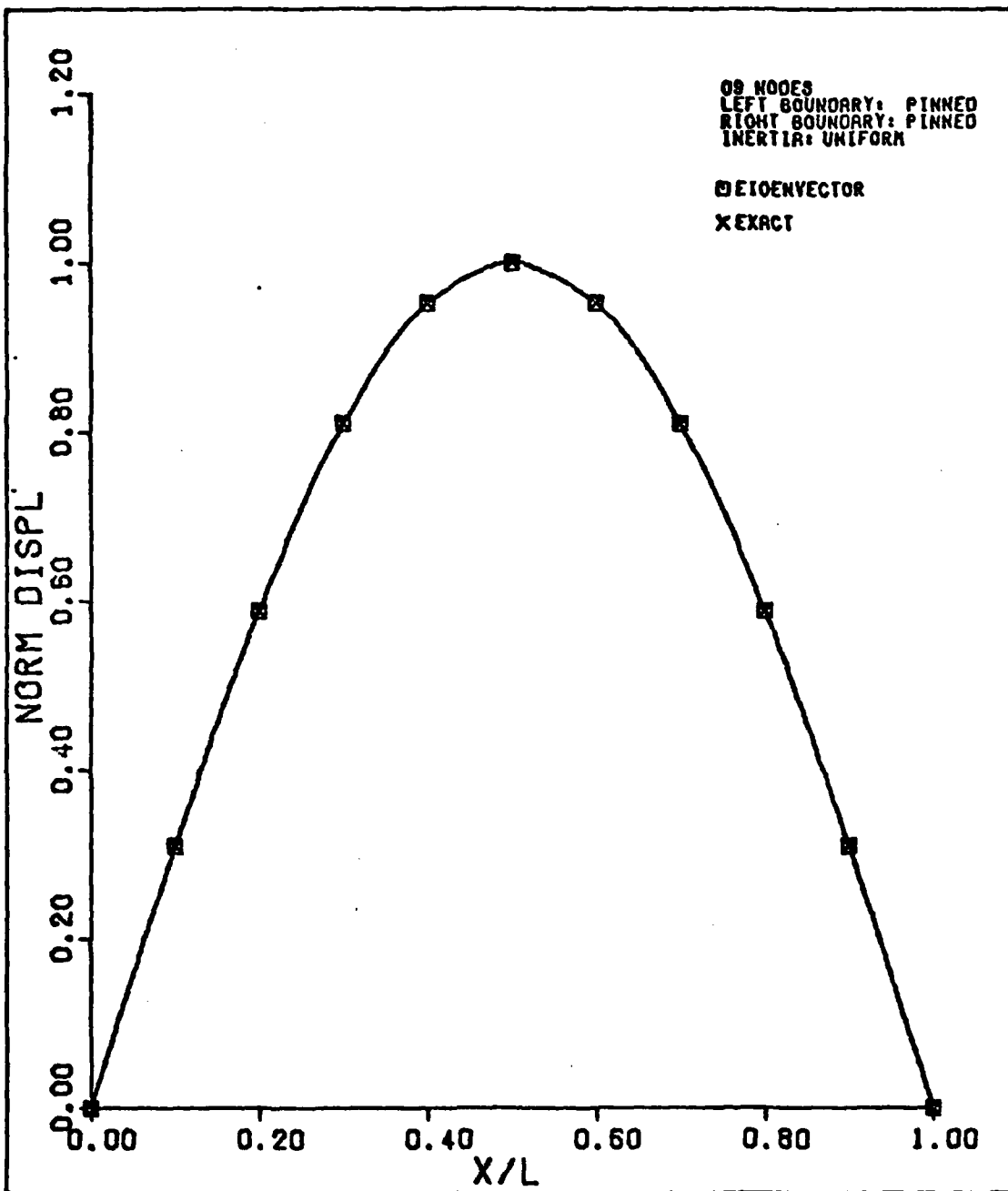


Fig 13. Comparison of the calculated eigenvector versus the exact mode shape. This plot represents the pinned-pinned, pinned-free, guided-guided, and free-free beam.

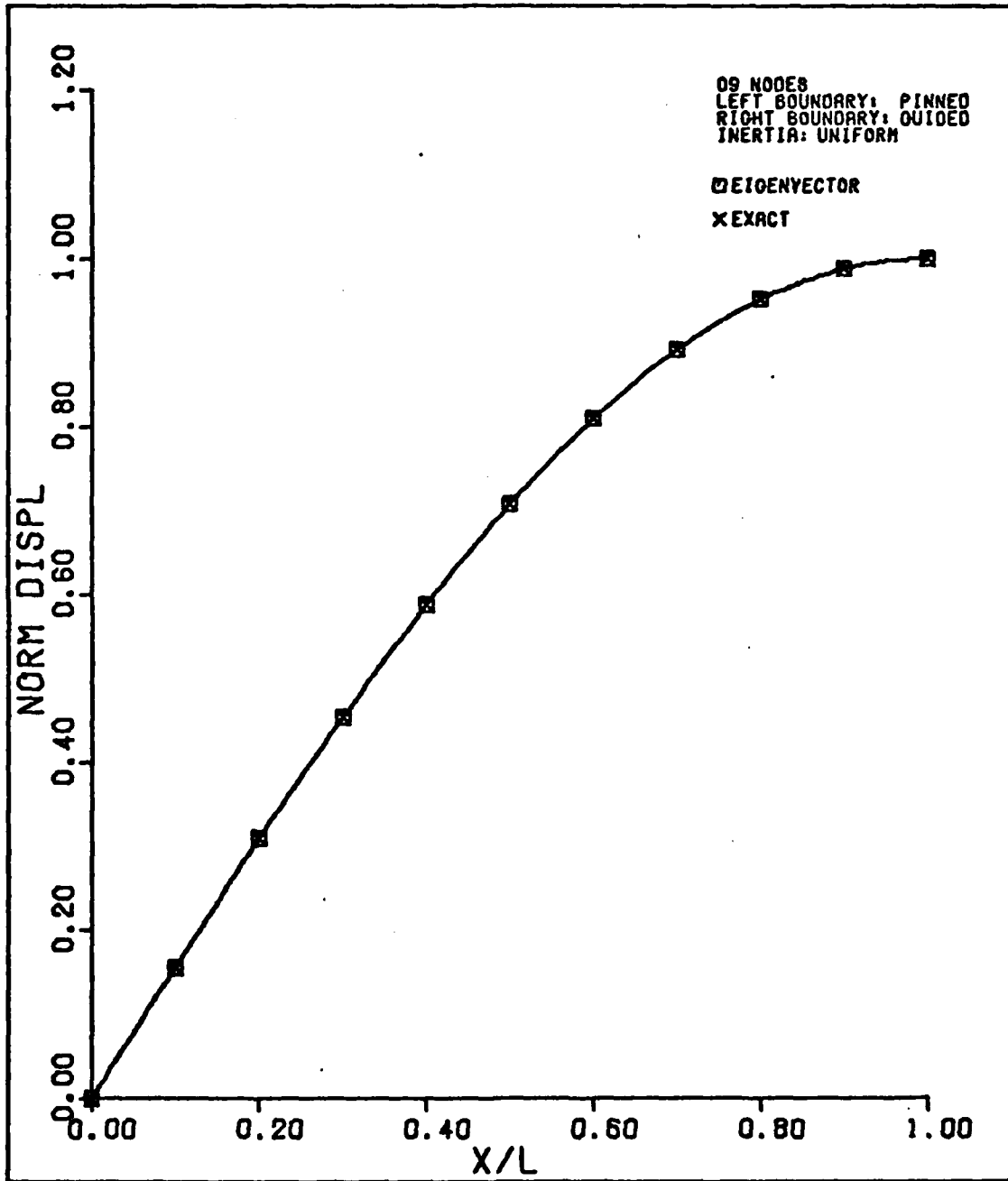


Fig 14. Comparison of the calculated eigenvector versus the exact mode shape. This plot represents the pinned-guided or guided-free beam.

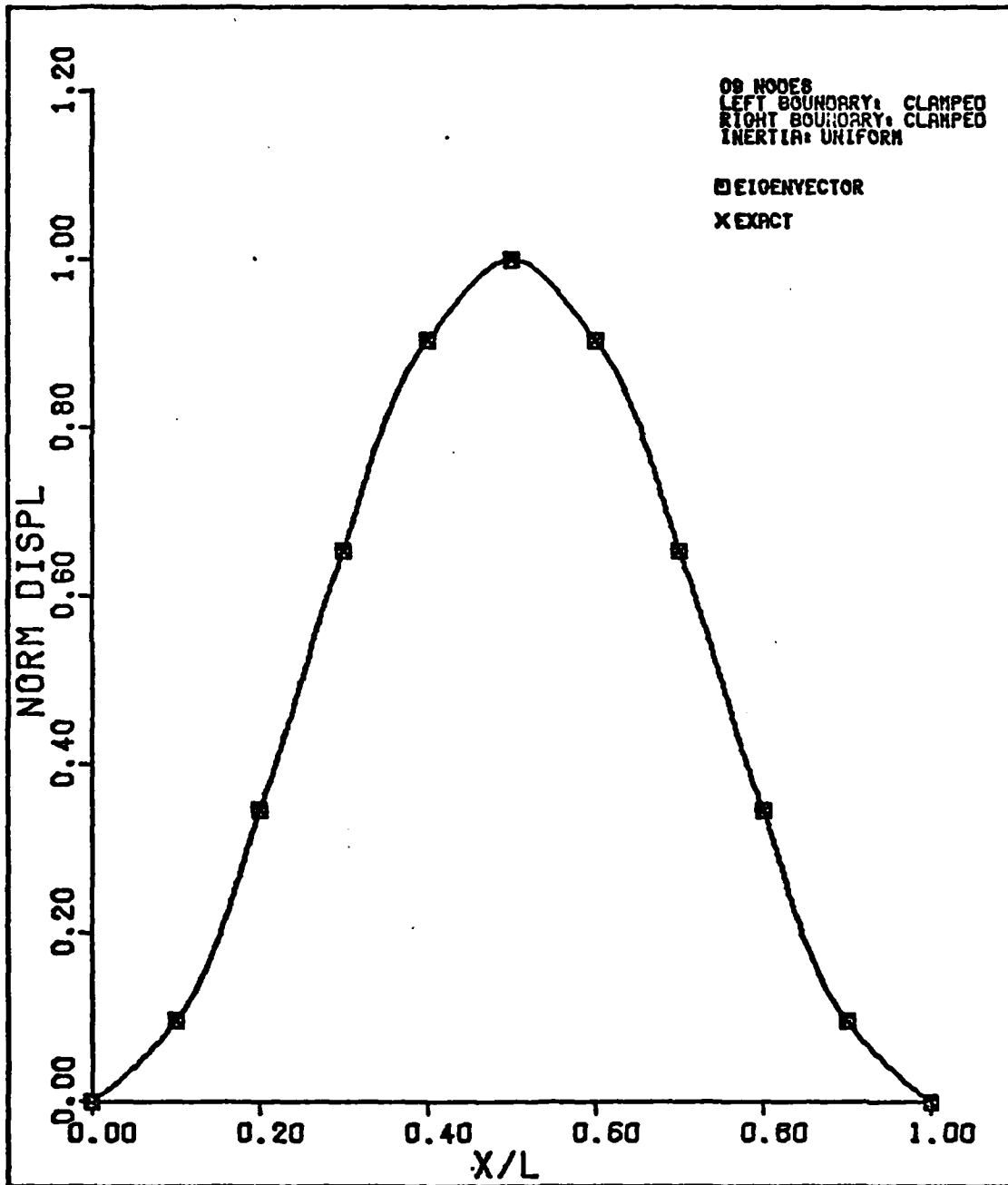


Fig 15. Comparison of the calculated eigenvector versus the exact mode shape. This plot represents the clamped-clamped beam.

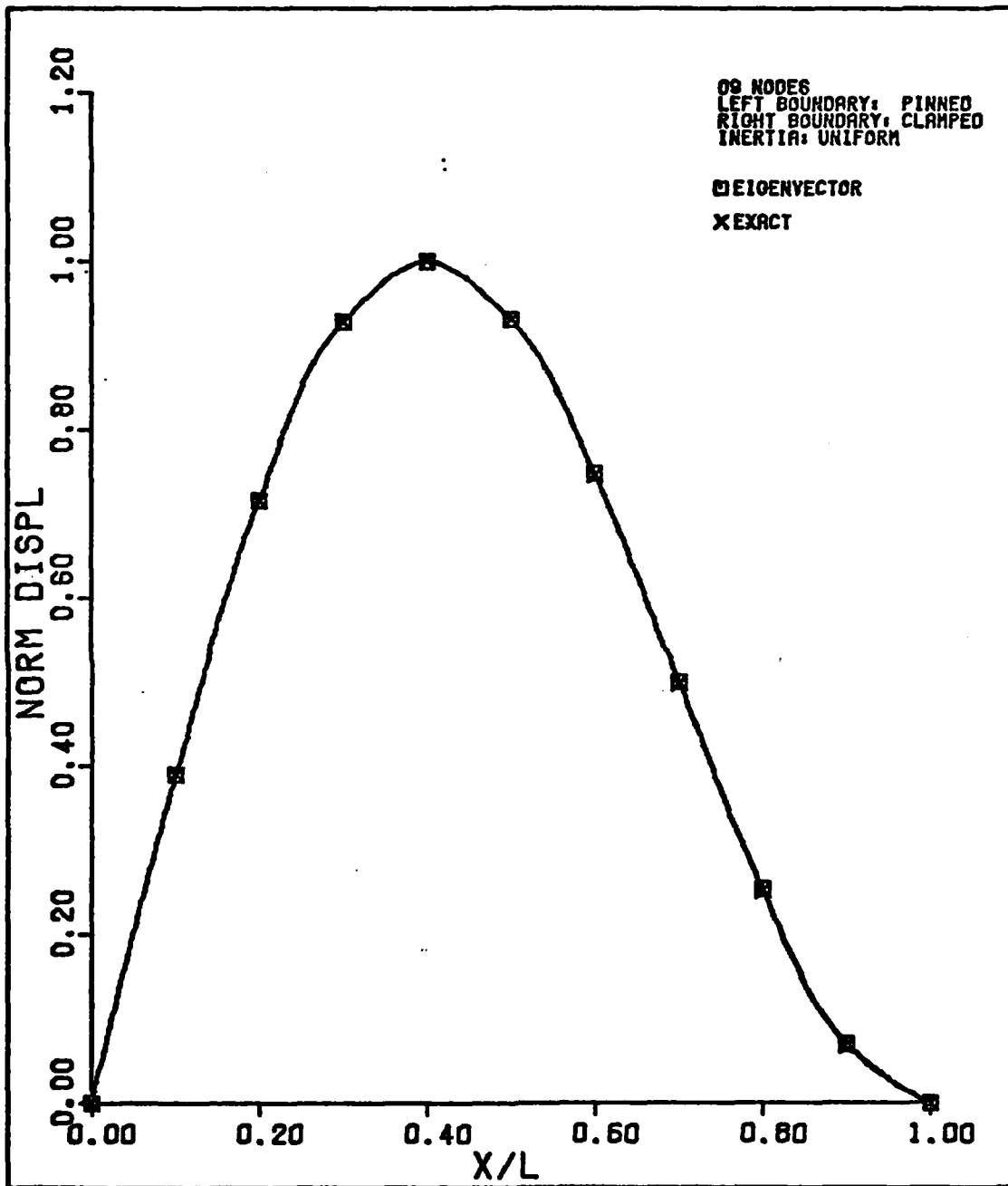
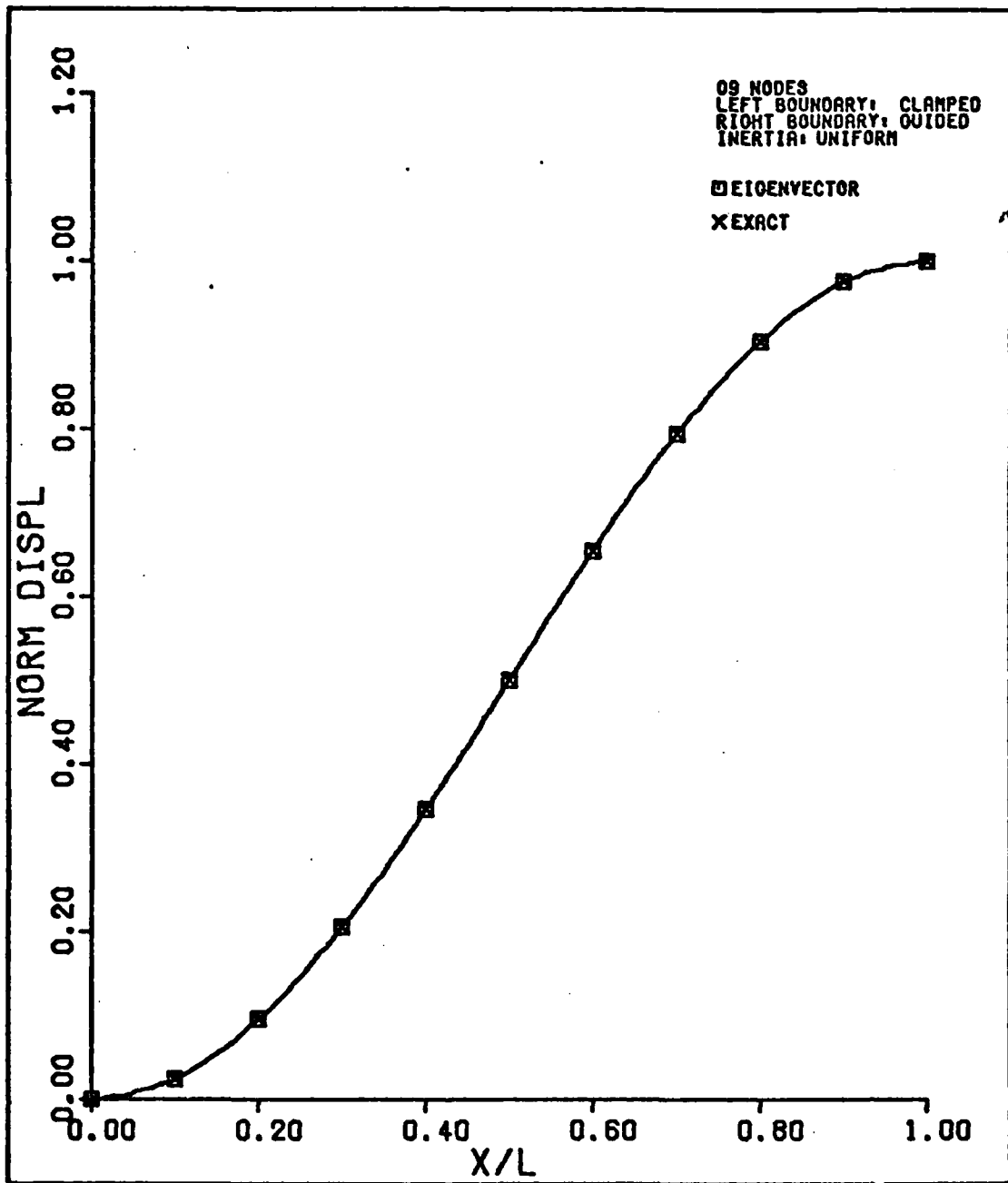


Fig 16. Comparison of the calculated eigenvector versus the exact mode shape. This plot represents the pinned-clamped beam.



. Fig 17. Comparison of the calculated eigenvector versus the exact mode shape. This plot represents the clamped-guided beam.

V. Beams With Variable Inertia

Introduction

The previous section dealt with simple uniform beams. They were used to verify the equation that governs eigenvalue determination as well as the computer program used to solve that equation. The uniform beams tested had a constant moment of inertia. If the beam's inertia can be increased over its middle, a higher load will be required to cause buckling. The beam is now a more stable structure, compared to its uniform cousin. In doing so, however, a beam with a variation in its moment of inertia results. Often the cross-section changes abruptly, resulting in a discontinuity of the inertia (22). A discontinuity of this type occurs in steel structures, where a beam is strengthened by riveting additional plates or angles along portions of the beam.

One of the improvements modeled in the thesis is the ability to handle changes in inertia. The moment of inertia $I(x)$ is regarded as a function of x , measured along the beam's axis. The use of I in this manner includes it within the integration of the virtual work equation, Eq (3-30). Inertias along the beam are now imbedded within the matrix equation, Eq (3-45).

This section of the thesis makes use of these abilities by examining continuous and discontinuous changes in inertia.

In some cases the exact buckling load is known beforehand, in others it is only bounded. In each case, the inertia at some point along the beam is defined as unity and the remaining inertias are expressed as the ratio with respect to that datum. The solution that is generated is a function of the chosen inertia. As was done last section, E and L are defined as one for simplicity.

The buckling load P_{cr} versus buckling wavelength λ is plotted for several cases to check the trigonometric finite difference accuracy, when possible. In addition, the search for the λ corresponding to the critical load will be discussed.

Optimization of λ

For several of the cases to be examined, only a bound on the solution is available in the literature. The wavelength parameter corresponding to the buckling load bound can be determined from the P_{cr} vs λ plot for the beam. But that P_{cr} is not the best solution. Eventually, the technique of this thesis will be applied to buckling problems with no known solution. What will be the buckling load then?

In the uniform beam analysis, a range of 1.4 to infinity for the buckling wavelength gave fairly good results for all boundary conditions. This technique of looking for a trend can be extended by comparison with known solutions to variable inertia beams. Eventually, a rule of thumb for λ can be developed. The corresponding critical load may be fairly good.

A promising procedure for determining an optimal buckling

wavelength is put forward by Stein and Housner in regards to plate buckling (2). The technique is applicable to beam buckling.

A trial solution is performed for a beam modeled by N nodes, equally spaced throughout the beam. The value of the critical buckling load is determined at several wavelengths, establishing the familiar buckling load curve, P_{cr} vs λ . The process is repeated with a different number of internal nodes M . The buckling load curve is superimposed on the one obtained for N nodes and is shown in Figure 18.

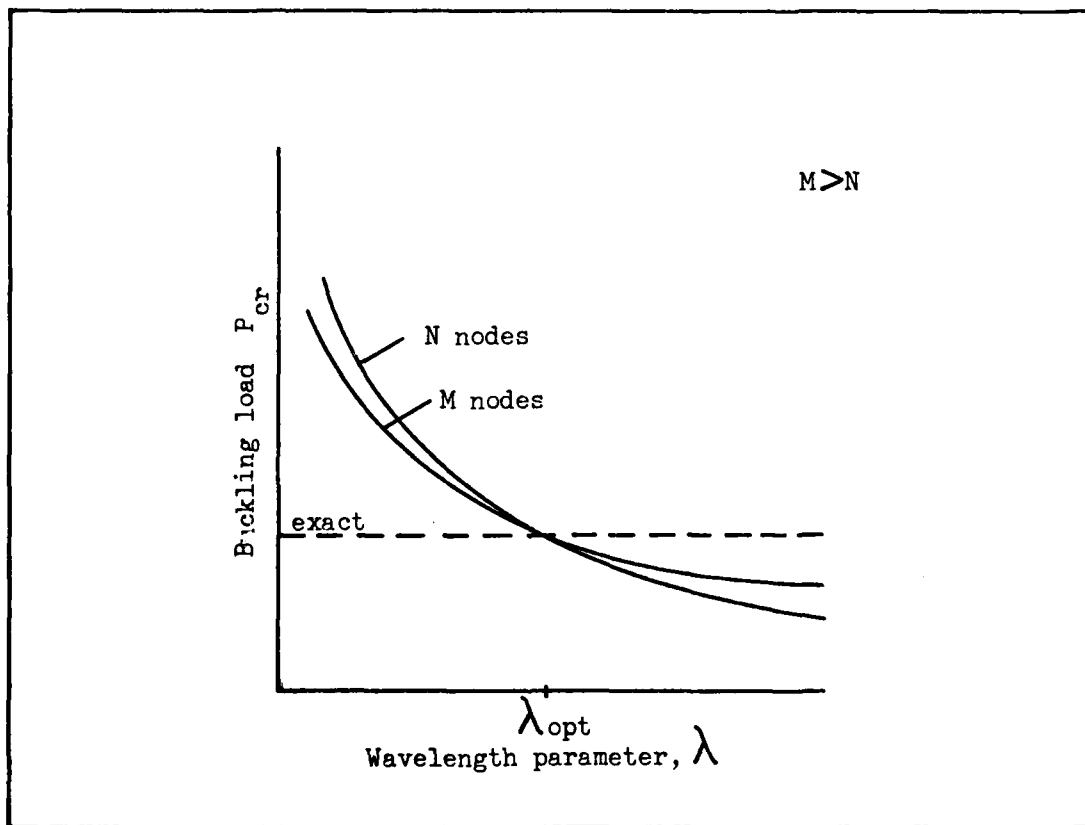


Fig 18. Optimization Curves for Buckling Wavelength

In the previous section, the optimal wavelength corresponded to half of the wavelength of buckled mode shape. For a beam which is non-uniform in inertia, the wavelength ceases

to have any physical significance. To find the optimal wavelength, Figure 18 is made use of. The value of λ at which the two curves cross indicates that convergence of the buckling load solution is relatively best at this value since for this wavelength, increasing the number of nodes produces no change in the buckling load. Increasing the number of nodes will return an improved solution at every wavelength, unless the wavelength corresponds to the exact buckling load. At λ_{opt} in Figure 18, increasing the number of nodes had no effect.

With this optimization method in mind, two sets of beams with a uniform mesh, continuous and discontinuous inertia, are examined.

Continuous Inertia

For a beam with continuously varying inertia, each node along the beam requires a specific inertia. Two examples are discussed in which the moment of inertia is defined by a simple formula.

A. Sinusoidal Variation. Brogan and Almroth (18) give a buckling solution for a pinned-pinned beam with a sinusoidal variation in inertia. The beam illustrated in Figure 19, has an inertia defined as

$$I(x) = I_0 \left(1 + \sin \frac{\pi x}{L} \right) \quad (5-1)$$

A one term approximation to the solution yields $P_{cr} = 1.825\pi^2 EI_0 / L^2$. This is higher than the solution for a pinned-pinned beam with constant inertia I_0 , which was found to be

$P_{cr} = \pi^2 EI_0 / L^2$ in the previous section, as is expected.

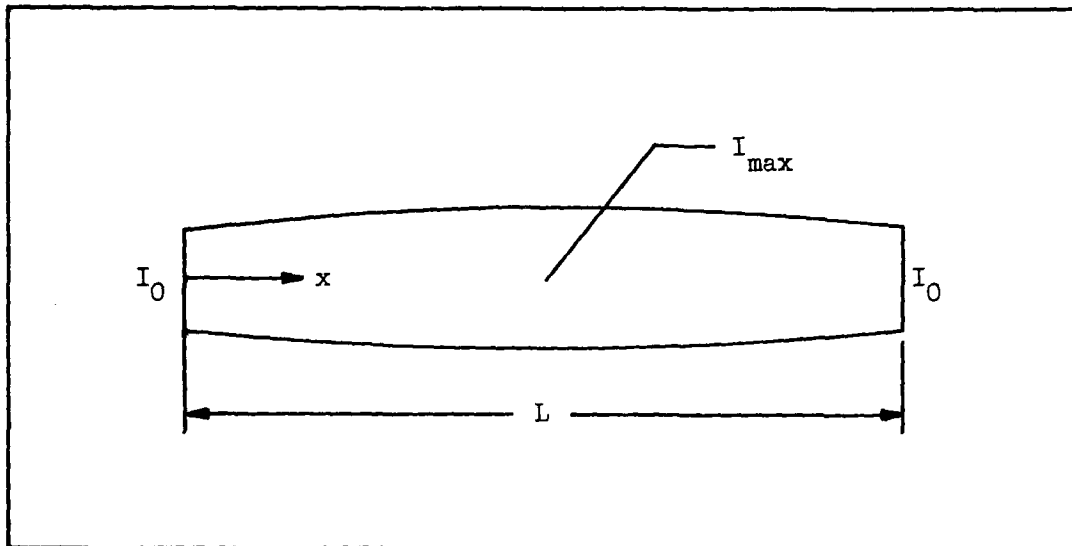


Fig 19. Sinusoidal Variation in Inertia

To model the beam, nine internal nodes were used. The x -coordinate of each node was calculated, allowing use of the inertia formula to calculate $I(x)$. Using the approximate solution as a guide, the range $.75 < \lambda < \infty$ provides answers more accurate than the conventional finite difference solution. Because the solution is not precisely known, the optimization technique is tried. The first curve generated was for nine nodes. The number nine was chosen because it places a node at the position of maximum inertia, in much the same way as a node at maximum deflection of the uniform beam was needed to fully model the mode shape. With this concept as a guide for choosing another set of nodes, the choice of $N = 11$ was made. Any odd number of internal nodes will place a node at the center. Although this requires a second solution to the eigenvalue equation, the size of the matrix is not much larger than for $N = 9$. Size depends, in general, upon N^2 as was

shown earlier. The two matrix sizes combined are still smaller than one corresponding to $N = 19$ and may produce a better solution.

For $N = 11$, the range of wavelengths for which the trigonometric series is more accurate shrinks to $.8 < \lambda < \infty$. The shrinkage is expected. As N increases, the conventional solution improves slightly faster than does the trigonometric approach. However, to get the conventional solution very close to the buckling load requires many nodes, whereas the trigonometric solution requires only a good choice of wavelength with fewer nodes.

The curves generated for $N = 9$ and 11 are shown in Figure 23. They intersect at $\lambda = 1.018$. The corresponding buckling load is $1.8268\pi^2 EI_0 / L^2$, slightly higher than lower bound using Rayleigh - Ritz. For this non-uniform pinned-pinned beam, the optimization technique worked well.

Two more solutions were obtained using 10 and 12 nodes. These nodal arrangements do not model the maximum moment of inertia. Directly comparing the buckling curves produced for $N = 10$ and 12 provides a buckling solution of $1.827\pi^2 EI_0 / L^2$ at $\lambda = 1.01$. Comparing the curves for $N = 9$ and 10 , which have on- and off-center nodes, results in $P_{cr} = 1.8267\pi^2 EI_0 / L^2$ at $\lambda = 1.02$. These results show that an accurate solution can be found if both curves use the same nodal arrangement, i.e. both curves have on-center or off-center nodes, in this example. Comparing dissimilar nodal arrangements ($N = 9, 10$) resulted in a fairly good solution also. This was not expected and will

be checked with the next model.

An additional nodal arrangement, $N = 5$, was checked. The range of improved accuracy over the conventional solution increased to $.73 < \lambda < \infty$. Comparing the curve of P_{CR} vs λ with another on-center solution ($N = 9$) gives the same solution as with $N = 9$ and 11. Therefore, in some cases, fewer nodes could be used to predict the critical load.

One final note on the sinusoidal pinned-pinned beam. As discussed in the introduction to this section, a beam built-up in the center would buckle at a higher load than its uniform counterpart. This is seen for the sinusoidal beam which buckles at about $1.827\pi^2 EI_0/L^2$ versus $1.0\pi^2 EI_0/L^2$ for its uniform inertia cousin. What is surprising though is that the ranges for a good choice of λ and the optimal wavelength itself are close to the uniform pinned-pinned beam. Perhaps a uniform beam can serve as a good guide in the choice of λ . This would be advantageous because results for all 10 combinations of boundary conditions are well known.

B. Exponential Variation. Sinha and Chou (17) present several solution methods for the axial buckling load of a pinned-pinned beam with an exponentially varying moment of inertia. The beam, similar to that illustrated in Figure 19, has an inertia defined as

$$I(x) = I_0 e^{2x/L} \quad \text{for } 0 \leq x \leq \frac{L}{2} \quad (5-2)$$

The beam is symmetric about the mid-section.

The exact solution for the axial buckling load, using the same assumptions embodied in this thesis, is given in

terms of the Bessel functions.

$$J_0(n)Y_1(ne^{-\frac{1}{2}}) - J_1(ne^{-\frac{1}{2}})Y_0(n) = 0 \quad (5-3)$$

where

$$n^2 = P_{cr} L^2/EI_0 \quad (5-4)$$

Solution of Eq (5-3) yields the beam buckling load as $1.9634\pi^2EI_0/L^2$. This is a higher buckling load than was found for the sinusoidal variance because the inertia is larger in the beam center.

The beam is modeled with an odd number of nodes so that the maximum inertia, at the beam's center, is included. The first mesh tried was $N = 9$. The inertia at each node was calculated using Eq (5-2). The wavelength range for which the trigonometric solution is more accurate than the conventional solution is $1.04 < \lambda < \infty$, with the calculated solution at $\lambda = 1.475$.

Although the exact solution is known and helped verify the ability to generate an accurate critical load, it provides an opportunity to try the two curve optimization again. A second nodal arrangement, $N = 11$, is applied to the problem. When superimposing the $N = 9$ and 11 curves in Figure 24, the intersection occurs at $\lambda = 1.48$ with a corresponding solution of $P_{cr} = 1.9628\pi^2EI_0/L^2$. This solution is within .031% of the calculated solution of Eq (5-3) and is most likely a combination of error in solving the eigenvalue problem and solving for n in Eq (5-4). A change in n of -.014% would give the solution returned by the intersection of the two curves. Because the tables used to solve Eq (5-3) were accurate for n

only to one part in a thousand, the exact solution cannot be calculated as closely as the intersection did. Therefore, the two curve intersection gives what can be termed an exact solution.

As was done for the sinusoidal beam, two solution curves corresponding to $N = 10, 12$ (off-center nodes) were generated. The intersection of these two curves produced $P_{cr} = 1.963\pi^2 EI_0 / L^2$ at $\lambda = .88$, which is fairly close to the result from $N = 9, 11$ except the buckling wavelength is quite different. The major difference from the sinusoidal beam is the lack of an intersection between the curves for $N = 9, 10$ and $N = 9, 12$. These curves are shown in Figures 25 and 26. The sinusoidal beam did return a solution for the buckling load when comparing meshes with nodes on- and off-center. The exponential beam does not produce this result. Normally, conventional solution accuracy improves as more nodes are used because the beam continuum is modeled by more points. Therefore, increasing the number of nodes will raise the conventional solution, which is the asymptote of the buckling load curve. If the number of nodes increases, and the conventional solution improves, the two buckling curves will intersect. Failure to model the same points of interest may result in a decrease in the conventional solution for an increase in the number of nodes. The buckling load curves will not intersect in this case. For nine nodes, the trigonometric buckling load curve approached $P_{cr} = 1.955\pi^2$, the conventional solution. For $N = 10$ and 12 , the buckling loads are $1.946\pi^2$ and $1.951\pi^2$ respectively. Comparing $N = 9$ and 10

or $N = 9, 12$ shows the decrease in load for an increase in nodes. Therefore, no intersection will result. There is an increase in the conventional load from $N = 10$ to 12 , accounting for the solution mentioned earlier for the two meshes. An intersection with $N = 9$ may be possible for $N = 14$, if the conventional solution is greater than for $N = 9$. Looking at the increase from $N = 10$ to 12 indicates just such a possibility. However, the number of elements in the eigenvalue matrix is increasing rapidly, bringing up the cost of a solution. It would be better just to compare meshes which model the same points of interest.

For the exponential beam, inertias ranged from I_0 to $2.72I_0$, making it stiffer than its uniform cousin with inertia I_0 . According, the exponential beam buckled at a higher load. The buckling wavelength could be greater or less than the uniform beam solution ($\lambda = 1.0$) depending upon the mesh used. This points out the advantage of using the optimization technique for finding the buckling load. When a mesh was used which modeled the maximum inertia, a buckling wavelength was obtained which was higher than for the less stiff uniform beam.

Discontinuous Inertia

A beam with increased inertia about its center provides greater resistance to buckling. To investigate variations in inertia, continuously changing beams were examined. But the change in cross-section is usually abrupt, mostly due to

welding or riveting material at strategic locations along the column. The abrupt change leads to an investigation of discontinuous inertias.

Figure 20 illustrates one type of discontinuous beam.

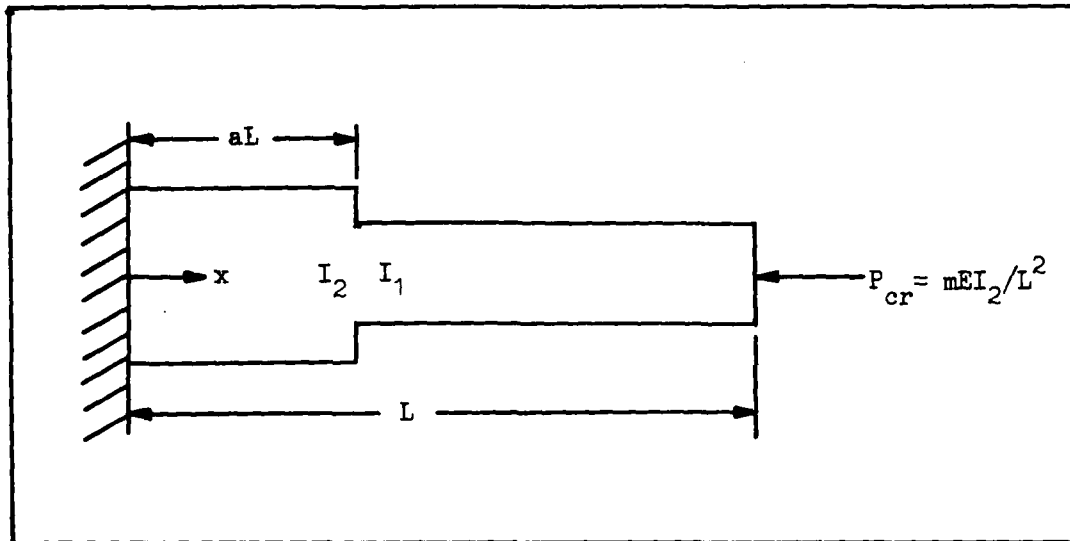


Fig 20. Typical Discontinuous Beam

The beam is clamped at one end and is free at the other. It is discontinuous in inertia at $x = aL$. The buckling load is defined in terms of the modulus E , the total beam length L , and the inertia I_2 . For simplicity, I_2 is defined as one. The inertia I_1 will be expressed as the ratio of I_1/I_2 with $I_2 = 1.0$. The non-dimensional coefficient m is well tabulated in literature (7,8,22,24). Because this type of discontinuous beam has known solutions widely available, it will be the model for my discontinuous inertia.

As was done with the continuously varying beams, the inertia must be calculated and provided for each node. This is not too difficult, there being only two values, I_1 and I_2 , in the example considered. Past experience has shown that

significant positions along the beam should be modeled with a node. These have included maximum inertia and maximum displacement. With this in mind, a node will be positioned at $x = aL$, the discontinuity of the beam. Positioning the node at that point forces certain mesh sizes on the modeling. For the beams of interest, a is a multiple of 0.1. Node numbers of 9, 14, and 19 are useful in modeling a discontinuity at this position. The effect of a node not at the discontinuity will also be examined.

If a node is located at a discontinuity, what value of inertia will be assigned to it? Should the inertia to its left (I_L) or to its right (I_R) be used? Possibly a simple average or a weighted average should be used.

Girijavallabhan (14) suggests an effective inertia for a discontinuity at node i

$$I_{\text{eff}} = \frac{6}{\frac{1}{I_L} \left(\frac{1}{2} + \frac{W_{i-1}}{W_i} \right) + \frac{1}{I_R} \left(\frac{1}{2} + \frac{W_{i+1}}{W_i} \right)} \quad (5-5)$$

for the beam of Figure 20. This solution makes use of an assumed mode shape which is not available in the approach of this thesis. An adequate value for I could be found by assuming that the displacements are the same as for the uniform beam. This inertia could be used to calculate a better eigenvector which in turn would generate a better effective inertia. The cycle would continue until some type of convergence is obtained. The final value for I would be used at the discontinuity.

A simpler solution is provided by O'Rourke (24). The

effective moment of inertia at a step change is given by

$$I_{\text{eff}} = \frac{2I_R I_L}{(I_R + I_L)} \quad (5-6)$$

O'Rourke states that this value of the inertia represents a value between the inertia for a pinned-pinned beam using Rayleigh's method with a step change and the inertia for a clamped beam. The real value of Eq (5-6) was not apparent in his paper. However, Ghali and Neville (7) derive this expression, which is repeated in Appendix C. In doing so, continuity in slope and moment is maintained, two very important properties. This expression maintains the necessary properties which is why Eq (5-6) is used in this thesis.

Specific Examples

As a check on the ability to predict the correct eigenvalue (buckling load), many beams of the type shown in Figure 20 were tested. The parameter "a" was varied from 0.1 to 0.9 with a similar range in I_1/I_2 . In all cases, using the inertia of Eq (5-6) at the discontinuity, the eigenvalue equation generated the known solution for a specific buckling wavelength. As an example, the following values were chosen for the beam shown in Figure 21:

$$\begin{aligned} a &= .7L \\ I_1/I_2 &= .3 \end{aligned}$$

The exact solution, as shown in Figure 21, is $P_{\text{cr}} = 2.221016EI_2/L^2$. The inertia calculated to represent the discontinuity is .4615 using Eq (5-6). For this clamped-free beam, a range of $.78 < \lambda < \infty$ provides accuracy better than the conventional

solution. The optimal wavelength is 1.10.

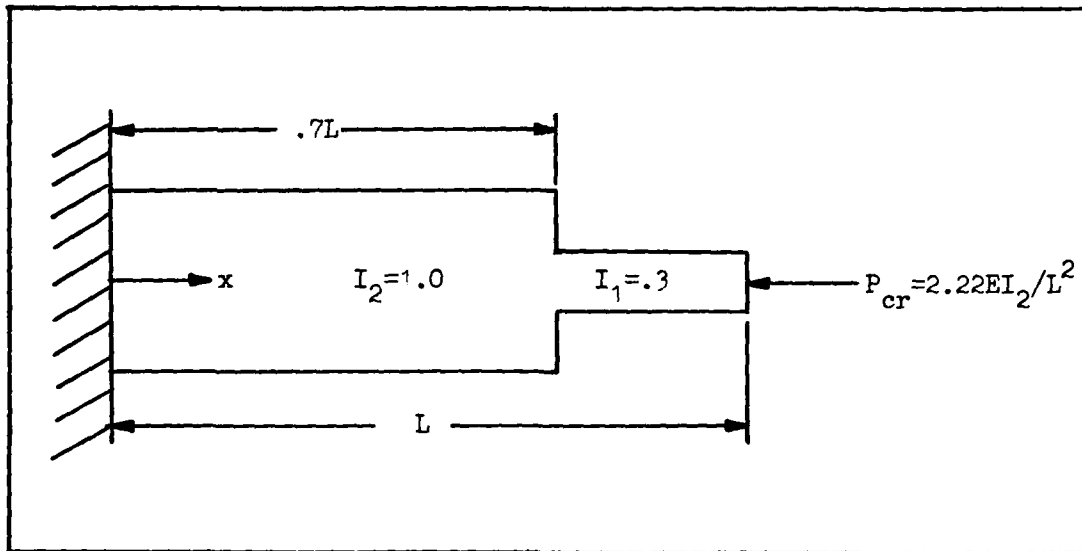


Fig 21. Discontinuous Beam of the First Example

A second example looks more closely at the effect of the number of nodes. Choosing the values of $a = .4$ and $I_1/I_2 = .4$ gives an exact solution of $M = 1.66931$. A P_{cr} vs λ curve for $N = 9$ is generated with an accuracy range of $.99 < \lambda < \infty$ and an optimal solution at $\lambda = 1.4$. A second curve, using $N = 19$ is superimposed in Figure 27. The two curve intersection occurs at $\lambda = 1.4$ as expected.

Two more curves are generated, one for $N = 8$ and another for $N = 10$. These nodal arrangements do not position a node at the discontinuity. Therefore, a node sees only an inertia of 1.0 or 0.4, depending upon its location. For the eight internal node beam, $\lambda = .78$ produces the known solution. For 10 nodes, though, the known solution is never reached. This buckling load curve appears in Figure 28. The conventional solution, which is the limit, is greater than the known solution. This could be due to the size of the inertia gradient

across the discontinuity. Assuming a linear gradient across the discontinuity results in effective inertias of .64 and .76 for the 8 and 10 node meshes respectively. The effective inertia from Eq (5-6) is approximately .57. While this is the value which maintains continuity, there may be an upper limit to the effective inertia below which the correct buckling load is returned for some value of the wavelength. In this case, the 10 node mesh models a beam that is too stiff.

As a check on where the upper limit on effective inertia lies, several values for the inertia at the discontinuity were substituted. The indicator that an effective inertia is too high is a conventional finite difference solution that is greater than the known solution. The beam is then too stiff.

An average of I_L and I_R , giving the effective inertia as .7, was tested. For all values of the buckling wavelength the known solution was not produced. Therefore, the 10 node inertia of .76, being higher than .7, would be expected to be ineffective.

A weighted average was also used to produce an effective inertia. This procedure sums the inertia of each segment - weighted by the percentage of the beam it represents - and divides by the sum of the inertias. The resulting inertia of .457 is below the value returned by Eq (5-6), .5714. The weighted average produced a correct solution at $\lambda = .44$. While this method produced a larger range of wavelengths for which the trigonometric solution was better than the conventional solution than for the inertia of Eq (5-6), the real

results were not as good. The conventional solution is worse for a weighted inertia because continuity is not maintained. So while you may have a larger range of wavelength at which the solution is better than conventionally, the conventional solution itself is not very good. A better test is how large a bandwidth on λ will give an accuracy within $\pm 1\%$ of the known buckling load. For a weighted inertia, this bandwidth extends from wavelengths equal to .43 to .48, a fairly small bandwidth. The inertia obtained using continuity gives a bandwidth from 1.26 to 1.61, five times larger. In fact, an inertia from Eq (5-6) gave a larger range of bandwidth accuracy than for any other inertia. In addition, there is an upper limit on the effective inertia above which the correct solution is unobtainable. This point should be kept in mind when modeling without a node at a discontinuity.

In addition, comparing curves for $N = 8$ and $N = 9$ yields an intersection for a buckling load of $1.75EI_2/L^2$, far above the known solution of 1.669; in Figure 29. This demonstrates the potentially poor results of trying to optimize the wavelength with meshes which do not model the same points.

A study should be made of what is the best effective inertia and compare it to that derived by Eq (5-6). For the purposes of this thesis, Eq (5-6) has been shown effective for all discontinuity combinations tested.

A final example of a more complex discontinuous beam is shown in figure 22. A pinned-pinned beam with two discontinuities is examined. The effective inertias at $x = .2L$ and

$x = .8L$ are determined by Eq (5-6). Using nine internal nodes, so chosen to place a node at each discontinuity, provides the expected solution at $\lambda = .64$. A second nodal arrangement, $N = 19$, is used to intersect with the curve produced by $N = 9$.

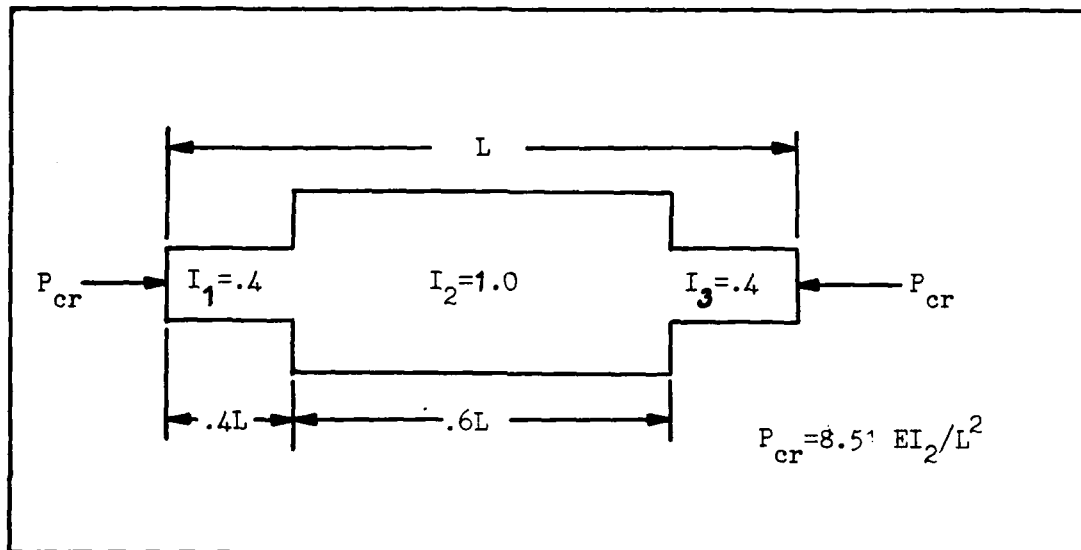


Fig 22. Third Example of a Discontinuous Beam

The intersection occurs for $\lambda = .64$, $P_{cr} = 8.51$, matching the known solution. The results are shown in Figure 30.

Summary

A beam with a discontinuous or varying moment of inertia can be analyzed using the approach of the thesis. In all such beams, an attempt should be made to place a node at the maximum moment of inertia and also at any discontinuities. For a continuous variation in inertia, the uniform beam results can provide an idea of a good choice of λ , generally larger than the uniform solution. The discontinuous beams can also use this principle.

An accurate method of determining the correct value for

the buckling load is to plot P_{cr} vs λ for two sets of nodes. The intersection of these two curves is the desired solution. The two sets of nodes should be somewhat similar. Also, the effective inertia at a discontinuity is evaluated using Eq (5-6).

With these principles, the known solution was derived for every example tested.

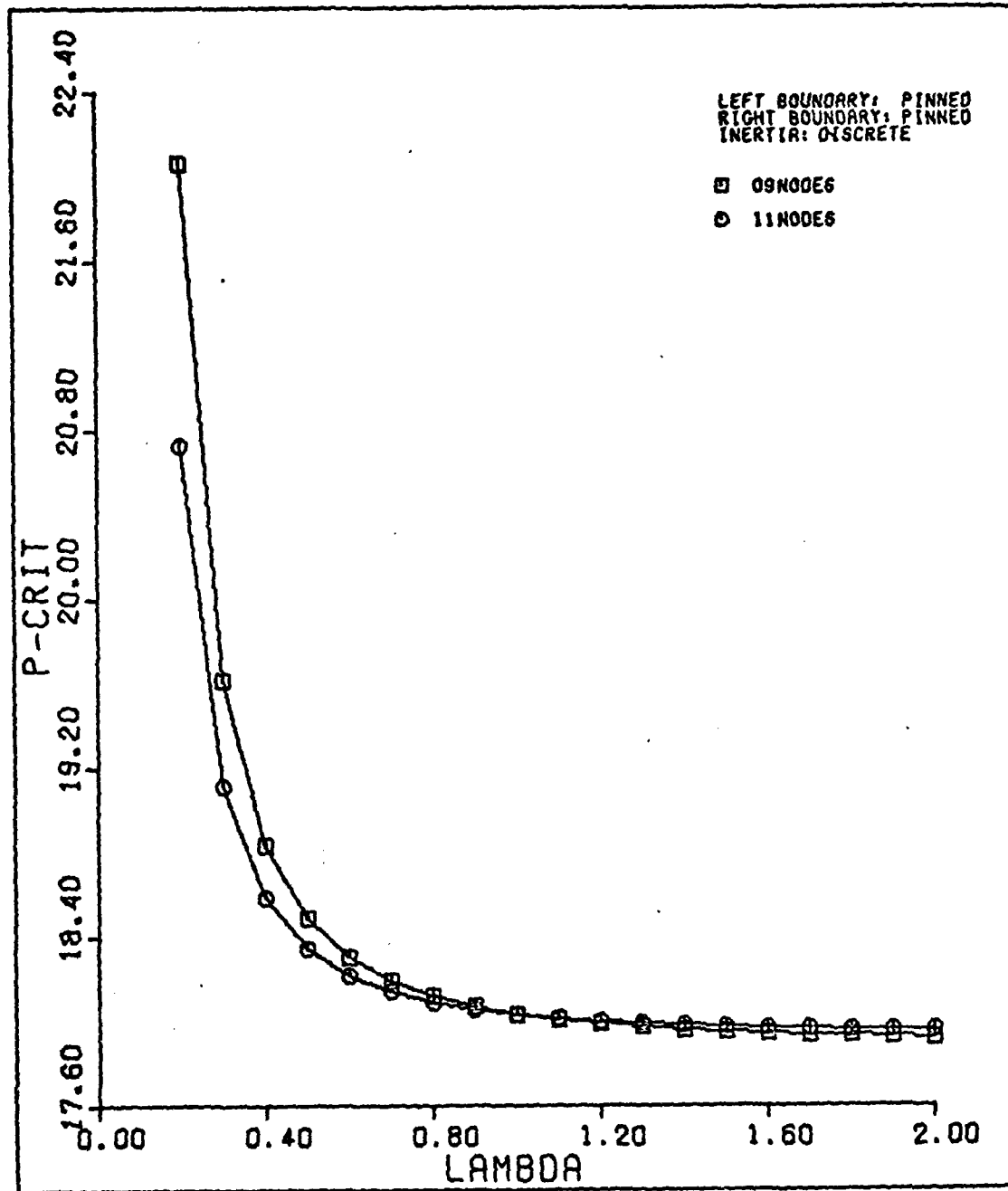


Fig 23. Buckling load curves for a beam with sinusoidal inertia. $N = 9, 11$.
 $P_{cr} = 18.03 EI_0 / L^2$, $\lambda = 1.018$.

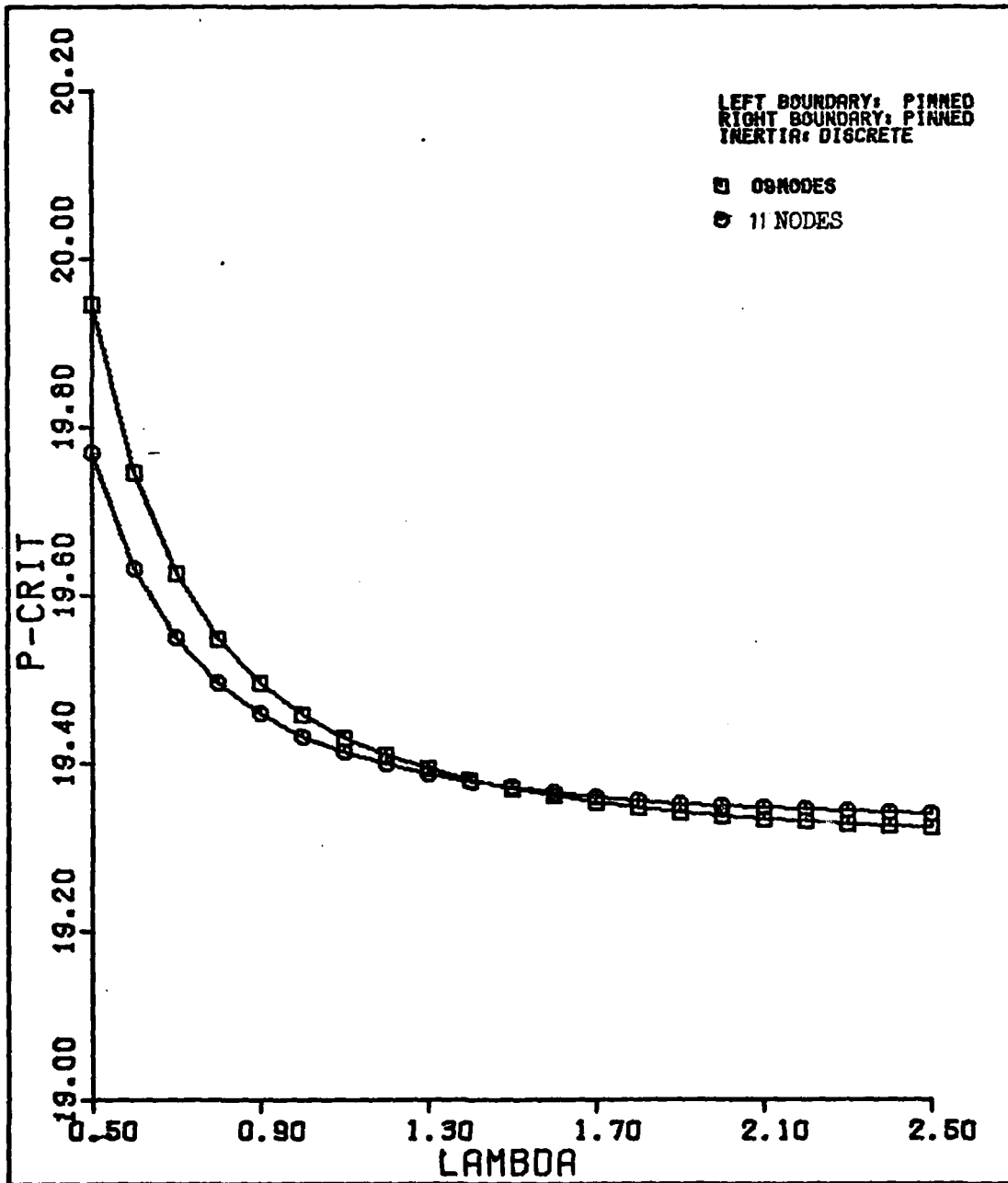


Fig 24. Buckling load curves for a beam with exponential inertia. N = 9,11.

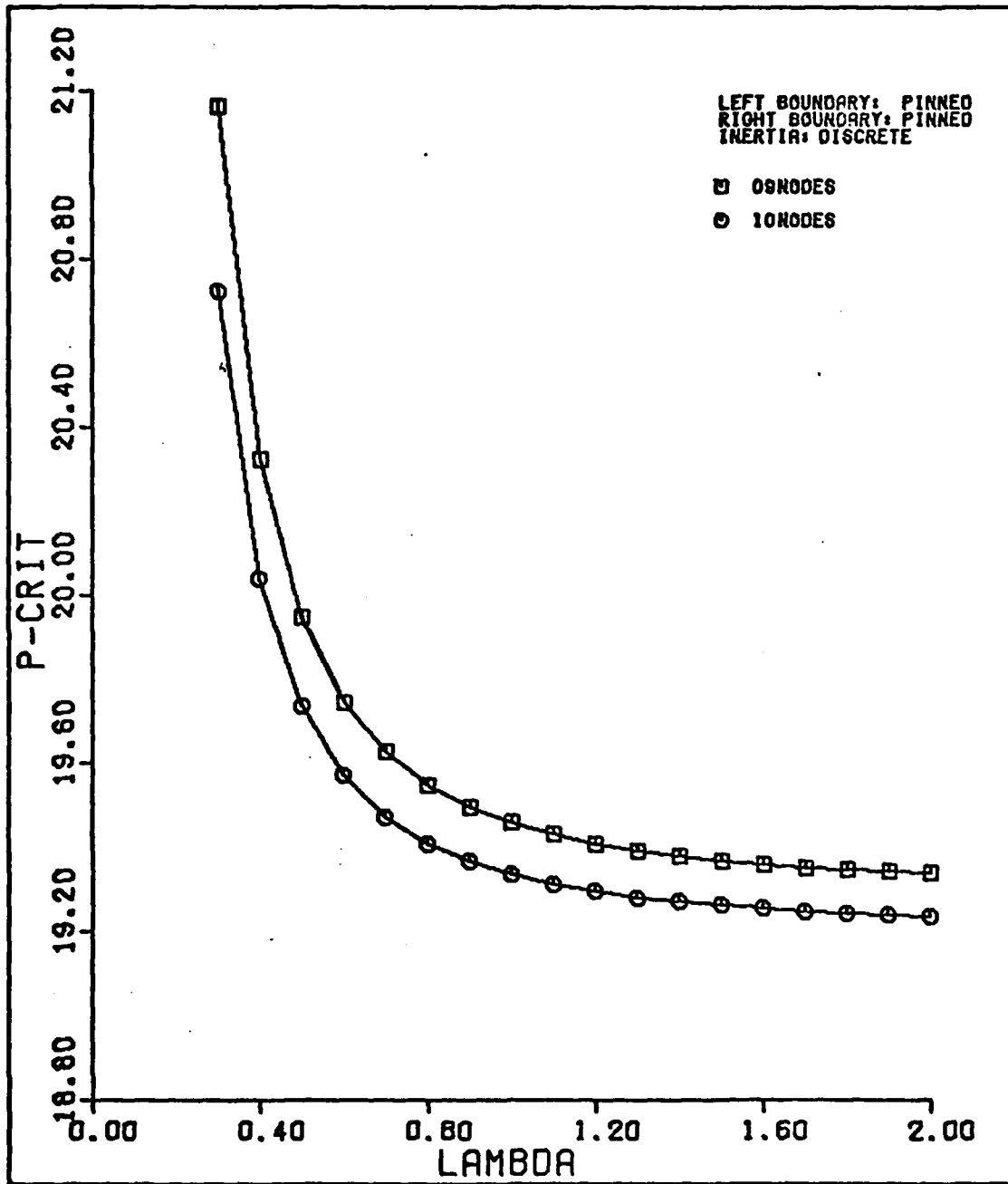


Fig 25. Buckling load curves for a beam with exponential inertia. N = 9,10.

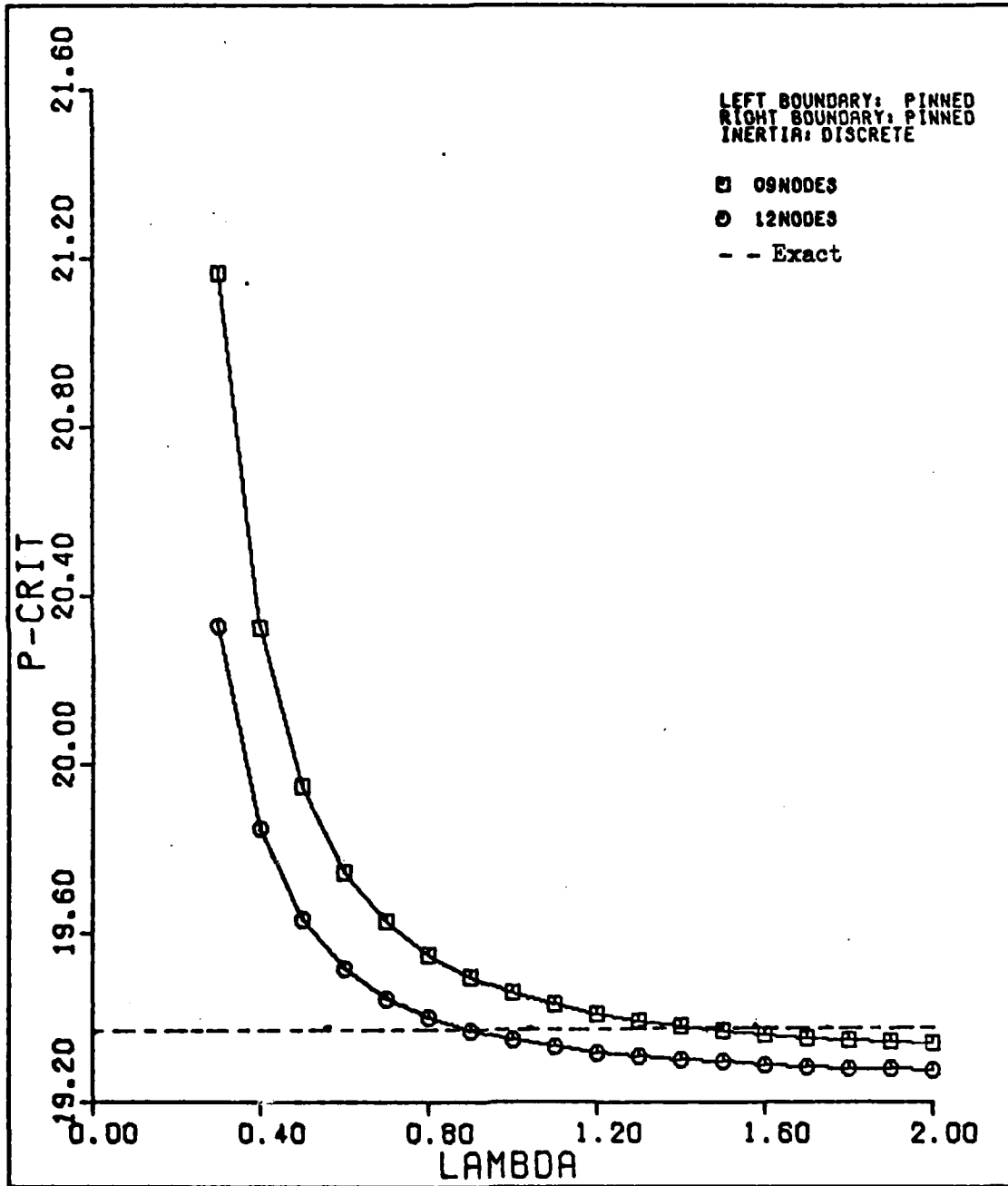


Fig 26. Buckling load curves for a beam with exponential inertia. N = 9,12.

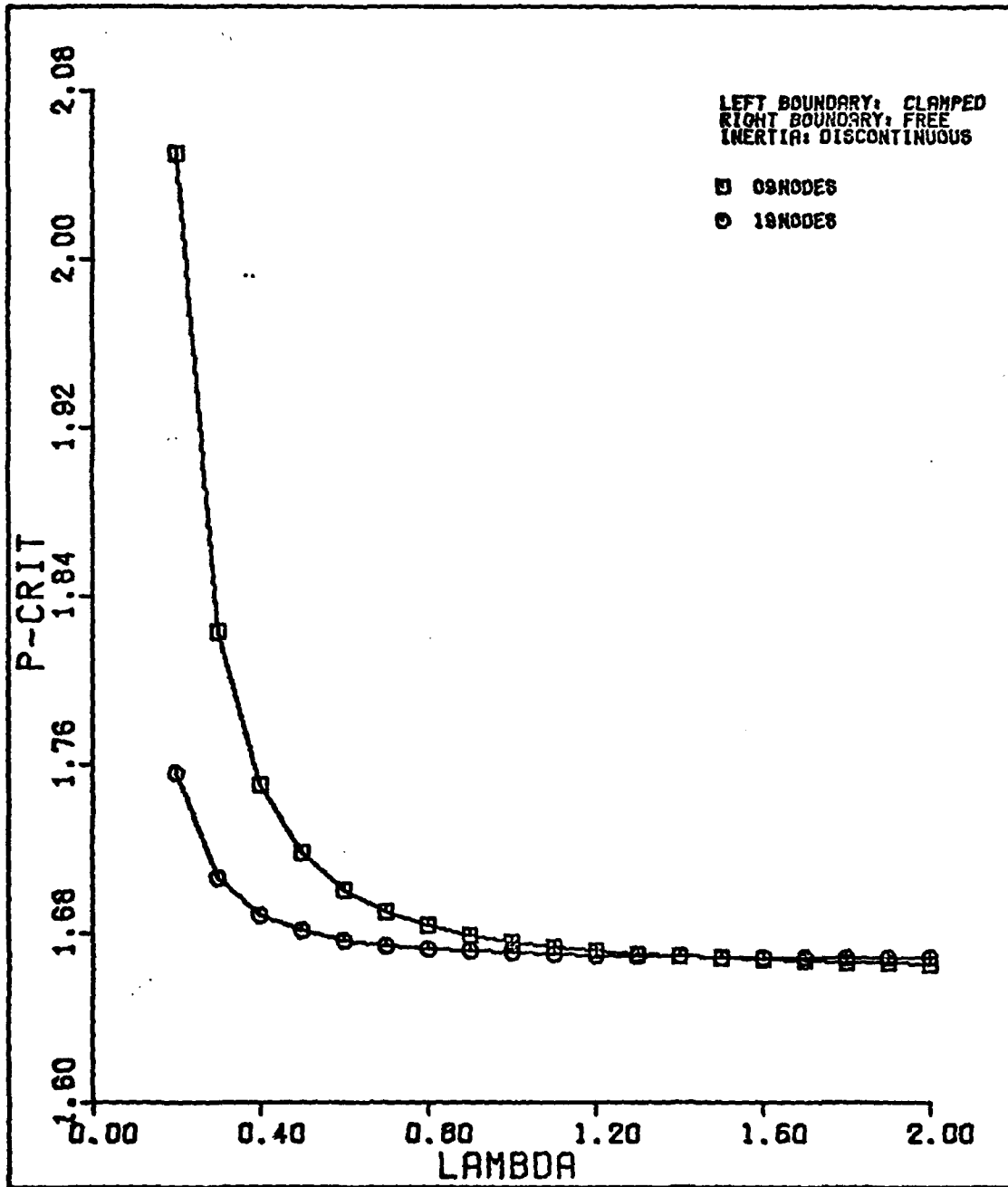


Fig 27. Buckling load curves for a discontinuous beam, $I_1/I_2 = .4$, $a/L = .4$. $N = 9, 19$
 $P_{cr} = 1.669 EI_2/L^2$, $\lambda = 1.4$.

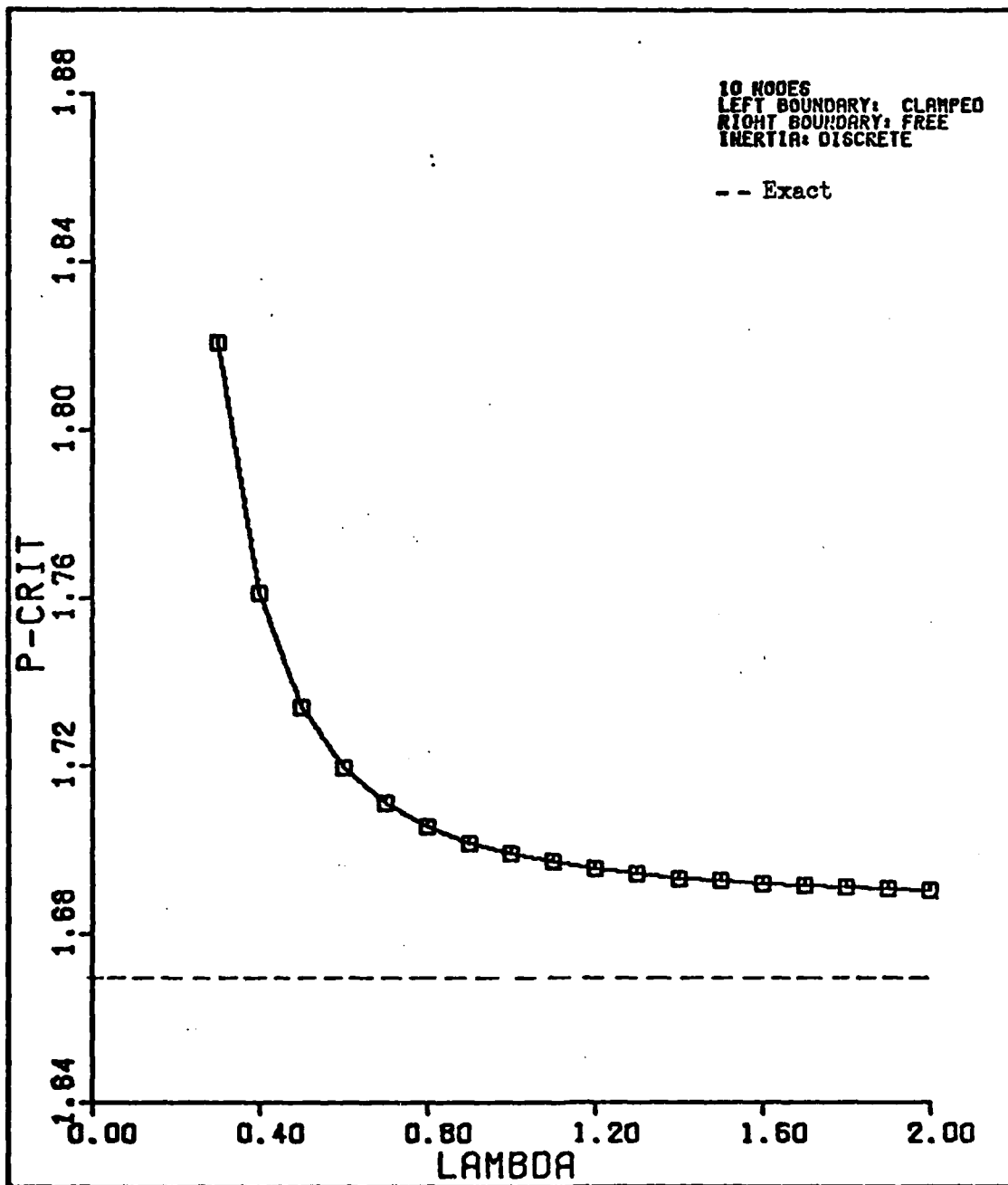


Fig 28. Buckling load curve for a discontinuous beam,
 $I_1/I_2 = .4$, $a/L = .4$. $N = 8,9$.
 $P_{cr} = 1.669 EI_2/L^2$, $\lambda = 1.4$

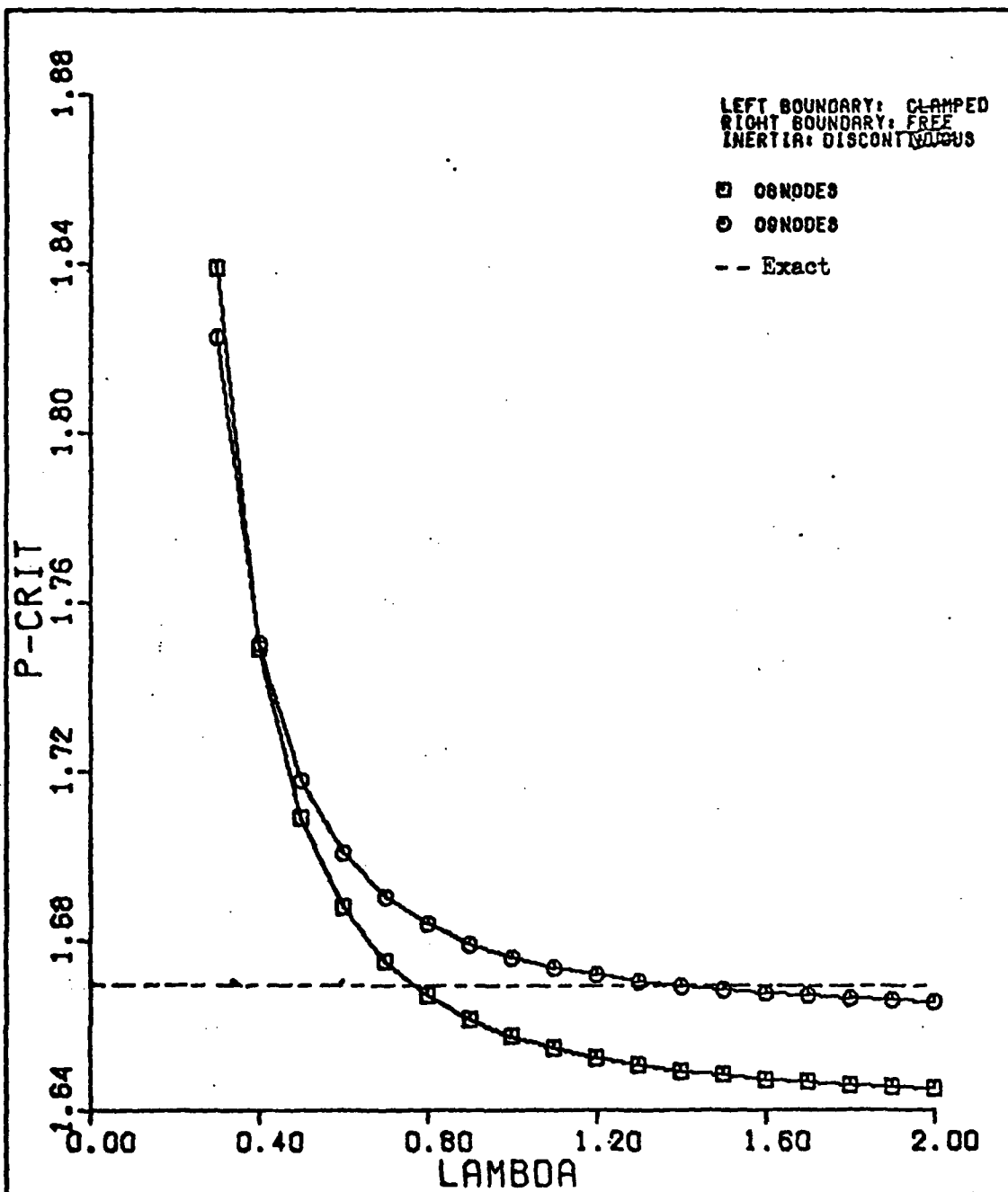


Fig 29. Buckling load curves for a discontinuous,
 $I_1/I_2 = .4$, $a/L = .4$. $N = 8,9$.
 $P_{cr} = 1.669 EI_2/L^2$, $\lambda = 1.4$

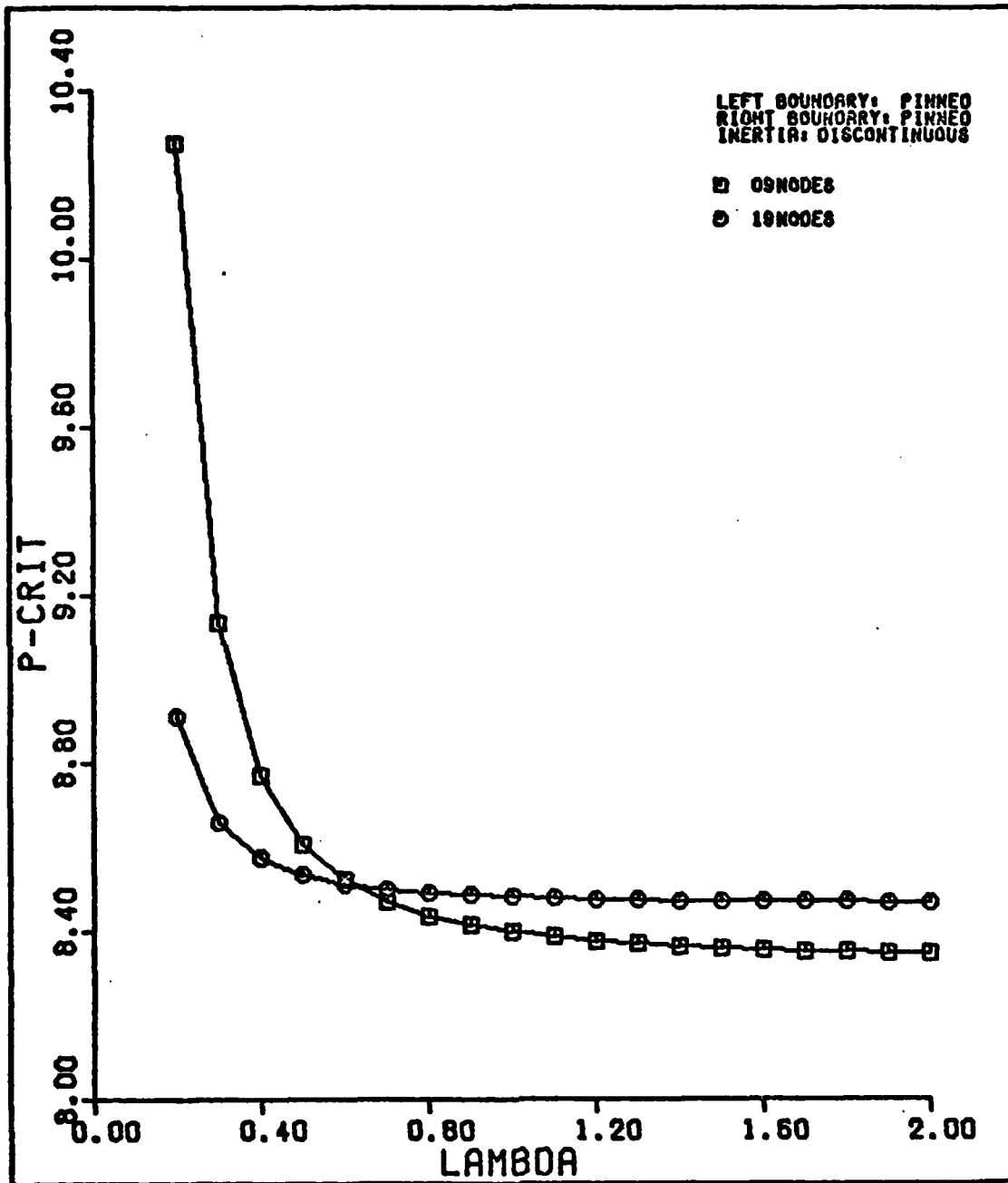


Fig 30. Buckling load curves for a discontinuous beam,
 $I_1 = I_3 = .4$, $I_2 = 1.$, $a_1 = .2L$, $a_2 = .6L$
 $N = 9,19$. $P_{cr} = 8.51$, $\lambda = .64$

VI. Variable Mesh

Introduction

In the previous section, beams with various inertias were examined. Often, the beam had a geometric discontinuity in its inertia. This discontinuity was modeled with a node at the location of the step change to produce the best results. Increasing the number of nodes also improved the solution accuracy, if the discontinuity is modeled. Previous examples showed the increase in accuracy between nine and nineteen nodes, both of which placed a node at a discontinuity. The change to 19 nodes decreased the mesh size by a factor of two, increasing the solution accuracy.

To obtain increased accuracy up until now, the number of nodes had to be increased. Doing this increases the time and cost to the user. An alternative approach to increasing the number of nodes is to respace the available nodes. For the discontinuous beams, a nine node solution may give better accuracy if the available nodes are respaced. With several nodes at and around the discontinuity, a better range of critical buckling loads may be obtained than is possible with a uniform mesh of the same number of nodes. Figure 31 shows the difference in node spacing for a discontinuous beam with nine nodes for uniform and variable meshes.

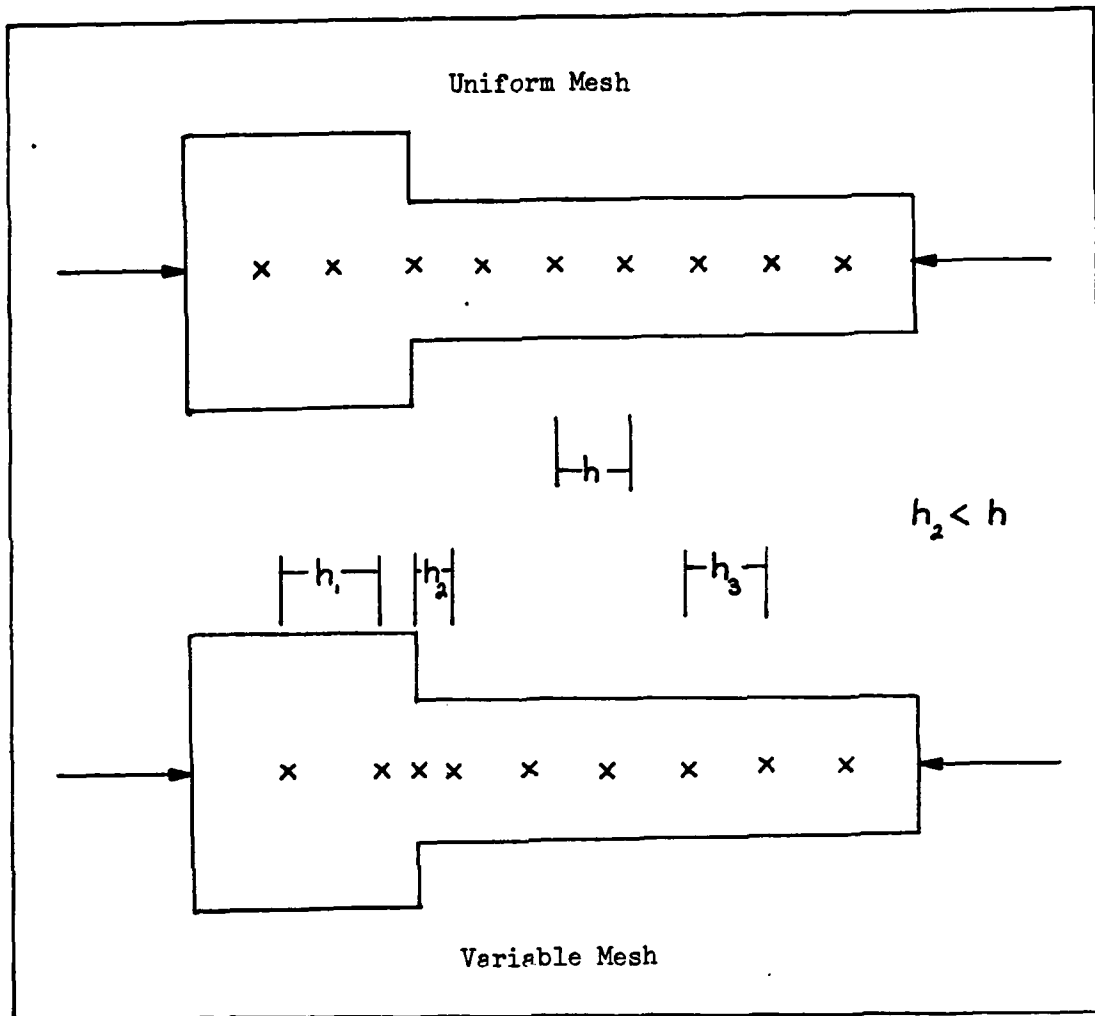


Fig 31. Comparison of Variable
Uniform and Variable Meshes

The variable mesh has taken the nine nodes with uniform spacing and redistributed several of them about the discontinuity. The remaining nodes are spaced according to the sizes of the remaining beam sections. Placing more nodes nearer the discontinuity than is available from a uniform mesh hopefully gives the same effect as increasing the total nodes used. For example, a nine node beam has an $h = .1$ mesh size. If two nodes are moved closer to the discontinuity for

a mesh spacing of $h_2 = .05$ (Figure 31), the mesh size near the change is the same as for $N = 19$. The question that must be answered is how the remaining nodes can be distributed for a more accurate solution to result. If this is possible, better accuracy can be obtained by clustering more nodes about discontinuities, points of maximum/minimum inertia, and other significant locations. Section VI examines just this question.

Technique

Section III of this thesis showed the numerical integration technique used to solve the virtual work expression with a uniform mesh. With a variable mesh, the numerical integration technique must be expanded to accommodate changes in mesh size throughout the beam. Figure 32 shows this scheme for a beam with three different mesh sizes. This figure is the analog to Figure 5 which works for uniform mesh. Nodes i and j correspond to the nodes at which mesh size changes. The three mesh sizes are h_1, h_2, h_3 . With the change in mesh size, Eq (3-33) must be reintegrated. Applying the trapezoidal rule, the equation

$$\int_0^L f dx = P \int_0^L g dx \quad (3-33)$$

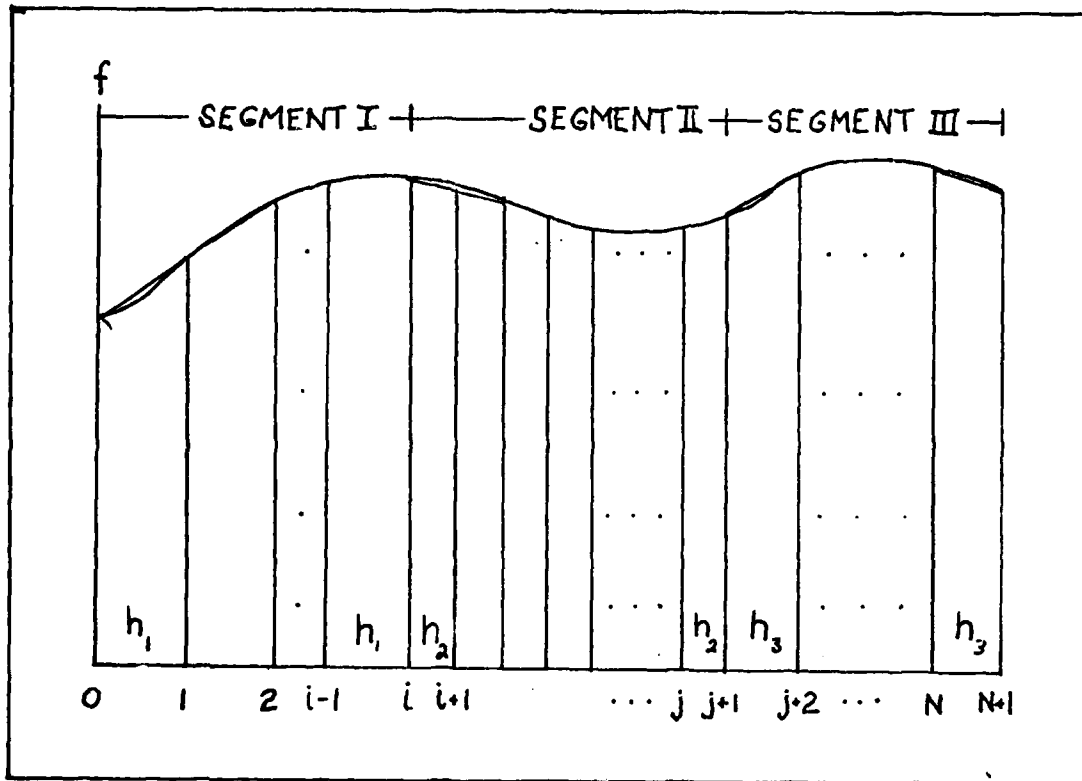


Fig 32. Numerical Integration of $f dx$ for a Variable Mesh

becomes

$$\left\{ \begin{array}{l} \frac{1}{2}h_1 f_0 + \sum_{a=1}^{i-2} h_1 f_a + \frac{1}{2}h_1 f_{i-1} \\ + \frac{1}{2}h_2 f_{i-1} + \sum_{b=i}^j h_2 f_b + \frac{1}{2}h_2 f_{j+1} \\ + \frac{1}{2}h_3 f_{j+1} + \sum_{c=j+2}^N h_3 f_c + \frac{1}{2}h_3 f_{N+1} \end{array} \right\} = \left\{ \begin{array}{l} h_1 \sum_{a=0}^{i-2} g_{a+\frac{1}{2}} \\ + h_2 \sum_{b=1-1}^j g_{b+\frac{1}{2}} \\ + h_3 \sum_{c=j+1}^N g_{c+\frac{1}{2}} \end{array} \right\} \quad (6-1)$$

Eq (6-1) is the analog to Eq (3-34). If the mesh spacing h_i ($i = 1, 2, 3$) is constant, Eq (6-1) reduces to Eq (3-34). To numerically integrate each separate variable mesh problem could take a lot of work, except for a simplification evident

in Eq (6-1). Each bracketed ($\{\}$) set of terms has the same construction as the others, except for the different mesh size and end points. It becomes fairly simple to program this repetitious pattern. The end result is the construction of the eigenvalue matrices for each segment of uniform mesh size. These eigenvalue matrices correspond to the ones described by equation (3-45). However, whereas the matrices generated by Eq (3-46) were global - describing the entire beam, the matrices built by a segment of constant mesh size h_i are 'local' - corresponding to only that segment. To produce the required global matrix equation, the local matrices must be added for each segment of constant mesh size. For the beam in Figure 32, there are three segments of constant mesh size. Therefore, three local eigenvalue matrices are produced corresponding to the bracketed terms in Eq (6-1). These matrices are added together, making sure the nodes overlap correctly, producing a global matrix equation of the same form as Eq (3-46). This process is similar to the construction of a global stiffness matrix in finite elements, in which segments of a beam add their local stiffness matrices together to form a global matrix. The local matrices developed here depend upon stiffness, inertia, and the displacements at each node, as well as the mesh size.

Because various mesh sizes are used in the beam, difficulties arise. Eq (6-1) demonstrates the need to define f_{i-1} , the combination of derivatives at a node where the mesh changes.

Previously,

$$f_{i-1} = \frac{E_{i-1} I_{i-1}}{\tilde{h}^2} [W_i - 2W_{i-1} + W_{i-2}] [\delta W_i - 2\delta W_{i-1} + \delta W_{i-2}] \quad (6-2)$$

This expression used a full-station central difference which was derived using a constant mesh size. But Figure 32 shows that f_{i-1} has mesh sizes h_1 and h_2 on either side of node (i-1). The central difference expressions created for the second derivative in Section III are of no use at a node separating two different mesh sizes.

Using a technique similar to the one used in Section III, a finite difference expression for the second derivative is calculated in Appendix B. At a mesh discontinuity node, this expression is used instead of the second derivative shown in Eq (6-2). The first order derivatives do not have this problem because their reference points are between two nodes, where the mesh does not change size. With the appropriate nodal expressions used, the eigenvalue matrix is calculated in the same manner as in Eq (3-46).

The mesh discontinuities introduce one more unfavorable aspect to the problem. Previously, in Eq (3-34), the mesh size h was factored out of the eigenvalue equation because it was constant and appeared on both sides of the equation. With the variable mesh, the mesh size for each segment h_i must be retained in the problem. Of greater significance is the need to multiply each term of the A matrix of Eq (3-46) by $1/\tilde{h}_i^2$ where \tilde{h}_i is the equivalent mesh corresponding to each segment of the beam. For a constant mesh size, the equivalent mesh \tilde{h}

AD-A079 862

AIR FORCE INST OF TECH WRIGHT-PATTERSON AFB OH SCH00--ETC F/6 13/13
COLUMN BUCKLING OF ISOTROPIC AND COMPOSITE BEAMS USING A TRUNCA--ETC(U)
DEC 79 J L INSPRUCKER

UNCLASSIFIED

AFIT/6A/AA/804-2

NL

2 of 2
PAGE 2
/TOTAL



| | | | | | | | | | | | | | |
|--|--|--|--|--|--|--|--|--|--|--|--|--|--|
| | | | | | | | | | | | | | |
| | | | | | | | | | | | | | |
| | | | | | | | | | | | | | |
| | | | | | | | | | | | | | |

END
DATE
FORMED
2 - 80
001

could be factored outside the A and B matrices in Eq (4-1) and (4-2). Doing so permitted solving the eigenvalue matrix for k, Eq (4-3), then varying λ to obtain P_{cr} . Because h is not constant throughout the beam, neither is \tilde{h} . The equivalent mesh term is now brought within the matrices of Eq (3-46), and with it goes the ability to vary λ after the eigenvalue matrix problem is solved. The equivalent mesh sizes cannot be expressed as ratios of one another, in an effort to retain the variation in λ external to the matrix solution, because the ratios themselves depend upon λ . The mesh sizes h_i could be scaled this way, but that is of no significant use.

The use of a variable mesh requires that the wavelength parameter be specified before solving the eigenvalue equation. The eigenvalue returned is the buckling load and not k in Eq (4-3), which simplified solving problems with a uniform mesh. Because of this, a P_{cr} vs λ curve cannot be generated with only one solution of the matrix equation. The variable mesh approach requires constructing and solving the matrix equation each time a point on the buckling load curve is desired. Before, the buckling load curves in Sections IV and V required one matrix solution. Now, twenty solutions may be needed to produce the same curve. The increase in time and cost makes the variable mesh approach appear unusable right away. Only for a better range of accuracy than is available with an equal number of nodes in a uniform mesh can the technique hope to be effective.

Test Results

To answer the question just posed, whether variable meshes are more accurate than uniform meshes for an equal number of nodes, beams from Section V were reanalyzed. These beams have a varying moment of inertia, providing the best test of preferentially grouped nodes.

The first beam tested appears in Figure 33.

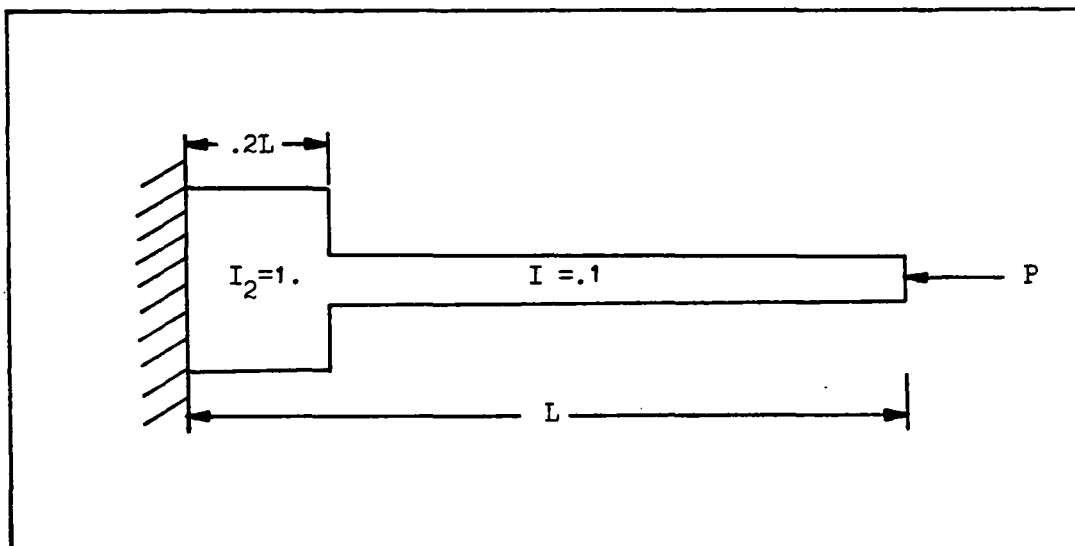


Fig 33. First Variable Mesh Example

The known exact solution is $P_{cr} = .366875 EI_2/L^2$, occurring at $\lambda = 1.61$ for nine or 19 nodes uniformly spaced. The number of nodes to be used for the variable mesh is nine. Nine nodes provides a convenient mesh size (.1L) and places a node at the discontinuity. Because the discontinuity at $x/L = .2$ is the region of significance, more nodes will be grouped around it. There will be two uses made with the variable mesh, one with three nodes near the discontinuity and one with five nodes. The meshes will be used to generate the buckling load curve P_{cr} vs λ (by multiple computer runs) which can be compared to

the curve for nine nodes uniformly generated.

The first variable mesh tested, (mesh A), consists of three nodes clustered more closely around the discontinuity than is available with the uniform mesh. The nodal arrangement is shown in Figure 34. The mesh size around the discontinuity, h_2 , was chosen as one-half the uniform mesh size of $.1L$. This corresponds to modeling the region near the discontinuity with a 19 node mesh, which would provide a mesh of $.05L$.

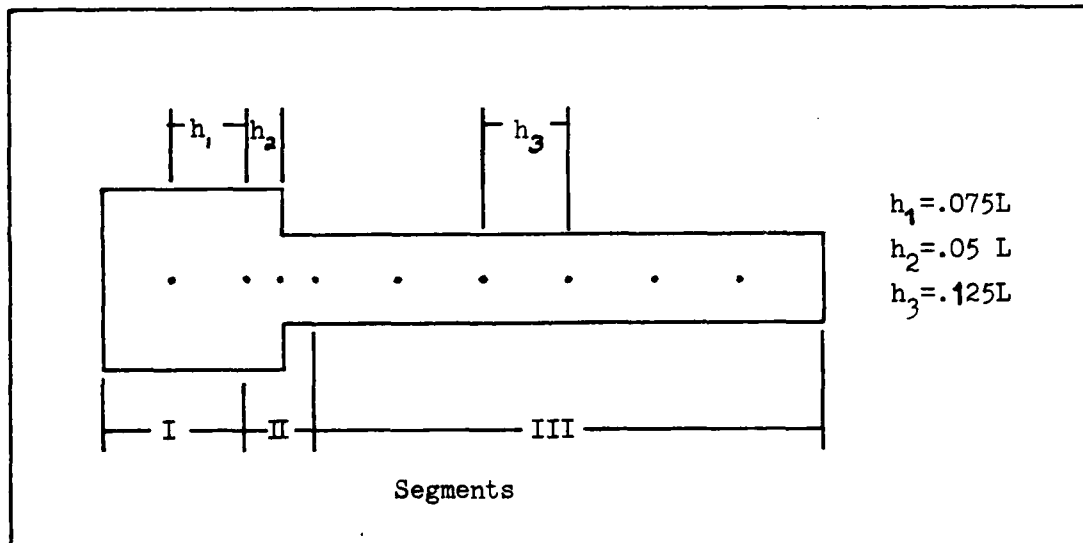


Fig 34. Discontinuous Beam With Variable Mesh A

The six remaining nodes (nine minus three) are distributed by the percentage of remaining beam. This results in mesh sizes of $h_1 = .075L$ and $h_3 = .125L$. With the first variable mesh in place, the buckling load was calculated for 20 values of the wavelength parameter (.1 to 2.0)

A second mesh (B) was built using five nodes about the discontinuity, also with mesh size $h_2 = .05L$. The remaining four nodes are distributed to create mesh sizes $h_1 = .10$ and

$h_3 = .14$, shown in Figure 35.

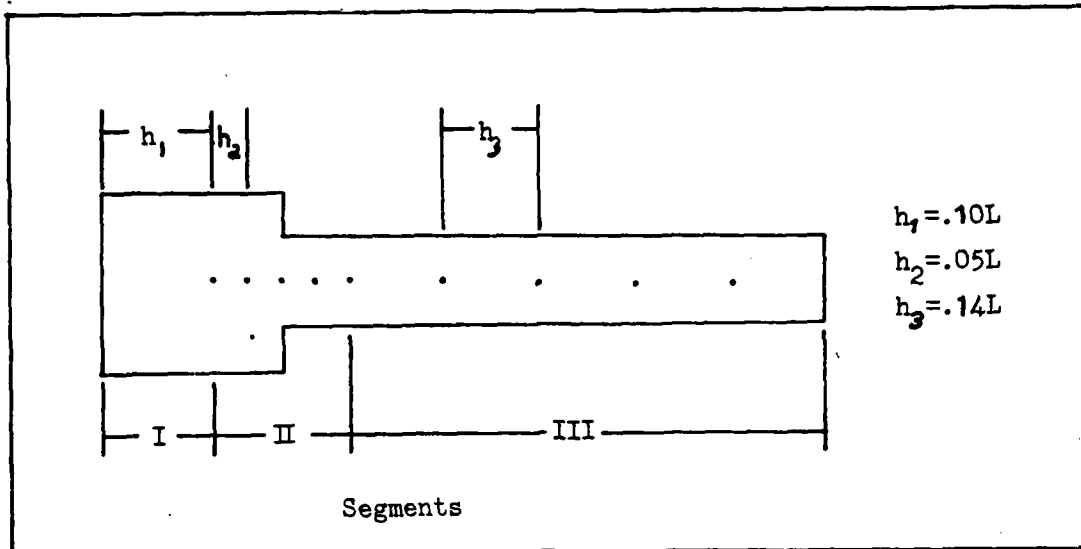


Fig 35. Discontinuous Beam With Variable Mesh B

A curve of buckling load vs λ is generated by multiple solutions of the eigenvalue equation.

The curves obtained for meshes A and B are displayed with the nine node uniform mesh curve in Figure 37. At $\lambda = 1.6$, the uniform mesh provides a solution of $P_{cr} = .36688EI_2/L^2$ which is in error by only .0014% of the known solution. The variable meshes A and B on the other hand have solutions of .36720 and .36753, respectively. The errors for the variable meshes are .089% and .179%, much larger than for the uniform mesh solution. In fact, figure 37 shows that for all $\lambda < 1.6$, the uniform solution is more accurate than either variable mesh solutions. Likewise, three nodes around the discontinuity are better than five. For the range $\lambda > 1.6$, there are small intervals in which each variable mesh solution is more accurate than the uniform solution. Not because of the better quality of the mesh, but because they fail to match

the uniform curve. Mesh A arrives at the exact solution at $\lambda = 1.73$ and mesh B at $\lambda = 1.78$. During the interval $1.7 < \lambda < 1.9$, the two meshes are more accurate. But this accuracy quickly disappears and soon the uniform solution is best again.

As the wavelength parameter grows very large, the uniform solution approaches the conventional solution. Unfortunately, the variable mesh solutions pass right through this uniform mesh limit, possibly reaching a limit which is worse than that attained with the conventional finite difference approach.

A final drawback is the failure of the variable mesh to accurately predict the known buckling load. If two good uniform meshes are used, the intersection of the buckling curves is the buckling load. This method was found highly useful in the last section. The intersection of meshes A and B occurs at $\lambda = 1.9$ producing a solution of $P_{cr} = .36656EI_2/L^2$, lower than the known solution.

For this beam, changing from a uniform to a variable mesh produced results inadequate to justify using a variable mesh.

The beam in Figure 33 was remodeled to see if shrinking the mesh size around the discontinuity had any effect. The first set of meshes used a mesh size in the segment enclosing the discontinuity of $h_2 = .05L$. A second set of meshes with $h_2 = .025L$ were constructed, with the same type of mesh structure used as before, i.e. first three and then five nodes around the discontinuity. The remaining nodes are then

distributed according to the length of the remaining beam segments. The meshes are similar to the first set, but are more tightly packed at the discontinuity and more loosely packed away from the inertia step change. For three nodes around the step, the mesh sizes are $h_1 = .0875L$, $h_2 = .025L$, and $h_3 = .12917L$. This is the A mesh. The B mesh, with 5 nodes about the discontinuity, has mesh sizes $h_1 = .075L$, $h_2 = .025L$, and $h_3 = .1875L$. Checking the buckling loads at $\lambda = 1.6$ (which is approximately the optimal wavelength for the uniform case of nine nodes) produces:

$$\text{Mesh A} \quad P_{cr} = .36712 \quad \text{Error} = .067\%$$

$$\text{Mesh B} \quad P_{cr} = .36775 \quad \text{Error} = .239\%$$

The buckling load curves are plotted in Figure 38.

Comparing these results with the A and B meshes from set one produces some interesting results. For three nodes about the discontinuity, the denser mesh of the second set is closer to the uniform solution for all λ . However, five nodes about the discontinuity favors the looser mesh of the first set. Possibly there is a size for the mesh outside of the discontinuity above which the solution deteriorates. For the three node sets, mesh set two had higher mesh size but better packing around the discontinuity. Therefore it may not have crossed the limit on mesh size away from the step change and would then produce better results. On the other hand, with the five node examples, mesh set two had better packing around the discontinuity but much poorer meshes in other parts of the beam than did the first case.

Using more and more of the available nodes to model the

discontinuity leaves fewer nodes to model the remaining beam. This is the reason for the poor performance of the variable mesh. The uniform mesh does a better job of modeling the outer beam segments while doing an adequate job of modeling the discontinuity. A point to remember is that the discontinuity needs a node at that position. Nodes on either side may create too high an inertia gradient, thereby preventing the buckling curve from passing through the critical buckling load.

Further examples of the variable mesh were examined. The beam in Figure 36 was examined using three and five nodes around the discontinuity, meshes A and B respectively.

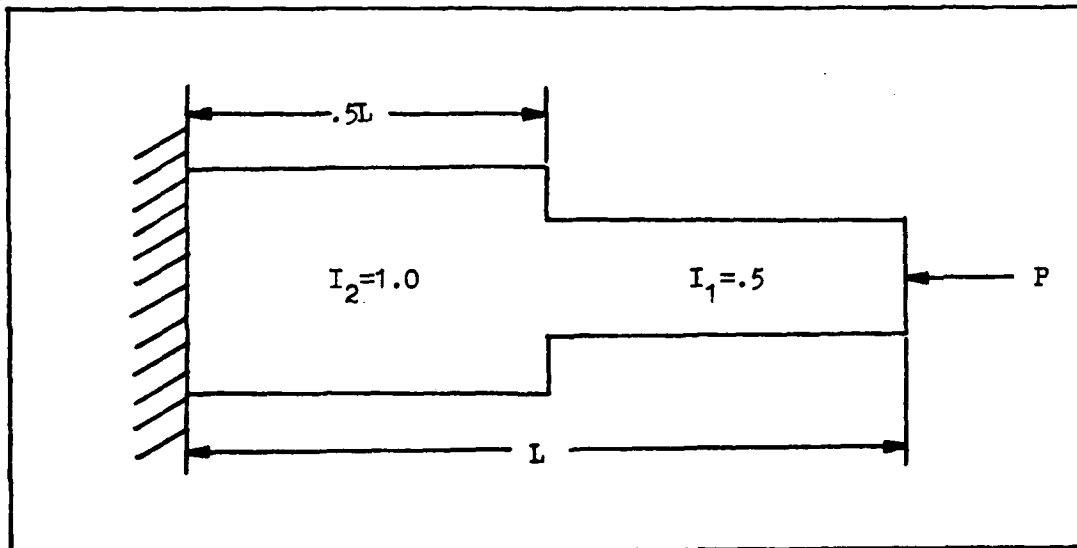


Fig 36. Discontinuous Beam $P_{cr} = 2.067EI_2/L^2$

Once more, the uniform nine node solution was superior for all values of λ except that small range where the variable mesh curves pass through the known solution. The curves for Figure 36 are shown in Figure 39. The mesh sizes used were $h_1 = .1125$, $h_2 = .05$, $h_3 = .1125$ (Mesh A) and $h_1 = .133$,

$h_2 = .05, h_3 = .1333$ (Mesh B).

Final checks were made using the beams with exponentially- and sinusoidally-varying inertia from the previous section. For each beam, three nodes were grouped about the center $X = .5L$. It is at the center that the inertia is maximum. Errors were checked for two values of λ : $\lambda = 1.0$ and 1.8 . The results are in Table 6-I. These spot checks reveal the same pattern as was previously shown. Namely, that a variable mesh produces poorer results than a uniform mesh with the same number of nodes. The buckling load curves for these two beams are available in Figure 40 and Figure 41.

TABLE II
Nine Internal Nodes

| | Sinusoid | | Exponential | |
|---------------|-----------------|-----------------|-----------------|-----------------|
| | $\lambda = 1.0$ | $\lambda = 1.8$ | $\lambda = 1.0$ | $\lambda = 1.8$ |
| Uniform Mesh | .017% | -.551% | .449% | -.122% |
| Variable Mesh | .257% | -.663% | .744% | -.141% |

Summary

For an equal number of nodes, a uniform mesh is generally much more accurate than a variable mesh. The only place where the variable mesh is more accurate is the small λ range where the buckling curve passes through the known solution.

The variable mesh requires the buckling wavelength parameter to be input before a buckling load can be returned. This is different from the uniform mesh which calculates a buckling curve based on only one eigenvalue matrix solution.

Therefore, plotting a variable mesh buckling curve requires as many matrix solutions as points on the curve, an extremely costly method. In addition, the intersection of two variable mesh buckling curves does not yield the correct buckling load, whereas two uniform mesh curves do. Since the aim is to find the buckling load of a beam, it is best to plot two uniform mesh curves and find their intersection. This costs as much as finding two points on one variable mesh curve. If all that is desired is a P_{cr} for a choice of λ , the uniform mesh will provide a much better solution in almost all cases. The exception occurs if λ is chosen near the optimal λ for the variable mesh. But the uniform mesh is very close to the same solution, so no real improvement in accuracy occurs. For any other λ , a uniform mesh can provide a large accuracy improvement. In fact, for very large λ , the variable mesh may be even poorer than a conventional finite difference solution.

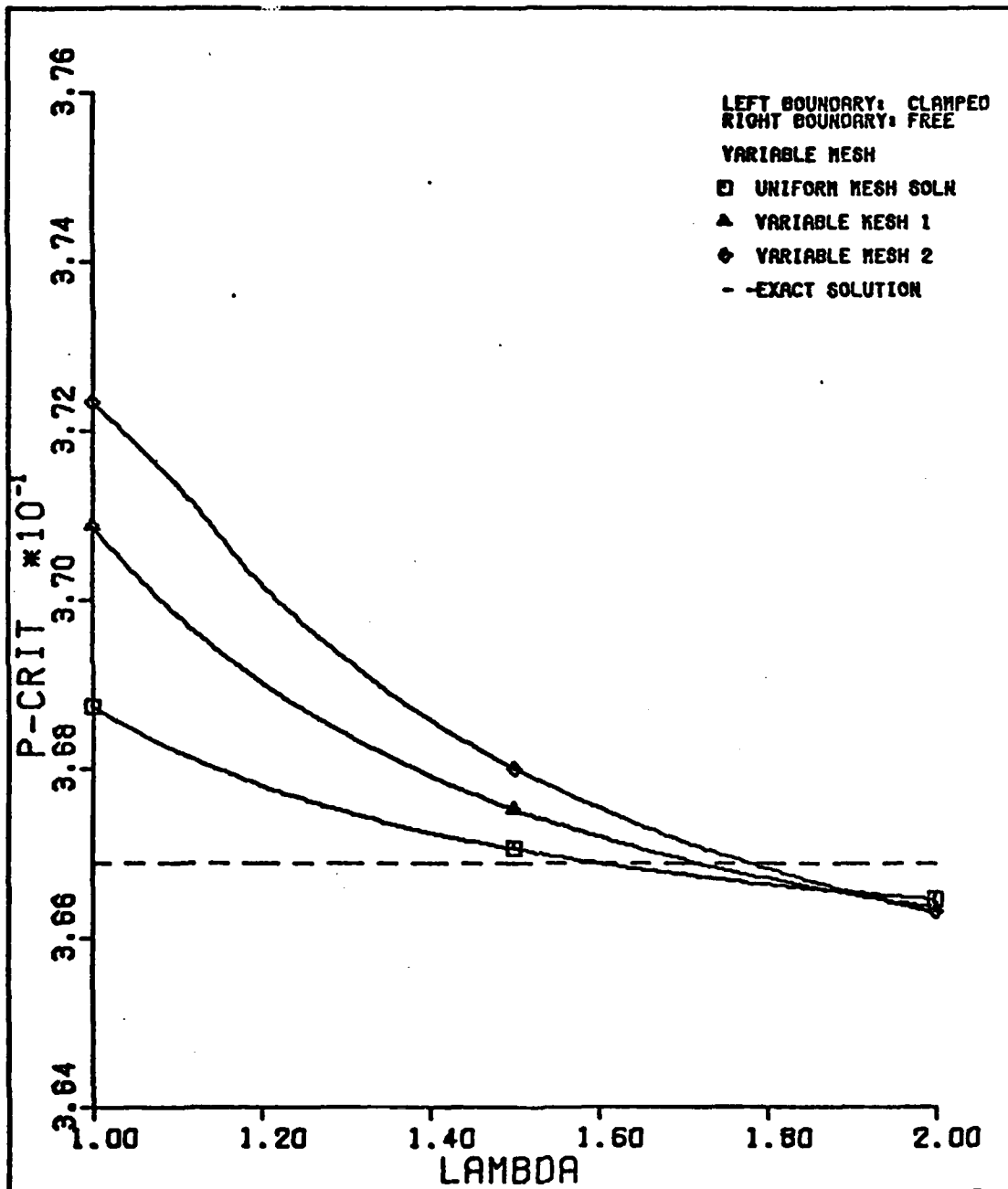


Fig 37. Uniform and variable mesh curves for a discontinuous beam, $I_1/I_2 = .1$, $a/L = .2$, $N = 9$. Variable mesh 1 clusters 3 nodes around the discontinuity, mesh 2 clusters 5. $h_2 = .05L$

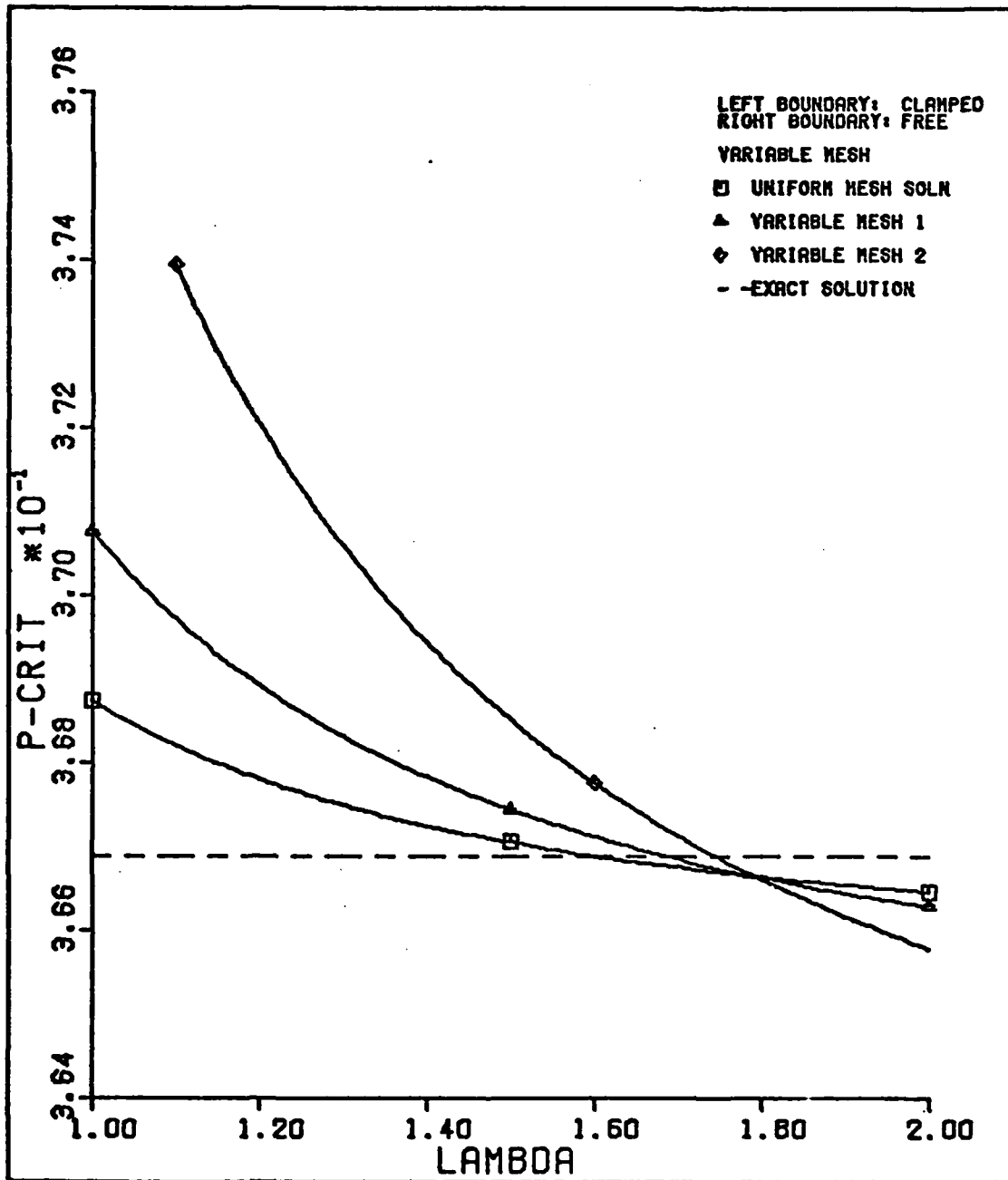


Fig 38. Uniform and variable mesh curves for a discontinuous beam, $I_1/I_2 = .1$, $a/L = .2$, $N = 9$. Variable mesh 1 clusters 3 nodes around the discontinuity, mesh 2 clusters 5. $h_2 = .025L$

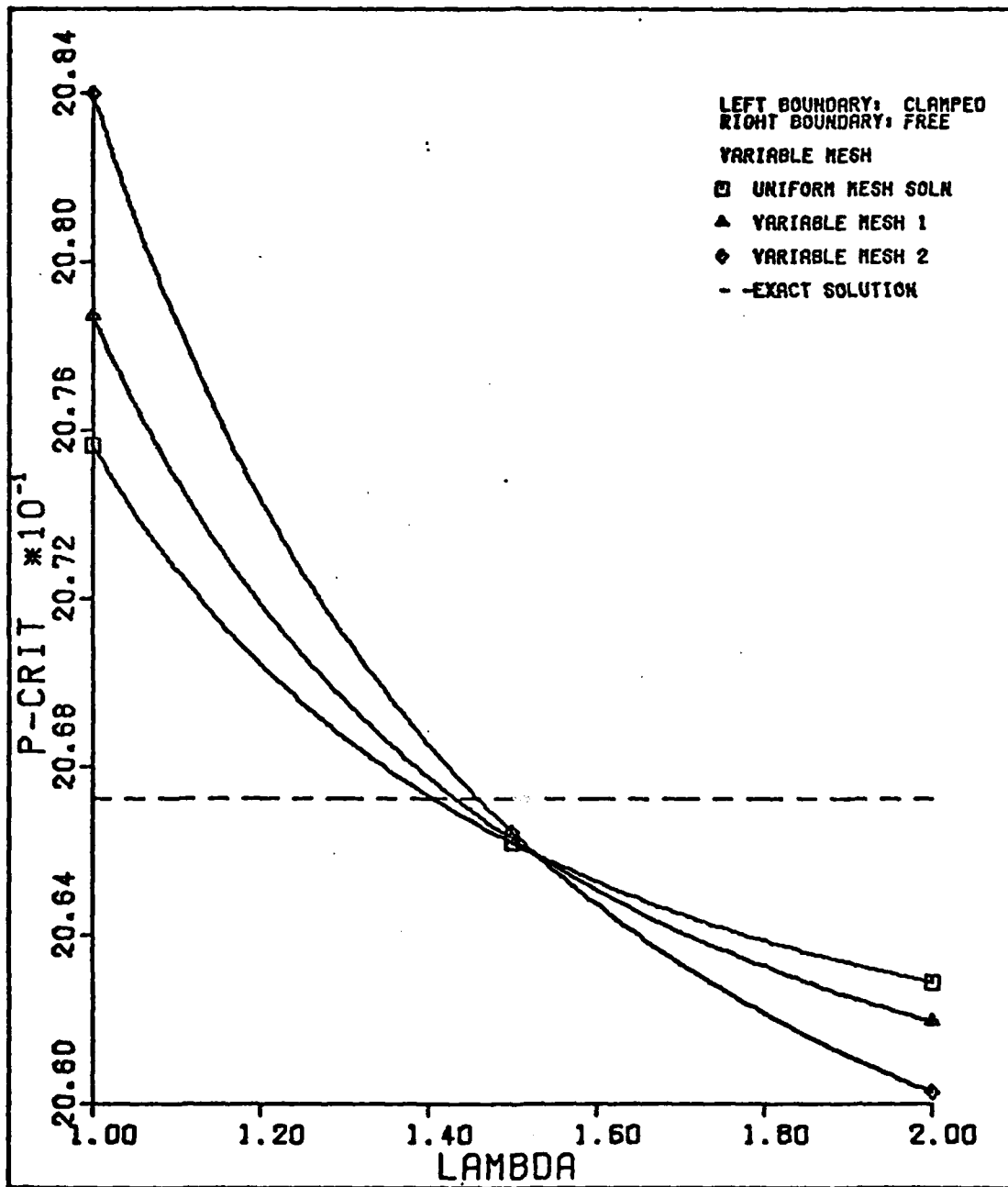


Fig 39. Uniform and variable mesh curves for a discontinuous beam, $I_1/I_2 = .5$, $a/L = .5$, $N = 9$. Variable mesh 1 clusters 3 nodes around the discontinuity, mesh 2 clusters 5. $h_2 = .05L$

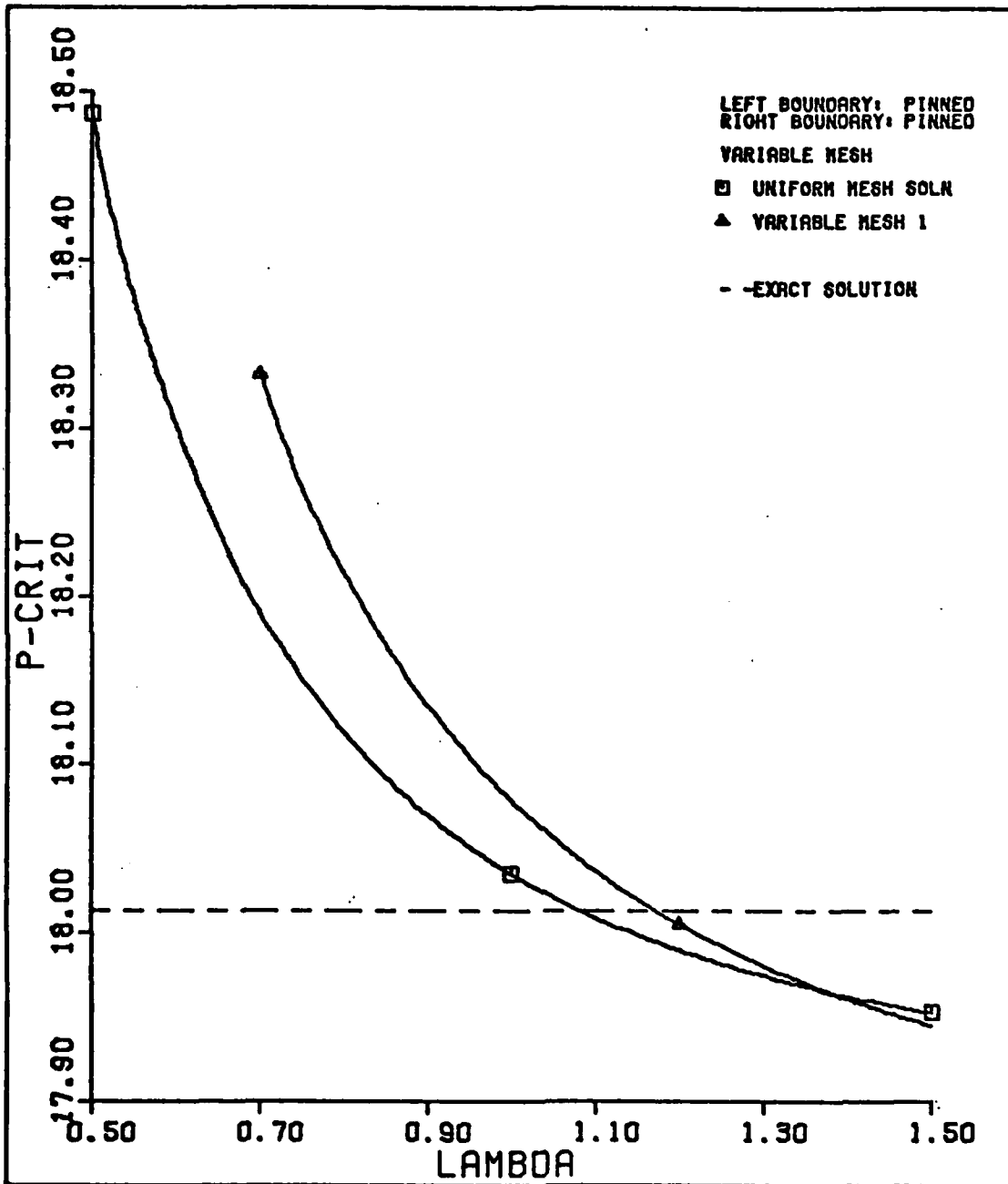


Fig 40. Uniform and variable mesh curves for a beam with sinusoidal variation of inertia. Variable mesh 1 clusters 3 nodes around maximum inertia. $h_2 = .05L$. $N = 9$.

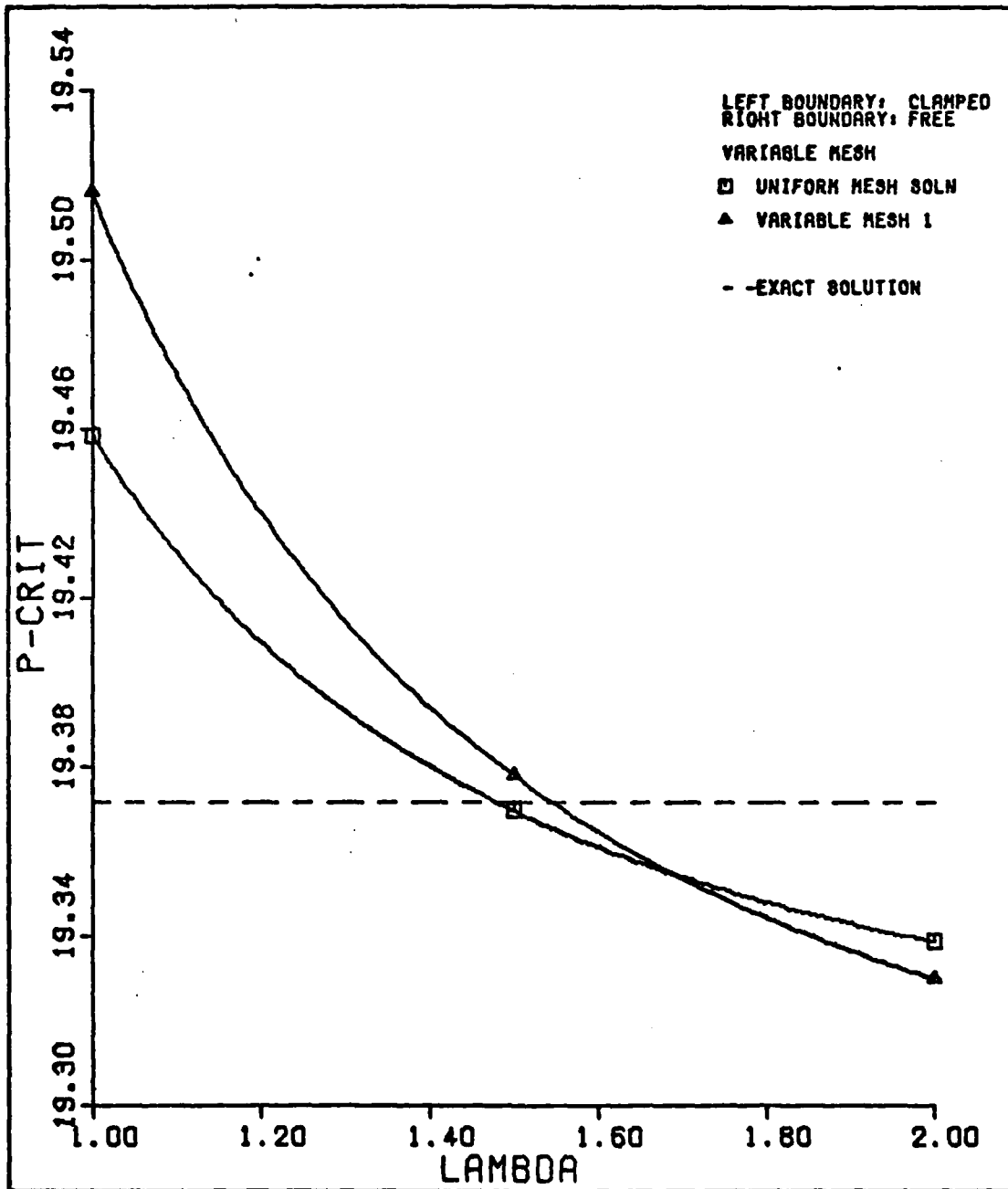


Fig 41. Uniform and variable mesh curves for a beam with exponential variations of inertia. Variable mesh 1 clusters 3 nodes around maximum inertia. $h_2 = .05L$. $N = 9$

VII. Extension to Composite Materials

Introduction

Throughout the previous sections, attention was given to varying the geometrical properties of the beam. No attention was given to the material itself. Material properties were assumed isotropic, with the result that the beam stiffness E was constant. However, the material stiffness was included as a possible function of distance along the beam. Stiffness, in combination with the inertia, form a product known as the flexural rigidity EI . By keeping E within the integration of the virtual work equation, Eq (3-30), the flexural rigidity can be considered a function of X also. The importance of this concept will be discussed shortly in conjunction with composite materials.

Composite materials consist of two or more constituent materials bonded together so that the gross material properties are superior to the constituents. Desirable properties (high strength, high stiffness, low weight) are maintained while undesirable properties are suppressed. By selecting the proper materials and combining them in an efficient geometrical arrangement, the desired gross properties can be achieved (35).

Because composite materials represent a way for the engineer to design structural elements to certain specifications

and still have control over other properties in the element, a method of modeling the composite beam will be developed in this section.

Theory

A composite beam is somewhat different from the isotropic beams used in the previous sections. To begin with, a composite beam can be formed by laying-up thin layers of material, one on top of the other. A layer of the beam, called a lamina, generally has fibers embedded within a matrix. The fibers provide most of the material strength, with the matrix serving to hold the fibers in place. As a lamina is layed-up, the fibers may or may not line up with the beam's principal axis. Figure 42 demonstrates fibers at an angle θ to the beam's X-axis. The combination of layers of material with different properties and orientations from lamina to lamina requires a new model of the beam.

To model a composite beam, two approaches are available:

- 1) Laminated beam approach
- 2) Laminated plate approach

Although the second method is not used in this analysis, it is worth discussing briefly.

Laminated Plate Approach

Much work has been done in conjunction with buckling of composite plates (28,33-36). To apply the method to a beam, a plate can be made very long and narrow. Two opposite edges of the plate are free while the other two are held in place.

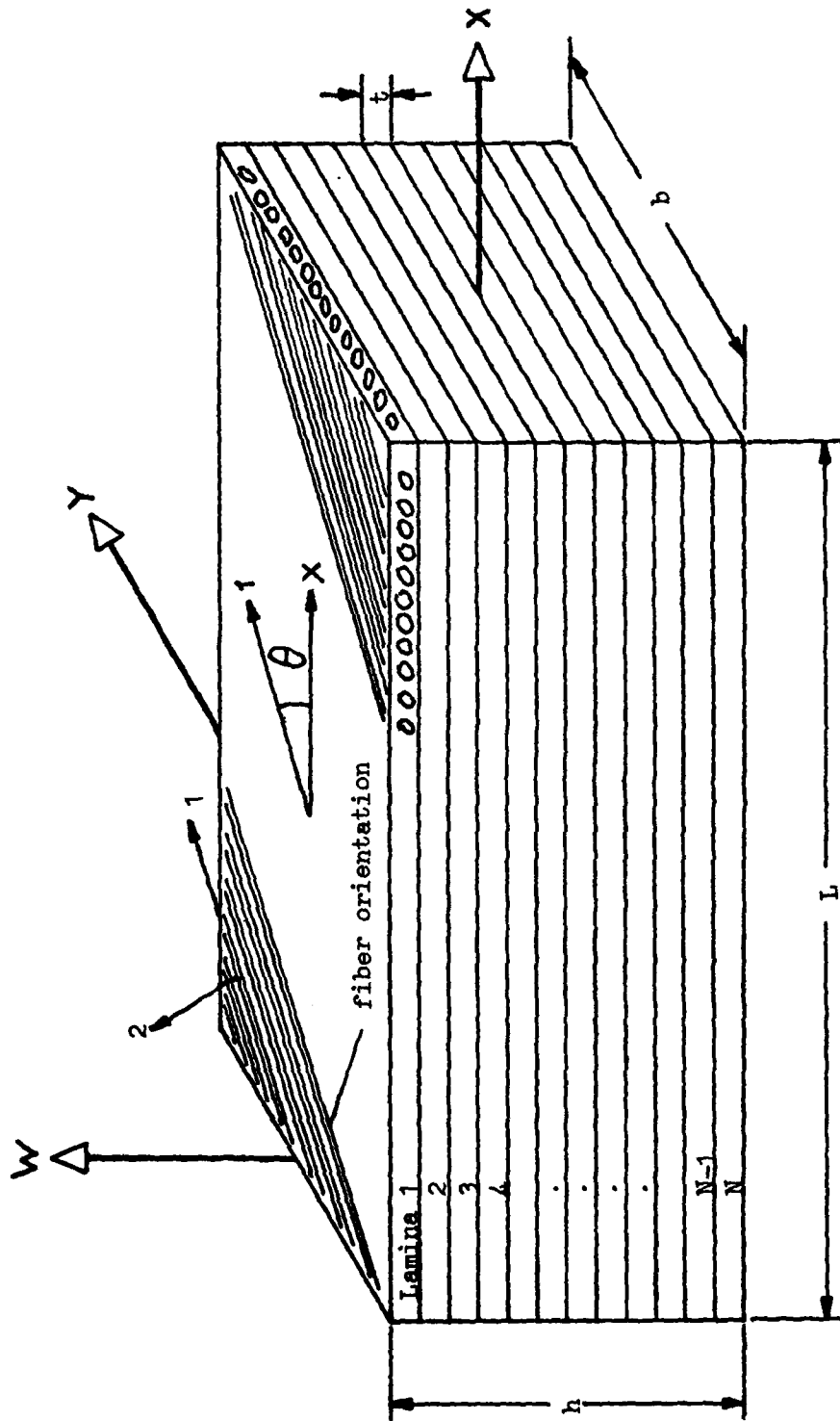


Figure 42. Typical composite beam lay-up

This approximates the boundary conditions on the beam. If the free edges are perpendicular to the y-axis, there will be no moment M_y at these edges. Because the plate is narrow, $M_y = 0$ is assumed for the entire width. Also, the line load along the plate's x-axis N_x is assumed constant.

The produce $N_x \cdot b$, where b is the plate width, approximates the axial load P upon a beam.

If only M_x and N_x are applied to this narrow plate, a beam loaded axially is now approximated. Using the equations relating moment, curvature, and in-plane loading available in composite textbooks (30), an expression for the moment can be derived

$$M_x = \frac{1}{D'_{11}} \frac{d^2w}{dx^2} - \frac{B'_{11}}{D'_{11}} N_x \quad (7-1)$$

The coefficients D'_{11} and B'_{11} are the bending and coupling stiffnesses for a composite laminate. If a beam of unit width is assumed, $N_x = P$. For simplicity, the laminated beam is assumed symmetric about the midsection. This simplification results in the coupling stiffness B'_{11} being set equal to zero. In addition, the bending stiffness reduces to D'_{11} , which is easily determined once the lay-up of the beam is defined. The moment equation has been reduced to a result which is directly substituted into the computer program for this thesis

$$M_x = D'_{11} \frac{d^2w}{dx^2} \quad (7-2)$$

D'_{11} can be considered as an equivalent flexural rigidity \overline{EI} . A further derivation is available in Appendix D.

Results

Very few results for the buckling load of a composite column are available in literature. Most work has been done in the area of plate buckling.

Calcote (28) does provide a simple theoretical solution for the buckling load of a pinned-pinned beam.

$$N_{cr} = \left(D_{11} - \frac{B_{11}^2}{A_{11}} \right) \frac{\pi^2}{L^2} \quad (7-3)$$

The buckling stress N_{cr} is expressed as load/width. For a beam of width 1.0, the total buckling load $P_{cr} = N_{cr}$.

Dietz derives a similar expression for the buckling load of a uniform composite beam of width 1.0 (27). If a beam has plies that are layed-up symmetrically about the mid-section, it can be shown that $B_{11} = 0$ in Eq (7-1). Dietz demonstrates that for such a symmetrically laminated beam,

$$P_{cr} = \pi^2 D_1 / L'^2 \quad (7-4)$$

The $(L')^2$ is the reduced length of the beam, the distance between two consecutive inflection points of the deflected mode shape. L' has the same meaning as λ_{opt} did for a simple uniform beam. The optimal wavelength for simple beams was found to correspond to half the buckled mode's wavelength, which corresponds to Dietz's L' . Therefore, since λ is known (Table II) for simple cases, Eq (7-4) can be used. To analyze simple composite beams, the only change in solving the eigenvalue problem is to replace EI by \overline{EI} or D_{11} (if symmetric). Therefore, the results of this section are mostly a check on calculating material properties.

As an example, a composite beam was made out of 20 plies of Boron-epoxy all oriented at 0° . Material properties were obtained from Reference 37. Because the plies are symmetric, the buckling load for a pinned-pinned beam ($L' = l$) from Eq (7-4) is

$$P_{cr} = 7584.43/L^2 \quad (\text{lbs})$$

for a $D_{11} = 768.468$ in-lbs. From a buckling curve, this load is returned for a $\lambda = 1.0$ (as expected for a pinned-pinned beam).

If the plies are all oriented at 90° to the beam's x-axis, weaker properties are presented towards the axial load. One would expect a lower buckling load because a boron-epoxy lamina is nine times less stiff at 90° than at 0° . The fibers are not longitudinally aligned. At $\lambda = 1.0$, a buckling load of $1028.6/L^2$ (lbs) is returned, matching the expected solution from Eq (7-3) or Eq (7-4).

Intermixing 0° and 90° plies returns a buckling load between the two cases already looked at.

The buckling load, determined by knowing λ_{opt} or finding the intersection of buckling load curves, is not the best answer. Results in this section used a laminated beam approach which assumed $\sigma_y = 0$, good only for orientations near 0° and 90° . Results for other orientations may not be as good.

Also, the effect of the shear modulus G has been ignored throughout this thesis in order to simplify the problem. Brunelle (36) shows that the buckling load for a pinned-pinned uniform beam is

$$P_{cr} = EI \frac{\pi^2}{L^2} / \left[1 + \left(\frac{h}{L} \right)^2 \frac{E}{G} \right] \quad (7-5)$$

where h is the beam height. In this thesis E/G was assumed zero, a reasonable assumption for isotropic material. For $E/G = 0$, Eq (7-5) returns the solution discussed in Section IV. A composite beam has a much higher E/G ratio than a solid metal column. For the boron-epoxy beam with all layers at 0° , the ratio E/G is about 40. To accommodate the transverse shearing modulus G , a correction factor is suggested. (28,33) which yields the buckling load for a pinned-pinned beam as

$$P_{cr} = \frac{EI \pi^2}{L^2} / \left(1 + \frac{\eta \pi^2 E r^2}{4L^2 G} \right) \quad (7-6)$$

A factor depending on the cross-section, η , is included as well at the radius of gyration r . Therefore, the buckling load returned by the methods of this thesis are going to be higher than they actually are.

In addition to the problems just mentioned, there are many others. The glue holding layers of the beam can fail leading to gaps in the beam. Individual fibers within a lamina can buckle on their own or even fail. The entire beam may fail before buckling occurs. The solution method used in this thesis does give a useful first try at the buckling load of a composite column though.

Summary

An approach was examined with which a composite beam can be modeled. The laminated beam model was chosen. This

model has the advantage of direct substitution of \bar{EI} for EI of an isotropic beam. Therefore, isotropic beam results are usable for composites. The solutions obtained matched the predicted results, as expected, because no real changes are made to the approach of Section III. Results will tend to be off from the actual solutions because of the laminated beam approach and the effect of the shear modulus G . However, the solutions achieved can be useful as a first approximation with which optimum orientations and geometries can be investigated.

VIII. Conclusions

This thesis investigated the results of using a trigonometric finite difference approach to solve the virtual work equation for the critical buckling load. When possible, the conventional finite difference solution was examined. Various values of λ were used in the trigonometric approach to determine both the correct solution as well as the range over which the trigonometric approach gave more accurate approximations than the conventional approach. A wide range of boundary conditions was included in this investigation. In addition, the effect of a variation in beam inertia and the use of a variable mesh size were checked. Finally, the application of the buckling load technique to a composite beam was made.

Based upon a recommendation in Hannah's thesis, the trigonometric approach was applied to the virtual work equation in order that the critical buckling load could be calculated. By using the trigonometric finite differences, the buckling load became a function of λ and the mesh size, as well as E , I , and L . Application to simple uniform beams provided a test of the technique. It was found for a large range of λ that the trigonometric approach provided more accuracy than with conventional finite differences. Increasing the number of nodes also increased solution accuracy.

The optimum wavelength was found to equal half the buckled wavelength, thereby pinpointing the location of P_{cr} . If the buckled shape was not known ahead of time, $\lambda = 1.4$ provided a fairly accurate solution for all 10 boundary conditions. In addition, eigenvectors produced by the numerical technique were found to match exactly with known mode shapes, as long as a node was positioned at the point of maximum displacement.

The effect of variations in inertia, both continuous and discontinuous, were examined. Beams with a larger middle cross section, as in the case of the exponential and sinusoidal variations, buckle at higher loads than their uniform cousins. The optimal wavelength does not correspond to any physical phenomena, such as the half-buckled wavelength. If the minimum inertia is normalized to 1.0, the optimal wavelength is larger than for the uniform beam. Normalizing the maximum inertia to 1.0 produces an optimal wavelength less than the uniform case. The difference between the uniform and variable inertia beam wavelengths is proportional to the size of the inertia increase. For the sinusoidal beam, the inertia did not change very rapidly. Therefore the optimal wavelength is only slightly larger than for the uniform beam. The exponential beam had larger and more rapid changes in inertia. The choice of λ_{opt} should be larger than the uniform solution of 1.0.

A discontinuous beam was modeled with maximum inertia as 1.0 in the thesis. Therefore, the optimal wavelength should be somewhat lower than the uniform solution, because

the variable beam is less stiff. This guideline is verified by the examples checked.

For beams with changes in inertia, the most effective buckling load curves were generated when a node was located at the position of maximum inertia or a discontinuity in inertia. By finding the intersection of two buckling load curves with similar nodal arrangements (i.e., same points of interest modeled), the buckling load and λ_{opt} were established. Failure to use similar nodal arrangements could lead to a poor solution and sometimes no solution at all. The intersection technique is better than guessing at a wavelength based upon inertia distribution, if greater accuracy is required.

The inertia at a discontinuity was modelled by a combination of inertias to either side of the discontinuity. This effective inertia maintained continuity in both slope and moment. However, below a certain value of effective inertia, the critical buckling load can be reached. The optimal wavelength will not be predictable with any accuracy though.

A variable mesh was tested in an effort to better model regions near a discontinuity or other points of interest. While the buckling curve is similar in form to the uniform mesh curve, it is less desirable to use. The intersection of variable mesh curves with each other or with a uniform mesh curve occurred at lower buckling loads than the actual solution. In addition, a variable mesh provided a larger error in approximating P_{cr} , compared to a uniform mesh with

an equal number of nodes, for most wavelengths. Only in a small wavelength range will a variable mesh be better. This could be useful to apply, though, if a uniform mesh cannot model all points of interest. Finally, as more nodes are packed near a discontinuity, the solution accuracy worsens.

In the last section of the thesis, a composite beam was analyzed using the laminated narrow plate approach. The approach permits the direct substitution of an equivalent flexural rigidity in place of the product EI . The thesis then treats the composite as an isotropic beam with the ability to change its flexural rigidity at each section. The effects of creating a beam out of composites does not directly enter the buckling load solution. Instead, the equivalent flexural rigidity is determined by using the composite properties of the beam. The direct substitution mentioned above permits the composite beam to be handled as easily as an isotropic beam. Also, the assumption of no shear effects by ignoring the shear modulus G produces a critical buckling load higher than in actuality. The composite beam approach does provide a useful first analysis of buckling which can be extended to discontinuous and other types of composite beams in the same manner as for an isotropic beam.

The numerical technique applied in this thesis provided accurate solutions for many types of problems. The main point to be followed was to place nodes at positions of significance along the beam. The intersection of two buckling load curves following this procedure provided the buckling

load and optimal wavelength for the truncated Fourier series. For a wide range of wavelengths, the trigonometric solutions are superior to those returned by conventional finite differences. If the intersection of buckling load curves is not used to choose a wavelength, the 10 known uniform solutions can act as guidelines in doing so. Increasing or decreasing the wavelength from the uniform optimal case will provide a fairly good answer. The amount of increase or decrease varies with the changes in inertia throughout the beam. Variable meshes are not of much use in determining the critical buckling load, unless a uniform mesh cannot be chosen which models all the points of interest. In this case a variable mesh may be useful for some part of the wavelength range. Finally, composites can be modeled by a simple change from EI to the equivalent flexural rigidity, based upon the composite properties.

Bibliography

1. Stein, M. and Housner, J. Numerical Analysis and Parametric Studies of the Buckling of Composite Orthotropic Compression and Shear Panels. NASA Technical Note D-7996, Washington: National Aeronautics and Space Administration, October, 1975.
2. Stein, M. and Housner, J. "Application of a Trigonometric Finite Difference Procedure to Numerical Analysis of Compressive and Shear Buckling of Orthotropic Panels." Computers and Structures. Vol. 9:17-25, 1978.
3. Hannah, S. R. Application of Trigonometric and Conventional Finite Difference Approximations to Beam Buckling. Unpublished Thesis. Wright-Patterson Air Force Base, Ohio: Air Force Institute of Technology, December 1976.
4. Hannah, S. R. and Palazotto, A. N. "The Incorporation of Truncated Fourier Series into Finite Difference Approximations of Structural Stability Equations." Computer and Structures. Vol. 9:603-607, 1978.
5. Calcote, L. R. and Wah, T. Structural Analysis by Finite Difference Calculus. New York: Van Nostrand Reinhold Co., 1970.
6. Salvadori, M. G. "Numerical Computation of Buckling Loads by Finite Differences." ASCE. Vol. 116, Paper No. 2441, 1951.
7. Ghali, A. and Neville, A. M. Structural Analysis: A Unified Classical and Matrix Approach. Scranton, PA: Intext Educational Publishers, 1972.
8. Wang, C. T. Applied Elasticity. New York: McGraw-Hill Book Co., 1953.
9. Hildebrand, F. B. Finite-Difference Equations and Simulations. Englewood Cliffs, N.J.: Prentice-Hall, Inc. 1968.
10. Wang, Ping-Chun. Numerical and Matrix Methods in Structural Mechanics. New York: John Wiley and Sons, Inc. 1966.

11. Nansen, R. H. and DiRamio, H. "Structures for Solar Power Satellites." Astronautics and Aeronautics. Vol. 16, Number 10:55-59, October 1978.
12. Ziegler, H. Principles of Structural Stability. Waltham, MA: Blaisdell Publishing Co., 1968.
13. Michalos, J. and Wilson, E. N. Structural Mechanics and Analysis. New York: The MacMillian Co., 1965.
14. Girijavallabhan, C. V. "Buckling Loads of Non-Uniform Columns." Journal of Structures Division, ASCE. Vol. 95:2419-2431, 1969.
15. Abbassi, M. M. "Buckling of Struts of Variable Bending Rigidity." Journal of Applied Mechanics, Transactions of ASME. Vol. 25:537-540, December 1958.
16. Abbassi, M. M. "The Second Approximation for Buckling Loads of Tapered Struts." Journal of Applied Mechanics, Transactions of ASME. Vol. 28:211-212, March 1960.
17. Sinha, S. C. and Chow, C. C. "Approximate Eigenvalues for Systems with Variable Parameters." Journal of Applied Mechanics. Vol. 46:203-205, March 1979.
18. Almroth, B. O. and Brush, D. O. Buckling of Bars, Plates, Shells. New York: McGraw-Hill Book Co., 1965.
19. Popov, E. P. Introduction to Mechanics of Solids. Englewood Cliffs, N.J.: Prentice-Hall, Inc., 1968.
20. Timoshenko, S. P., and Young, D. H. Theory of Structures. New York: McGraw-Hill Book Co., 1965.
21. Willems, N. and Lucas, W. M. Matrix Analysis for Structural Engineers. Englewood Cliffs, N.J.: Prentice-Hall, Inc., 1968.
22. Timoshenko, W. P. and Gere, J. M. Theory of Elastic Stability. New York: McGraw-Hill Book Co., 1961.
23. Shaker, J. Effect of Axial Load on Mode Shapes and Frequencies of Beams. NASA Technical Note D-8109, Washington: National Aeronautics and Space Administration, November 1975.
24. O'Rourke, M. and Zebrowski, T. "Buckling Load for Non-Uniform Columns." Computers and Structures. Vol. 7:717-720, 1977.
25. Acton, F. S. Numerical Methods that Work. New York: Harper and Row Publishers, Inc., 1970.

26. Franklin, J. N. Matrix Theory. Englewood Cliffs, N.J.: Prentice-Hall Inc., 1968.
27. Dietz, A. G. H. (ed) Composite Engineering Laminates. Cambridge, MA: MIT Press, 1969.
28. Calcote, L. R. The Analysis of Laminated Composite Structures. New York: Van Nostrand Reinhold Co., 1969.
29. Hopkins, R. B. Design Analysis of Shafts and Beams. New York: McGraw-Hill Book Co., 1970.
30. Jones, R. M. Mechanics of Composite Materials. Washington, D.C.: Scripta Book Co., 1975.
31. Moler, C. B., and Stewart, C. W. "An Algorithm for Generalized Matrix Eigenvalue Problems." SIAM Journal of Numerical Analysis, 10, 1973.
32. Almroth, B. O., and Brogan, F. A. "Numerical Analysis of Structures (Discretization Procedures)." Lockheed Missiles and Space Company, Inc.: Technical Report # LMSC-D556462, January 1977.
33. Broutman, L. J., and Krock, R. H. Composite Materials. Vol. 7 Structural Design and Analysis - Part I. Ed. by C. C. Chamis. New York: Academic Press, Inc., 1975.
34. Tsai, S. W. Analyses of Composite Structures. NASA Contract Report CR-620, Washington: National Aeronautics and Space Administration, November, 1966.
35. Tsai, S. W. Structural Behavior of Composite Materials. NASA Contract Report CR-71, Washington: National Aeronautics and Space Administration, July, 1964.
36. Brunell, E. J. "The Statics and Dynamics of a Transversely Isotropic Timoshenko Beam." Journal of Composite Materials. Vol. 4:405-407, 1970.
37. Mandell, J. R. An Experimental Investigation of the Buckling of Anisotropic Fiber Reinforced Plastic Plates. Air Force Materials Laboratory; AFML-TR-68-281, October 1968; Wright-Patterson Air Force Base, Ohio.

APPENDIX A

Derivation of the Virtual Work Equation

An arbitrary element of the beam acted upon by the axial load P is shown in figure A1.

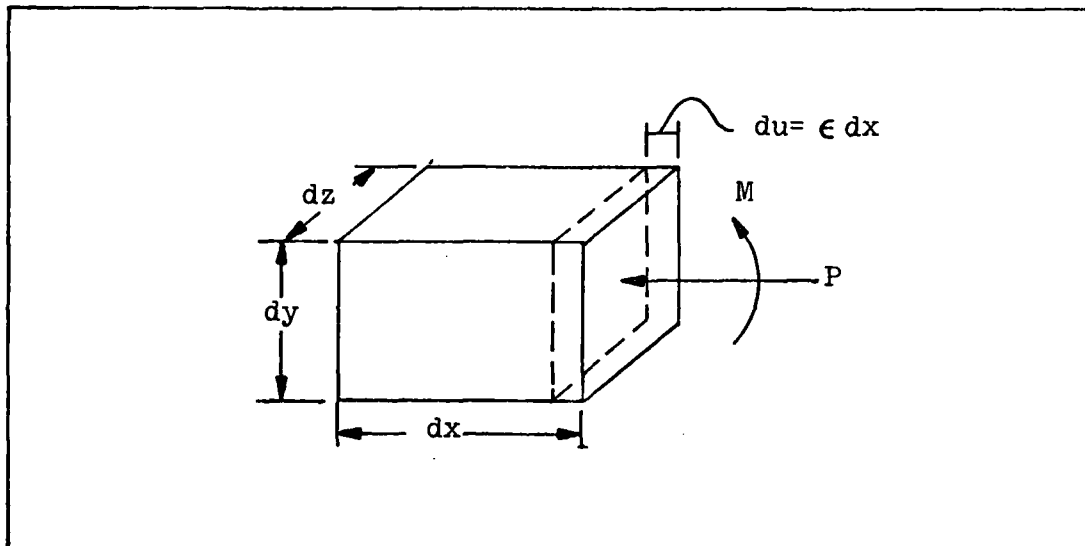


Fig A1. Beam Element Under Axial Loading

The stress produced on the element face is equal to the load divided by the area, $\sigma = P/dzdy$. The total strain energy in the beam is approximated by

$$U = \int_V \frac{1}{2} \sigma \epsilon \, dx \, dy \, dz \quad (\text{A-1})$$

From simple beam theory, $\sigma = \epsilon E$, providing the simplification

$$U = \int_V \frac{1}{2} \frac{\sigma^2}{E} \, dx \, dy \, dz \quad (\text{A-2})$$

Also from beam theory, the stress and moment are related by $\sigma = My/I$ and the inertia $I = \int_A y^2 dy dz$. Using these definitions, the strain energy of the beam reduces to

$$U = \int \frac{M^2}{2EI} dx \quad (A-3)$$

The moment in the beam can be expressed in terms of the deflection as $M = EIw''$. The strain energy reduces further to the familiar form

$$U = \int \frac{1}{2} EI \left(\frac{d^2 w}{dx^2} \right)^2 dx \quad (A-4)$$

The internal virtual work is the variation of strain energy, expressed as

$$\delta U = \int EI \frac{d^2 w}{dx^2} \frac{d^2 \delta w}{dx^2} dx \quad (A-5)$$

In addition to the internal work, external work is produced by the axial load as it moves through the displacement du .

The external work W_e is

$$dW_e = -\frac{1}{2} P du \quad (A-6)$$

The displacement du needs to be expressed in terms of the vertical displacement w before the external work expression is useful. Figure A2 illustrates a segment of the deflected beam segment AB' compared with the undisplaced segment AB .

An expression for AB' is

$$AB' = \left[(dx)^2 - \left(\frac{dw}{dx} dx \right)^2 \right]^{\frac{1}{2}} \quad (A-7)$$

This expression can be approximated, through the use of the binomial expansion, as

$$AB' = dx \left[1 - \frac{1}{2} \left(\frac{dw}{dx} \right)^2 + \dots \right] \quad (A-8)$$

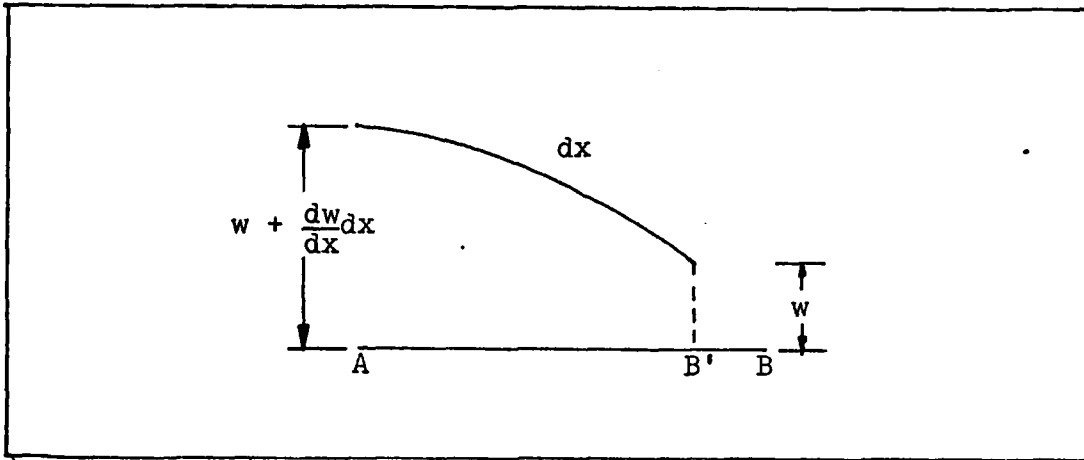


Fig A2. Deflected Beam Segment Shape

The displacement du equals the segment $B'B$, which in turn equals

$$AB - AB' = -\frac{1}{2} \left(\frac{dw}{dx} \right)^2 dx \quad (A-9)$$

The total horizontal displacement of the beam is found by integrating Equation 9 along the length of the beam

$$u = -\frac{1}{2} \int \left(\frac{dw}{dx} \right)^2 dx \quad (A-10)$$

The total external work done by the axial load is found by integrating Eq (A6) and substituting Eq (A10)

$$W_e = \frac{1}{2} P \int \left(\frac{dw}{dx} \right)^2 dx \quad (A-11)$$

The virtual work of the external force is

$$\delta W_e = P \int \frac{dw}{dx} \frac{d\delta w}{dx} dx \quad (A-12)$$

For equilibrium, the variation in total potential energy π must be zero, where $\pi = U - W_e$. This gives the virtual work equation

$$\delta U = \delta W_e \quad (A-13)$$

and

$$\int_0^L EI \frac{d^2 w}{dx^2} \frac{d^2 \delta w}{dx^2} dx = P \int_0^L \frac{dw}{dx} \frac{d\delta w}{dx} dx \quad (A-14)$$

APPENDIX B

Trigonometric Finite Difference Expression For the Second Derivative of Deflection with Variable Mesh

When a uniform mesh was used, the expression for the second derivative at node i was developed in Section III as

$$W''_i = \frac{1}{h^2} (W_{i+1} - 2W_i + W_{i-1}) \quad (B-1)$$

This derivative applies only when the mesh size is constant across the node. In Section VI, a variable mesh is used where the second derivative is required at a discontinuity in mesh size. A new expression is required for the second derivative at the change in mesh size. Figure B1 shows the mesh at the discontinuity, with mesh sizes h' and h'' .

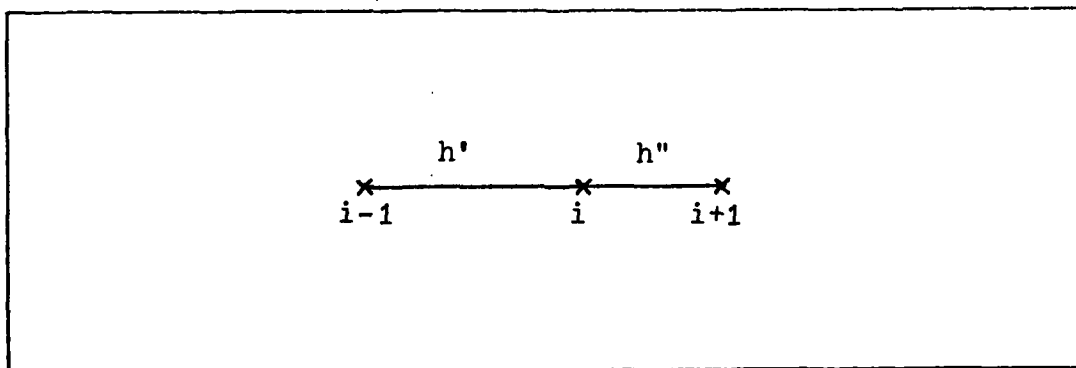


Fig B1. Variable Mesh Size Arrangement

The trigonometric expression used to generate finite differences is

$$W(X) = W_i + \frac{\lambda}{\pi} W'_i \sin \frac{\pi(X-X_i)}{\lambda} + \left(\frac{\lambda}{\pi}\right)^2 W''_i \left[1 - \cos \frac{\pi(X-X_i)}{\lambda}\right] \quad (B-2)$$

Applying the above expression at $X = X_i + h''$ and $X = X_i - h'$ yields the equations

$$W_{i+1} = W_i + \frac{\lambda}{\pi} \sin \frac{\pi h''}{\lambda} W_i' + \frac{\lambda^2}{\pi^2} \left(1 - \cos \frac{\pi h''}{\lambda}\right) W_i'' \quad (\text{B-3})$$

$$W_{i-1} = W_i - \frac{\lambda}{\pi} \sin \frac{\pi h'}{\lambda} W_i' + \frac{\lambda^2}{\pi^2} \left(1 - \cos \frac{\pi h'}{\lambda}\right) W_i'' \quad (\text{B-4})$$

The needed expression for W_i'' can be obtained with the following procedure: Multiply W_{i+1} by $\sin \frac{\pi h''}{\lambda}$, multiply W_{i-1} by $\sin \frac{\pi h'}{\lambda}$ and add the two expressions. Using the expression

$$1 - \cos \frac{\pi h}{\lambda} = 2 \sin^2 \frac{\pi h}{2\lambda}$$

reduces the second derivative to the desired result.

$$W_i'' = \frac{\sin \frac{\pi h'}{\lambda} W_{i+1} - \left(\sin \frac{\pi h'}{\lambda} + \sin \frac{\pi h''}{\lambda}\right) W_i + \sin \frac{\pi h''}{\lambda} W_{i-1}}{2 \left(\frac{\lambda}{\pi}\right)^2 \left[\sin \frac{\pi h'}{\lambda} \sin^2 \frac{\pi h''}{2\lambda} + \sin \frac{\pi h''}{\lambda} \sin^2 \frac{\pi h'}{2\lambda}\right]} \quad (\text{B-5})$$

Equation (B5) is the expression required for the second derivative at a node where the mesh changes. If $h' = h'' = h$, Eq (B5) reduces to Eq (B1) where

$$\tilde{h} = \frac{2\lambda}{\pi} \sin \frac{\pi h}{2\pi}$$

APPENDIX C

Effective Inertia at a Sudden Change in Cross-Section

For a beam with a discontinuity at node i , as shown in Figure C1, what is the value of the inertia at that node?

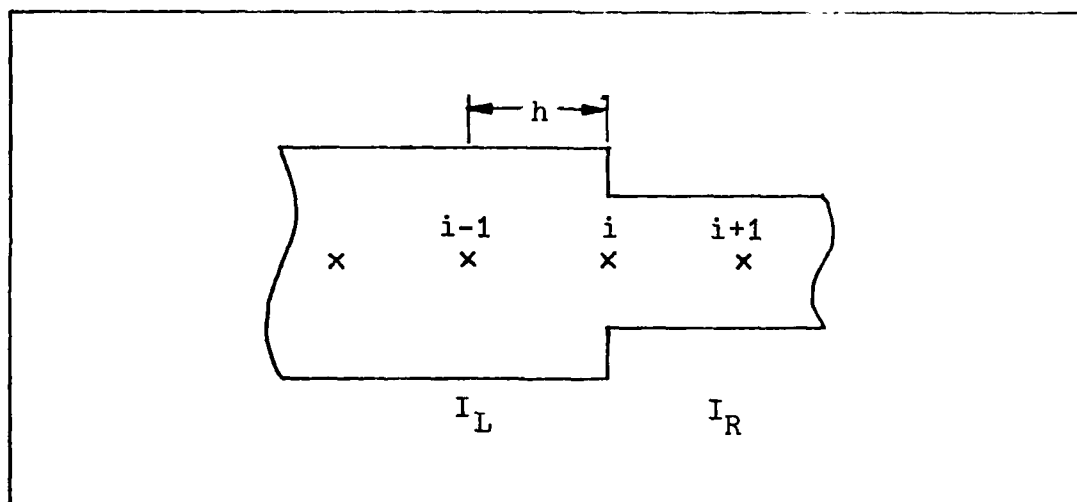


Fig C1. Step Change in Inertia

The inertia of the section left of the discontinuity is I_L and to the right, I_R . With these values and the deflection curve in Figure C2, the effective inertia can be calculated. The curves in Figure C2 are beam displacements from node $i - 1$ to node $i + 1$. Curve ABC is the true deflection, with displacements W_{i-1} , W_i , W_{i+1} , respectively. If curve A-B is extended to point C', a fictitious displacement W_{i-1}^f is generated for node $i + 1$. Likewise, extending curve C-B to point A' produces a fictitious displacement W_{i-1}^f at node $i - 1$.

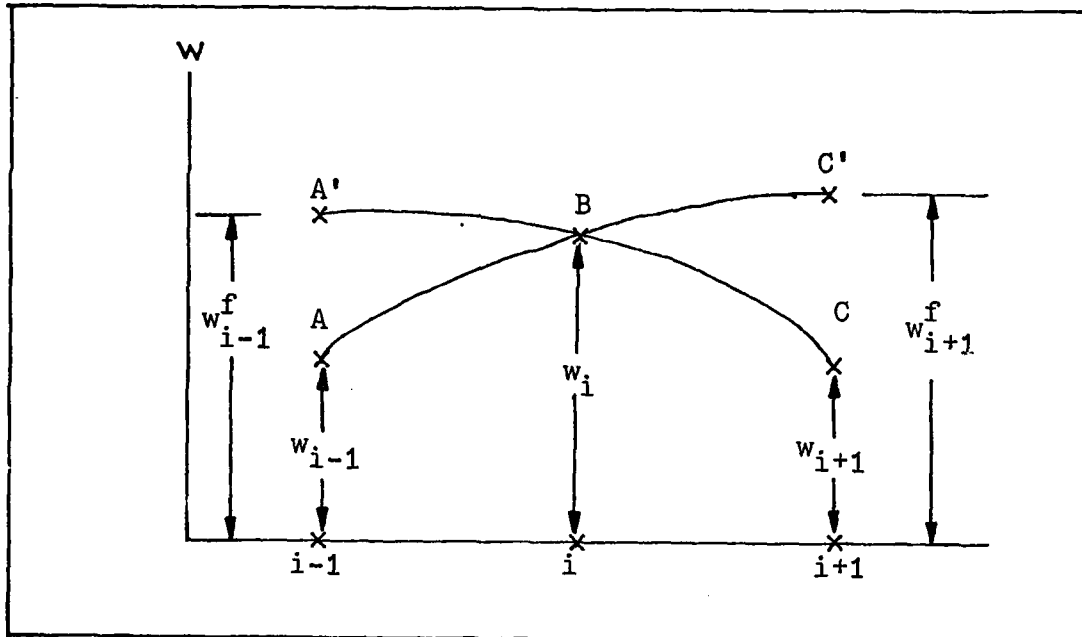


Fig C2. Fictitious and Actual Node Displacements

For compatibility, the slope of the two curves at i must be equal. Using a full-station central difference for slope

$$w'_i = \frac{1}{2h}(w_{i+1} - w_{i-1}) \quad (C-1)$$

yields the continuity equation

$$w_{i+1} - w_{i-1}^f = w_{i+1}^f - w_{i-1} \quad (C-2)$$

Also, for equilibrium, the bending moments either side of node i must be equal. The moment is described by $M = EI \frac{d^2w}{dx^2}$. Using a full-station central difference to equate moments produces

$$M_i = \frac{EI_L}{h^2}(w_{i+1}^f - 2w_i + w_{i-1}) \quad (C-3)$$

$$M_i = \frac{EI_R}{h^2}(w_{i+1} - 2w_i + w_{i-1}^f) \quad (C-4)$$

Expressing w_{i-1}^f in terms of w_{i+1}^f from Eq (C2) and inserting

into Eq (C3) and Eq (C4) produces two equations for M_i in terms of W_{i+1}^f . Eliminating the fictitious displacement from both equations produces

$$M_i = \frac{2EI_L I_R}{h^2 (I_L + I_R)} [W_{i+1} - 2W_i + W_{i-1}] \quad (C-5)$$

The general form for the moment at node i is

$$M_i = \frac{EI_{eff}}{h^2} [W_{i+1} - 2W_i + W_{i-1}] \quad (C-6)$$

By comparing the two moment equations, the effective inertia at a discontinuity is

$$I_{eff} = \frac{2I_L I_R}{I_L + I_R} \quad (C-7)$$

APPENDIX D

Flexural Rigidity of a Composite Beam

The laminated beam approach is used to model the flexural rigidity \bar{EI} of a composite beam.

From this approach

$$\sigma_z^i = \sigma_{xy}^i = \sigma_{yz}^i = M_y^i = 0 \quad (D-1)$$

and

$$\sigma_x^i = \bar{Q}_{11}^i \epsilon_x^i \quad (D-2)$$

The superscript i is the layer number for a ply in the composite. The assumptions in Eq (D1) yield the stress equation (D2). Stress in each layer is modeled by Hookes' Law. The strain ϵ_x can be expressed in terms of distance from the mid-section and the curvature as $Z(d^2w/dx^2)$. Substituting into Eq (D2) gives

$$\sigma_x^i = \bar{Q}_{11}^i Z \frac{d^2w}{dx^2} \quad (D-3)$$

The moment in a simple isotropic beam is given by the formula

$$M = EI \frac{d^2w}{dx^2} \quad (D-4)$$

For a composite beam, the moment is found by integrating the stress and its moment arm throughout the thickness.

$$M = b \int_{-t/2}^{t/2} \sigma_x^i Z dz \quad (D-5)$$

The composite beam is of constant width b and thickness t .

Substituting for σ_x^i from Eq (D3) produces

$$M = \left(b \int_{-t/2}^{t/2} \bar{Q}_{11} z^2 dz \right) \frac{d^2 w}{dx^2} \quad (D-6)$$

Comparing Eq (D4) and Eq (D6) shows that the same moment-curvature behavior results for a composite beam if an equivalent flexural rigidity

$$\bar{EI} = b \int_{-t/2}^{t/2} \bar{Q}_{11} z^2 dz \quad (D-7)$$

is substituted into Eq (D6). The moment equation becomes

$$M = \bar{EI} \frac{d^2 w}{dx^2} \quad (D-8)$$

Because the eigenvalue equation of this thesis was derived using Eq (D4), a simple substitution of \bar{EI} for EI permits modeling of composite beams.

Using this equation, Dietz (28) reduces the equivalent flexural rigidity to the form

$$\bar{EI} = b \left(D_{11} - \frac{B_{11}^2}{A_{11}} \right) \quad (D-9)$$

The values of D_{11} , B_{11} , A_{11} are dependent upon the thickness, location, orientation, and material properties of each layer.

The equations describing D_{11} , B_{11} , and A_{11} are available in composite textbooks (30).

Vita

John Louis Insprucker III was born on 7 October 1956 in Cincinnati, Ohio. He moved to Detroit, Michigan, where he graduated from Bishop Borgess High School in 1974. He attended the University of Michigan from which he received the degree of Bachelor of Science - Aerospace Engineering, summa cum laude, in April 1978. Upon graduation, he was commissioned into the USAF through the four year AFROTC program. His first assignment was to the School of Engineering, Air Force Institute of Technology, in August 1978.

Permanent Address: 6573 Whitefield
Dearborn Hts., Michigan 48127

UNCLASSIFIED

SECURITY CLASSIFICATION OF THIS PAGE(When Data Entered)

Of boundary conditions. Choosing the optimal wavelength produced the result from literature. An optimization scheme was used which determines the critical load by locating the intersection of two buckling load curves. The method is accurate as long as points of interest - maximum inertia, discontinuities - are modeled by the nodal arrangement. The trigonometric approach provided improved accuracy over the conventional approach for a wide range of wavelengths. For an infinite value of the wavelength, the trigonometric approach converges to the conventional one. A variable mesh designed to concentrate nodes about points of interest was found to be relatively ineffective when compared to a uniform mesh. Composite materials were modeled using an equivalent flexural rigidity.

UNCLASSIFIED

SECURITY CLASSIFICATION OF THIS PAGE(When Data Entered)